The effect of channel bed infiltration on flood wave progression in ephemeral systems

Firas Alazem

The University of Leeds

School of Civil Engineering

submitted accordance with the requirements for the degree of Doctor of Philosophy

June 2023

Acknowledgements

I would like to express my sincere gratitude and appreciation to my supervisors, Professor Andrew Sleigh, Professor Mark Trigg, and Professor Nigel Wright for their continuous support and guidance, all over my PhD journey. Without their support, this thesis would not have been possible.

I would like to thank Cara (the Council for At-Risk Academics) and the University of Leeds for their contribution funding my PhD.

I would like to sincerely thank my blessing wife Nour Aswad for all of her love, support and push during the challenging time of my PhD.

I wish to thank my parents Rola Abdeen and Luay Alazem. They born me, raised me, loved me and taught me. Special thanks to my brother Ammar Alazem.

Lasty, this is all for my son Daniel Alazem.

Abstract

One of the most catastrophic natural hazards around the world is flooding, as they were constantly associated with very high levels of damage. This natural hazard is reported to have a greater reoccurring possibility in recent times. However, flooding in arid and semi-arid climates has received a relatively limited attention in the literature, which means there is a scarcity in data and understanding relating to floods and hydrological processes in arid and semi-arid areas. Such processes include ephemeral river systems, flash flooding, high channel infiltrations and high evaporation rates. Therefore, the aim of this research is focused on studying the effect of channel bed infiltration on flood wave progression in ephemeral systems, where this process is most important. This investigation can lead to a more profound understanding of the flood wave progression, and hence, can support conducting more robust flood risk assessments in both, temporal and spatial terms. Additionally, this realization of ephemeral systems can be essential for local authorities to make highly informed predictions of flood warning systems, effective emergency response, and resilience measures.

In order to achieve this aim, a Green-Ampt infiltration model was implemented within the LISFLOOD-FP hydrodynamic model. The evaluation of the effectiveness of the updated version of the hydrodynamic model was assessed through 4 testing levels of increasing complexity. The case study of the area has been chosen for this research, due to several occurrence of flood that hit the city of Hafr Al-Batin, which caused numerous losses in human life, damage to the public and private properties. Various model scenarios were constructed for the ephemeral wadi system upstream of Hafr Al-Batin, which including different infiltration process representations (none, steady state and variable) and these were used to evaluate the importance of infiltration on the flood wave characteristics.

The outcome of this research shows that the Infiltration losses have significant implications on the flood wave propagation characteristics in ephemeral river systems. These includes the extent of the flooded area, the water volume and the flow travel time. These were demonstrated in the study catchment area of Wadi Al Batin in Saudi Arabia. The conclusion from this study is that applying the spatial variable Green-Ampt infiltration losses is necessary in ephemeral systems and will provide more robust hydrodynamic modelling for use in the flood risk assessments in these systems.

Table of Contents

List of Figures

List of Tables

Chapter 1: Introduction

1.1 Background to the Study

Floods can be categorized under one of the following three major kinds: drainage flood, river floods, coastal flooding and flash floods (Jonkman and Vrijling 2008), which are considered the most damaging among the other kinds. The danger of flash floods comes from its rapid development, their irregularity and unpredictability and their abruptness. These characteristics have been proven through statistics aimed to investigate the reasons leading to the high level of risk associated with flash floods (Korichi et al. 2016).

It is widely accepted that one of the most high-risk and dangerous-to-life natural hazards is that associated with flooding – and that this risk is high almost anywhere around the world, particularly in areas where rain is most frequent (Guha-Sapir et al., 2014). MunichRe (2015) referred to flooding, and flash-flooding in particular, as one of the most catastrophic hazards for any country. One factor leading to such a conclusion is the high number of victims affected by flooding disasters every year. A further factor is the frequent reoccurrence of floods as reported by UNISDR (2015), who say that floods have been the most reoccurring destructive force, particularly in the period between 1994 and 2013. Asia is referred to the continent most facing the challenge of floods according to Budiyono et al. (2015). Furthermore, the rapid urbanization has a significant implication on pluvial and fluvial flooding. the damages resulting from the flood risk increase by the rapid urbanization and the reduction of the forests, shrubs, and farmlands.

Furthermore, it is worth mentioning that critical and the cumulative implications of the pluvial flooding by increasing the urbanization, which accrues in relation with heavy precipitation that exceeds the drainage systems.

Consequently, significant resources have been dedicated to predicting flood occurrence, and to control the damage caused by this disaster. To do so, Hansson et al. (2008) confirms that vulnerable areas must be identified, and the factors that intensify the severity of the resulting damage must be determined.

As referred earlier, the most damaging kind of floods, in terms of casualties and properties, is the *flash* floods, because these floods, despite their short duration time, are characterized by the element of unpredictability, the pervasiveness of the phenomenon around the world, and the large amount of fast-moving water, causing the highest level of risk when compared to the other kinds of flood. Moreover, the major water capacity will be depleted again within few hours (Balica 2012).

Since flash floods are directly linked to heavy rainfall, they affect the watershed to a great level. Such floods have a few hours (or less) of responses time, and normally cover around 1000 km^2. There are mainly two reasons for such a duration response; firstly, is the watershed size, and secondly is the effective water transport process, or what is called the runoff. Thus, it is noted by Borga et al. (2007) that a process analysis of flash floods needs to be conducted to address the problem of the unpredicted and exceptional hydrological behaviour of flash floods, which is the cause of high level of fatalities (Korichi et al.,2016).

There has been a great deal of examples on the high number of flood victims in the 20^{th} century. The Lisbon, Portugal flood in 1967, and the flood resulted from the Banqiao dam break in China both reported a number of deaths reaching 464 and 231,000 deaths, respectively. Another significant example is the flood of November 2001 in Algeria, with 700 deaths in Bab El Oued in Algeria, 45,000 people being severely affected, and an amount of over 300 million dollars property damage. The reoccurrence of floods in Algeria made more than half of its population prone to the risk of flood, as reported by the National Agency of Water Resources (Korichi et al. 2016). All of these examples lead to the conclusion that flash floods and inundations were directly associated with most of the catastrophic events that occurred in the twentieth century (Hand et al. 2004).

Despite the uniformity of results and damage caused by floods, there are some differences in the process leading to flood generation. To specify, semi-arid environments and wet environments actually have different processes of creating floods. According to Camarasa-Belmonte (2016) semi-arid areas can have rainfall with high intensities, exceeding soil infiltration primary capacity, which might lead to overland flow, despite the aridity of the soils. The intensity of precipitation and the storm moment, where maximum intensity can be found, both affect the rainfall-runoff processes considerably. However, the is not a fixed situation. Dunkerley (2012) and Camarasa-Belmonte and Soriano (2014) both indicated that there are some differences whether the maximum values are at the beginning versus the end of the storm.

On the other hand, the hydrological connectivity into the basin can greatly affect the flood formation, as this connection is essential in determining the water flow to the outlet. By depending on the morphoclimatic context, defining this connectivity becomes possible. For instance, connectivity in temperate humid environments relies on the connection between saturated areas of hill slopes and stream channels. However, connectivity in semi-arid environments results from the interaction between different patches of soil with significant variation in hydrologic behaviour (Wainwright et al. 2011; Bracken et al. 2013). This can lead to the conclusion that headwaters-generated runoff can be prevented from draining to an outlet, by semi-arid conditions, the local character of the rain, and the heterogeneity of the territory.

In regard to flood risk analysis, it is confirmed that there should be a comprehensive consideration of the elements contributing, or could be possibly adding up to the damage. Korichi et al., (2016) clarified how it is essential to consider all the possibilities, potential scenarios, possible damage, and uncertainties in the flood risks' analysis. Each of these factors can contribute the formation of a risk curve which is the distribution function of flood damage in the studied area. There are several reasons that might cause risk analysis uncertainty, which include statistics of maximum annual discharges, changes in river channel over time, collapse of embankments, genesis of hysteresis during a flood wave, and tributaries.

Camarasa-Belmonte (1995) listed some of the examples of ephemeral streams lack of normality. First, it was noted that the big amount of transmission losses, happening during the flood, and transferring the majority of the water to sub surface throughflow paths, is one example. Another instance is the impact caused by the intensity of rain during the initial period of storms on the rainfall runoff conversion outcomes, and how it would hinder the infiltration process to form overland flow, despite the aridity of the soil. Camarasa and Tilford (2002), on the other hand, added more examples, featuring the base flow absence, and the minimized impact of the basin in rainfall-runoff conversion processes during high energy events.

Therefore, it is critical to study the physical events, causing the initial problem, and human activity in the damaged locations, in order to effectively deal with the risks linked with the aforementioned river systems (Adger 2006). To be specific, there are three essential elements incorporating the flood risk assessment. These components are the foreseen hazard, i.e., whether flood is going to reach a certain threshold; vulnerability, i.e., "the potential adverse consequences, especially for human health, the environment, cultural heritage and economic activity"; and exposure, i.e., "an inventory of those people or artefacts that are exposed to a hazard" (UNDP 2004). Evaluating these three components is crucial for the accuracy of any flood risk assessment.

Through considering the hydrological aspect, it can be concluded that due to the lack of base flow, these ephemeral systems can rely heavily on rainfall. Furthermore, they tend to have a high dynamic aspect during flood events, even though they are waterless most of the year. According to Camarasa and Tilford (2002), water flow in these systems, therefore, is dominated by large-scale, low-frequency events.

Because of the technical issues associated with gauging dry riverbeds, it is difficult to obtain flow data in ephemeral streams, when seen from a hazard prespective. Additionally, Jin and Ward (2005) noted that both flood type and the spatial pattern of the overland flows can both be affected by the possibility of floodplain change. Thus, similar to any other semi-arid river systems, ephemeral streams

can occur in areas subject to floods. These areas normally change through the progression of time as result of the high intensity rainfall events.

On the other hand, there can be three prominent factors that can be associated with the human activity in floodable areas, which are characterized by vulnerability and exposure to floods. These factors are the high human presence on floodplains, population's lack of knowledge regarding the possible risks, and the inefficiency in swift reaction to the hazard (Camarasa-Belmonte and Soriano-García 2012).

Finally, ephemeral streams, as seen through the elements of vulnerability and exposure, are often densely populated areas, which have been utilized for regular and intensive farming, economical activities, and residential practices. As suggested by Camarasa-Belmonte and Soriano-García (2012), risk mapping can be a highly effective replacement and/or parallel approach for flood risk management in spatial planning, where both risk perception and management are lacking.

The ephemeral channels can allow for a correlated interaction between the flood movement and the ground infiltration. To stress: infiltration into the ground is influenced by the floods' movement in ephemeral channels, and the latter is influenced by the ground infiltration. This intertwinement necessitates the use of robust numerical simulation of flood flow movement along with channel transmission losses simultaneously, in order to better estimation any water management activity that happens in arid and semi-arid areas, including water balance. It is noteworthy that channel infiltration could have a grave significance in water and environmental planning and management in dry land environments (Costa et al. 2013).

In an attempt to evaluate the infiltration in alluvial channels, Abdulrazzak and Sorman (1988), conducted their study in a wadi bed. It was concluded that the amount of water lost to infiltration into the wadi bed as the flood wave progresses in the downstream direction, two elements were directly affected: the magnitude and the frequency of recharge from ephemeral streams. Due to the large amount of flood flow that is usually infiltrated in alluvial channels, the study relied basically on this study results to outline the elements on which cumulative infiltrated volume depends on. In other words, the amount of abstraction is heavily reliant on the soil profile, certain physical conditions, and rainfall and runoff characteristics. Thus, soil moisture deficit and evaporation requirements can be addressed by the infiltrated volume. This would, hence, take part in recharging the alluvial aquifer.

1.2 Research Gap

One of the most catastrophic natural disasters around the world is flooding, as they were constantly associated with very high level of damage. This natural hazard is reported to have a greater reoccurring possibility in recent times, due to the drastic climate change. Number of studies found that factors, such as higher sea levels and more intense cyclonic weather systems and precipitation, are expected to increase, leading to a greater frequency of flooding. As a result, there have been a great deal of attempts to devise strategies that would help put up with floods damaging effects. Such strategies include flood-plain building regulations, reservoirs, and levee projects. Yet, one of the most effective measures that can influence floods movement is ground infiltration. Likewise, infiltration in ground is also affected by the movement of floods in ephemeral channels. The efficiency of all these measures, including infiltration, depend heavily on better estimations of floods, water balance, and other water management activities.

Infiltration, in particular was one of the factors that has been profoundly investigated in a considerable number of studies, due to its pivotal role in hydrology (land-surface and subsurface). Thus, many infiltration models have been developed, and were basically classified under one of the following three groups: physically based (or theoretical or mechanistic), semi-empirical, and empirical (Mishra et al. 1999). These infiltration types were ultimately created, compared, and analysed for the purpose of simulating one-dimensional and two-dimensional flow routing infiltration models. The literature provided some evidence that confirms the importance of identifying the peak discharge and volume of a catchment, as it leads to reaching more reasonable result on the largest flash flood. Such evidence was presented in the Weiler et al. (2020) study, which confirmed the significance of analysing the spatially and temporally controlled superimposition of runoff formation and runoff concentration, due to its effect on modelled peak discharge and discharge volume for a given catchment. Furthermore, it is believed that reaching a precise prediction of the recharge into aquifers and increasing the amount of recharge at targeted locations, accordingly, relies heavily on the correct estimation of time of arrival and travel distance of flood events. Consequently, to make similar predictions, the spatial distribution of transmission losses and the channel must be fully comprehended.

For this reason, careful attention has been given to the flash floods in semi-arid environments, to fully grasp the relationship between inflow and channel characteristics. Moreover, after reviewing the literature, it is found that there has been a scrutiny of the interaction between the surface flow and the infiltration, along with the channel bed infiltration within hydraulic flood routing models.

On the other hand, some models have been developed to explicitly simulate the ephemeral channel rivers (El-Hames and Richards 1998, Mudd's 2006, Smith et al. 1995), as they can be fundamental for

understanding the inflow discharge and channel characteristics relationship. This interaction manages the infiltration and downstream discharge within ephemeral river reaches. In the same vein, studies such as Freyberg (1983), Parissopoulos and Wheater (1991), and Mudd's (2006) focused on the interoperability between infiltration and surface flows. Moreover, some studies were dedicated to creating different models of infiltration to evaluate the effect of incorporating intensive streambed infiltration. For instance, Cheng et al. (2015) integrated a model to estimate the infiltration model based on the Horton equation, while Balamurugan and Bhallamudi (2016) developed a model incorporating compound cross-sections with flood routing in ephemeral channels.

In addition to studies developing infiltration models, plenty of studies investigated the importance of integrating infiltration models with flood routing methods, because of the great effect it has on the overland flow hydrograph. For instance, Gülbaz et al (2020) combined Integrated Horton type of infiltration method equations, representing different types of flood wave equations, in an attempt to study the effects of this coupling. Another example is the study of Ni et al (2020), which was based on a two-dimensional (2D) hydrodynamic. This study created a model that specifically targeted shallow water flows that demonstrated high infiltration losses. By the same token, Tügel et al.'s (2020) also created a model that targeted the coupling of shallow water flow and infiltration. On the other hand, Courty et al (2017) adopted Itzï model, to replicate a two-dimensional surface flow.

This overview shows that a deep inspection of the related literature in the field of infiltration models have provided a considerable number of studies investigated infiltration models from different aspects. In other words, the available studies have provided a variety of infiltration models, extensive data on different topographical models, and the effect of these topographical data on infiltration models. Moreover, researchers have attempted to integrate infiltrations equations within the hydraulic models, through the one-dimensional (1D), two-dimensional (2D) and simulations of these models such as Itzï, to focus on the surface runoff water with infiltration, i.e., integration of water simulations with infiltrations.

Moreover, Green-Ampt infiltration has been integrated with TUFLOW, HEC-RAS, MODFLOW, and Flood Modeller However, and to the knowledge of the author, there have been very scarce, if any, attention that was given to the effect of such integration on flood waves progression.

Thus, the aim of the current thesis was to:

> *Extend an existing robust 2D flood inundation model (LISFLOOD-FP) by implementing the variable spatial infiltration process in the existing ephemeral channel flow routing in order to understand the importance of this process on the prediction of flood risk parameters.*

Therefore, this aim is focusing on studying the effect of channel bed infiltration on flood wave progression in ephemeral systems, where this process is most important. This investigation has the potential to lead to a better understanding of the flood wave progression in such systems, and hence, can support more robust flood risk assessments in both, temporal and spatial terms. Additionally, this realization for ephemeral systems may be essential for local authorities to make highly informed predictions of flood warning systems, effective emergency response, and resilience measures.

1.3 Research Objectives

The research Objectives are defined as follows:

- To investigate and determine the sensitivity of 2D flood inundation models to the various topographical spatial data and various infiltration scenarios to assess whether higher spatial resolution digital elevation models will lead to more robust flash flood predictions in ephemeral river systems.
- To implement the spatially variable infiltration model into the 2D flood inundation model and assess and evaluate its effectiveness.
- To determine whether implementing the spatial variable infiltration process in ephemeral channel flood routing models will lead to more robust flash flood assessments, and potentially provide more effective prediction, warning flood systems and effective emergency response.

1.4 Outline of the Thesis

The present Thesis consists of six chapters, as follows:

- Chapter 1 presents the background of the research, research gap, research aim and objectives, as well as an outline of the thesis.
- In Chapter 2, a literature review is presenting a review of various infiltration models, evaluation of Digital Elevation Models (DEMs) for flood inundation modeling, and interaction between the surface flow and the infiltration as well as incorporating the channel bed infiltration within hydraulic flood routing models and draws out the key literature gaps.
- In Chapter 3, a baseline 2D hydraulic modelling of a case study of Wadi Al Batin is presented with a range of DEM spatial data resolutions, channel Manning's friction coefficient and various infiltration scenarios in order to investigate the implications of the channel bed infiltration on the wave propagation in ephemeral river systems.

- In Chapter 4, development of a variable infiltration method is presented within a 2D hydraulic model and its effectiveness is evaluated through testing 4 levels of increasing complexity.
- In Chapter 5, reports on the application of the developed 2D hydraulic model to the study catchment of Wadi Al Batin and the exploration of the consequential implications on flood wave progression in the ephemeral system.
- In Chapter 6, the overall conclusions are presented as well as recommendations for further studies on the effect of channel bed infiltration on the flood wave propagation in ephemeral systems.

Chapter2 Literature review

2.1 Introduction

In this chapter, the associated literature will be reviewed to highlight some basic concepts related to the current thesis's area of study. The chapter will start by presenting and evaluating the most prevailing infiltration models that exist in the current literature. These models are the Green–Ampt Model, the Linear Smith–Parlange Model, the Non-linear Smith–Parlange Model, the Singh–Yu model, the Mishra–Singh Model, the Smith Model, the Holtan Model, the Overton Model, the Kostiakov Model, the Modified Kostiakov Model, the Huggins–Monke Model, and the Collis-George Model, all of which fall under one of the three major categories: the physically based, the semi-empirical, and the empirical infiltration models. Then, the chapter will refer to the modifications made to the Green–Ampt (GA) model, which includes nine main models, explaining the advantages and disadvantages of the Green–Ampt (GA) infiltration model.

Following this an analysis of the Digital Elevation Models (DEMs) for flood inundation modelling will be provided, describing the current tendency towards utilizing these models, and discuss their limitations. This presentation will evaluate the DEMs, describe their effects on flood inundation modelling, raster-based model of flood flow, and flood risk analysis in cities. In addition to these trending models, a description of Global digital elevation models (GDEMs) in creating flood hazard maps will be also included. Finally, the chapter will present a review of the studies conducted to investigate flash floods in semi-arid environments. This review will highlight factors such as the surface flow and the infiltration interaction, the channel bed infiltration within hydraulic flood routing models, and the results of incorporating high-rate streambed infiltration. The last section will also review papers studying overland flow dynamics which are unique to infiltrating surfaces, flood routing in ephemeral channels with compound cross-sections, as well as the high losses due to infiltration in deeper water flows.

A widely recognized definition of flood is the high-water flow that outstrips the potential flow capacity of a stream's natural or artificial banks. This natural phenomenon has been reportedly described as a vastly devastating phenomena, causing high rates of both human losses and property damage. For instance, the study of Guha-Sapir et al. (2014) published that only in 2013, around global 10,000 human lives were lost in flooding. However, this is not the only factor that signifies the risk of floods.

Many regions across the globe consider flooding as their worst natural disaster challenge. One of these instances is Saudi Arabia, the catastrophic flood of 2009 brought about significant numbers of deaths, damage, and financial losses. As a result of this flood 121 people were killed, and other 20,000 lost

their homes. Moreover, the flood had caused huge property and financial losses of around 3 billion riyals, which was estimated to be billions of dollars as well the victims suffered health problems after the flooding (Momani and Fadil 2010). It was also reported by the study of Maghrabi (2012) that in addition to the large number of fatalities, the flood caused dramatic damage in Jeddah's structure, properties and highways.

Similarly, floods have been reported as one of the most destructive natural disasters in Algeria. Korichi et al. (2016) published that in the flood of November 2001, there have been over 700 deaths in Bab El Oued. In addition, there were more than 45,000 victims, who faced health issues and property losses as a direct result of this flood. The monetary losses were reported to have reached 300 million dollars.

There have been considerable contributions to the study of the risks of floods across the globe. However, these studies considered mainly developed countries, as these offered a great deal of data to consider. Furthermore, most of profoundly studied areas had temperate climates, presenting results specific to floods that occur in these areas. Flooding in arid and semi-arid climates have received a relatively limited attention, which means there have been a scarcity in data relating to floods and the hydrological processes in arid and semi-arid areas. Such data includes ephemeral river systems, flash flooding, high channel infiltrations and high evaporation rates.

Flooding formation is essentially dependent on two factors: the hydrological connectivity in the basin and the climate. It is crucial to consider the basin as it is essential in the water flow to the outlet. However, the most important determiner of this association is the morphoclimatic context. For instance, the connectivity in temperate humid environments is reliant on hill slopes' saturated areas and their association with the stream channels. In semi-arid areas, on the other hand, the connection is determined by the interaction that happens between the varied hydrologic soil behaviour in a mosaic of patches covering the basin (Bracken et al. 2008; Bracken et al. 2013). Consequently, characteristics of semi-arid conditions, such as the local characterization of the rain and the heterogeneity of the terrain, are major factors that could prevent runoff produced at the head waters from reaching the outlet. Bracken and Croke (2007) add that when hills fail to contain enough runoff to counteract run-on intrusion at the base of the slope, sedimentary transitional types, like piedmonts and alluvial fans in intermediate sectors, promote run-on processes.

Despite the broadness of hydrological data available about the rainfall-runoff processes in temperate climates areas, Shannon et al. (2002) noted that similar rainfall–runoff processes data in semi-arid environments are still very scarce. Thus, the shortage in detailed information that is recorded, leads to insufficiency in the understanding of these systems. Some of the reasons that have been considered in this deficiency of hydrological data have been listed in order to promote possible ways to address

them. Firstly, there have been some technical difficulties registered in gauging ephemeral stream channels. Secondly, there is a low economic interest in these fluvial systems. Thirdly, runoff mostly occurs with a low relative frequency. Finally, the data at gauging systems is collected on a daily basis, which is an inadequate frequency for flood monitoring, as it would cause the loss of hydrological processes that occur in a within hours.

Similar shortage in semi-arid environment data needs to be addressed, since it has been demonstrated that evaluating flood risks in these areas is as important as the evaluation and understanding of flood risks in other environments. Al-Zahrani et al. (2016) is one of the recent studies that highlighted this issue. There needs to be an understanding of ways to develop these applications in semi-arid regions because hydraulic flood models do not necessarily include the relevant runoff processes. In semi-arid areas, there is one specific process that has proven to be essential in flood wave progression, which is channel bed infiltration. This process is particularly missing from most commercial hydraulic models, and is yet to be thoroughly investigated.

This thesis has selected the dry Valley of Wadi Al Batin, which is located in the eastern part of Saudi Arabia, as a case study to be subject to its investigation. The city of Hafr Al Batin is located in the valley of Wadi Al Batin, a rather dry area. This valley is the main source for the flash flood. According to Al-Zahrani et al. (2016), the city of Hafr Al Batin have been repeatedly hit by flash floods in the recent years, and thus has suffered large number of casualties and significant economic damage.

2.2 Existing infiltration models

This section presents a detailed evaluation and the comparison of the infiltration models, highlighting the underlying presumptions and the modified equation representing each model.

For many years, there have been many attempts to design and implement infiltration models, due to the critical function that infiltration has in each of the water cycle, hydrology, agriculture, and irrigation procedures. However, despite the diversity of these models, Mishra et al. (1999) distinguish between three major categories that encompass all infiltration models. The first category is the physically based infiltration models, which entails models developed on soil physics and adopt the principle of mass conservation and Darcy's law. The second category is the semi-empirical infiltration models, and the final category is the empirical infiltration models.

The physically based infiltration models can be manifested in many instances including the retention relation and the initial and boundary conditions. There has been certainly a development of different models with varying degrees of complexity, which have been basically exhibited in the models of

Green and Ampt (1911), Mein and Larson (1971, 1973), Philip (1957, 1969), Smith (1972), and Smith and Parlange (1978).

The Semi-empirical infiltration model, on the other hand, mediates both the physically based model and the empirical model. These models fundamentally depend on surface water hydrology as a method of the systems approach. Features such as the basic and spatially lumped continuity equations, and infiltration flux–concentration relation hypotheses are utilized in these semi-empirical models. There have been various instances on semi-empirical models in the field. Some of the prominent ones are the models of Grigorjev and Iritz (1991), Horton (1938), Holtan (1961), Overton (1964), and Singh and Yu (1990).

Both laboratory experimental data and the field experimental data form the ground of the empirical infiltration models, such as the SCS-CN, Huggins and Monke (1966), Kostiakov (1932), and also of the modified models of Kostiakov (Smith, 1972) and Collis-George (1977).

An evaluation of the 13 most common infiltration models, which represent the 3 aforementioned categories, has been carried out by Mishra et al. (2003). In addition to this evaluation and based on soil type data that was gathered from field and laboratory experiments, data were compared in terms of performance. Following models such as Green-Ampt, smith and Smith–Parlange Model, are physically bases model. Singh and Yu, Overton, Horton, and Holtan models are semi empirical models. Kostiakov, modified Kostiakov, Huggies and Monke, and Collies are empirical models. Furthermore, the study provided a commentary on the accordance of these models with the soils. These models are as follows:

2.2.1 Green–Ampt Model

The basis of this model is the presumption that soil is formed from uneven tubes, varying in aspects of shape, size, and direction. The model also adopts the assumption that deep soil is homogeneous, has a ponded surface, and holds identical moisture content base. Bouwer (1978) uses the following formula to define the infiltration rate under continuous ponding conditions:

$$f(t) = K_s\left[1 + \frac{H+\psi_f}{L_f(t)}\right] \quad (1)$$

Where $f(t)$ is the infiltration rate per unit area at a certain time [LT^{-1}], K_s is the saturated hydraulic conductivity [LT^{-1}], H is the ponding depth [L], ψ_f is the suction head at the wetting front [L] and $L_f(t)$ is the wetting front progression at time t [L].

2.2.2 The Linear Smith–Parlange Model

This model has been reached based on the following:

$$f(t) = K_s \left[\frac{C}{K_s F(t)} + 1\right] \quad (2)$$

Where $F(t)$ is the accumulated infiltration [L], C is a parameter related to the soil sorptivity [L^2T^{-1}], which differs linearly from the initial moisture and depends on the amount and pattern of rainfall intensity.

2.2.3 The Non-linear Smith–Parlange Model

The non-linear infiltration model of Smith-Parlange was inferred through the following:

$$f(t) = K_s \frac{e^{(K_s F(t)/C)}}{e^{(K_s F(t)/C)-1}} \quad (3)$$

2.2.4 Singh–Yu model

The basis of this infiltration model was built upon these two assumptions: Firstly, the excess infiltration, which implies that the rate of infiltration in the excess of the final infiltration rate; secondly, the rate of excess infiltration is inversely proportional to the nth power of the cumulative infiltration up to that time. This model is mathematically expressed as the following:

$$f(t) = f_c + \frac{a[S(t)]^m}{[S_0 - S(t)]^n} \quad (4)$$

Where f_c is the final infiltration rate [LT^{-1}], $S(t)$ is the available storage for water retention in the soil column at time t [L], $S_0$is the potential storage space available for moisture retention in soil column [L] at the beginning. a, m and n are the coefficient and exponents of the variables $S(t)$ and ($S_0 - S(t)$).

2.2.5 Mishra–Singh Model

This model adopted the SCS-CN method following Horton method for developing an infiltration equation. Just like Horton method, this model assumes a linear variation of the cumulative precipitation with time:

$$f(t) = f_c + \frac{Sk}{(1+kt)^2} \quad (5)$$

Where S is the potential maximum retention [L], and k is the decay infiltration factor.

2.2.6 Smith Model

Based on the assumption of uniform rainfall, this model has been derived accordingly:

$$f(t) = f_c + A(t - t_o)^{-b} \quad (6)$$

Where t_o is the time to ponding, A and b are the parameters which related to the rainfall rate, initial moisture, and the soil type.

2.2.7 Horton Model

This model was based on the presumption that considers the rate of infiltration is relatively proportional to the reduction in the infiltration capacity during rain. However, this assumption is valid if the effective rainfall intensity is greater than f_c. This model was demonstrated as the following:

$$f(t) = f_c + (f_o - f_c)e^{-kt} \quad (7)$$

Where f_o is the f value which is the infiltration rate at the t = 0.

2.2.8 Holtan Model

This model adopted the storage exhaustion concept to reach the infiltration equation which is expressed as follows:

$$f(t) = f_c + a(S_0 - F)^n \quad (8)$$

Where a and n are constants related to the soil type, surface and cropping conditions.

2.2.9 Overton Model

This model expressed its equation as the following, based on the Holtan model:

$$f(t) = f_c\, sec^2\left[(af_c)^{1/2}(t_c - t)\right] \quad (9)$$

Where t_c is the time parameter.

2.2.10 Kostiakov Model

This infiltration model was expressed as the following:

$$F(t) = at^b \quad (10)$$

However, this equation was differentiated by Rode (1965), leading to an infiltration rate that is expressed as the following:

$$f(t) = \alpha(t)^{-\beta} \quad (11)$$

Where $\alpha = ab$, and $\beta = 1 - b$.

2.2.11 Modified Kostiakov Model

The Kostiakov initial model has been reformed and modified by Smith (1972). This modified version of the model was demonstrated as follows:

$$f(t) = f_c + \alpha(t)^{-\beta} \quad (12)$$

2.2.12 Huggins–Monke Model

Through the execution of porosity onto the Holtan model, this model of infiltration was created to be presented as the following:

$$f(t) = f_c + \frac{a(S_0 - F)^n}{\emptyset^m} \quad (13)$$

Where $\emptyset$ is the total porosity, and m is the model parameter and can be determined from the soil property.

2.2.13 Collis-George Model

This model has been derived as follows:

$$f(t) = f_c + \frac{0.5 i_0 \left[1 - \tanh\left(t/t_c\right)^2\right]}{\tanh\left(t/t_c\right)^{0.5}} \quad (14)$$

Where $i_0 = S(t_c)^{1/2}$.

Following reviewing various infiltration models as above in section 2.2, it is determined to use Green-Ampt infiltration model to be implemented and tested with in this research study. Moreover, Green-Ampt is commonly used to estimate the infiltration loss with the modelling process. Green-Ampt assumes a soil profile that is separated by a sharp wetting front into upper saturated zone and lower unsaturated zone. Also, Green-Ampt model has chosen because of the feasibility of obtaining the required soil parameters and the feasibility to be implemented with LISFLOOD-FP hydraulic model.

2.3 Explicit modifications to the implicit GA model

The previous section introduced and evaluated some of the most prominent infiltration models, Due to several factors, mainly the precision and austerity of the model, the Green–Ampt (GA) model, which was set by Green and Ampt (1911), is widely recognized and used in the process of simulating one-dimensional vertical infiltration into the soil. Another factor related to the Green-Ampt model widespread use is noted by Rawls et al., (1982), which highlights the fact that soil physical properties can be employed to determine the parameters in this model.

A thorough process of comparison, review, analysis, and evaluation have been carried out on 9 explicit models that were derived from Green-Ampt model by Ali et al. (2016), who's work depended on various published data sources, i.e., laboratory, numerical and field experiments. These data mainly

featured physical parameters of infiltration. For such measures to be successfully carried out, it was necessary to consider different soil classes and the periods of infiltration.

Some advantages were identified for these explicit approximations over the implicit Green-Ampt models (Ali et al., 2016). The accuracy of the approximation and the simplicity of a computational process, as no iterative computational process is required, are some of the assets. In addition, the ability to these easily to be integrated into hydrological modelling allowing the addressing of a wider range of hydrological problems i.e. the infiltration simulation in rainfall-runoff modelling.

The nine models adopted are: Ali et al. (2013), Almedeij and Esen (2014), Barry et al. (2005), Li et al. (1976), Parlange et al. (2002), Salvucci and Entekhabi (1994), Stone et al. (1994), Swamee et al. (2012), and Vatankhah (2015).

To reach a valid conclusion, Ali et al. (2016) depended on the overall performance index (OPI), considering the explicit models' robust numerical processes and the efficiency of computation. Moreover, computing relative weight of a quantitative statistics in a given soil and infiltration estimates the Overall Performance Index (OPI) and rank of the models. The raking of these explicit models came as follows: Barry et al. model > Parlange et al. model > Vatankhah model > Li et al. model > Almedeij and Esen model > Salvucci and Entekhabi model (1994) > Swamee et al. model > Stone et al. model > Ali et al. model.

Li et al. Model

In this model, the approximation of the implicit Green-Ampt infiltration was derived as:

$$F(t)_{LI} = \frac{1}{2}\left(\frac{S^2}{2K_s}\right)\left[t^* + \sqrt{(t^*)^2 + 8t^*}\right] \quad (15)$$

Where $F(t)_{LI}$ is the accumulative infiltration defined by Li et al. (1976), S is the sorptivity parameter [$LT^{-1/2}$], and $t^*$is the dimensionless infiltration time.

Stone et al. Model

This model derived an explicit solution to Green-Ampt infiltration Equation:

$$K_s t = F(t) - \eta\left(H + \psi_f\right)\ln\left[1 + \frac{F(t)}{\eta\left(H+\psi_f\right)}\right] \quad (16)$$

Where η is the fillable porosity which is equal to $\theta_s - \theta_i$, where θ_s is the volumetric saturated water content and the θ_i is the initial volumetric water content.

Stone et al. (1994) modified the infiltration equation to become as follows:

$$F(t)_{ST} = \frac{S^2}{2K_s}\left[t^* + \sqrt{2t^*} - 0.2987t^{0.7913}\right] \quad (17)$$

Where $F(t)_{ST}$ is the accumulative infiltration defined by Stone et al (1994).

Based on Ali et al. (2016) findings discussed above about the model efficiency, also the feasibility of integrating into LISFLOOD-FP hydraulic model, it has been decided to implement Parlange et al. model and to be tested in this research.

However, it is worth noting that there have been some drawbacks that were attributed to the Green-Ampt Infiltration model. These limitations will be discussed in the following section.

2.4 Green-Ampt Infiltration model limitations

As explained in the previous section, the Green-Ampt infiltration model had many elements that made it the most preferred to be adopted. Yet, and similar to any other model, the Green-Ampt infiltration model has many limitations. This section will feature these limitations and draw special attention to the possible measures to overcome these drawbacks.

There has been a number of challenges and obstacles that have been reported in the application of the Green-Ampt infiltration equation in modelling infiltration during steady and unsteady rainfall events (Kale and Sahoo 2011). Some of the assumptions have been adopted only for the sake of mathematical austerity. For example, the assumption of soil water movement is in the form of a wetting front and there is no effect of diffusion. In contrast to the assumptions made in most Green-Ampt models, the soil profile is hardly ever homogeneous, and the properties associated with soil water that had a direct effect on the infiltration rate, are the water content, water retention characteristics, hydraulic conductivity, and hysteresis.

Moreover, there was one factor that entangled the process of the subsurface flow simulation, which is the variation of antecedent soil moisture conditions within the soil profile resulted from the soil physical characteristic, such as particle size, morphological and chemical properties, and biological activities. As seasons changed, there have been some disparity in the spatial distribution pattern of rainfall, topographical features, and soil types in the elementary watershed. Another difficulty is the scarcity of data on ground surface water retention capacity and antecedent moisture capacity.

Nevertheless, it is explained by Sokol (2003) how the technological advancement made it quite acceptable to rely on the infiltration estimation accuracy, as the radar technology, for instance, allows anticipation of the areal extent as well as the spatial distribution of rainfall. Furthermore, the concise measurement of rainfall intensities can be measured through the various automatic rain gauges with data loggers. Such measurements are made over different time intervals or even at finer temporal scales from the remote area. Finally, it is reported that in recent years the measurement of soil moisture with several sensors is becoming more straightforward.

Consequently, by applying Kowalsky et al.'s (2005) model to the above situation, it would be inconsiderable to register the divergent soil characteristics and its system state. Another advantage can be noted in storing rainfall and soil profile data, which is the efficiency of data storage devices. It is foreseen, however, that the use of a physically based model to account infiltration process will concur the research field related to watershed development and management.

2.5 Evaluation of Digital Elevation Models (DEMs) for flood inundation modelling

As can be inferred from the previous sections, there have been many factors that could have necessitated the conversion to digitalized models of flood inundation. This section examines the effects of various Digital Elevation Models (DEMs) on flood inundation modelling. Afterward, a presentation of the most significant drawbacks that are linked to DEMs will be provided.

As an alternative solution to the high-cost topographical data, Sanders (2007) attempted to reach the flood inundation modelling by examined the digital elevation, and its relation to flood inundation models, the extent to which flood prediction to the digital elevation model type are sensitive, the resolution, and the accuracy. The following DEMs were tackled in the study, the airborne light ranging and detection (LiDAR) data at 1/9 s resolution, airborne interferometric synthetic aperture radar (IfSAR) data at 1/9 s resolution, and shuttle radar topography mission (SRTM) data at 1 and 3 s resolution.

Findings of this study reported that on account of the LiDAR-based DEMs' horizontal resolution and vertical accuracy, which is ~0.1 m, LiDAR-based DEMs are seen as the ultimate source of terrain data for flood modelling. Additionally, it is highly adopted due to its ability to detect bare earth, vegetation and building heights. The DEM 1/9 s NED from the USGS is a valid Digital Terran Model, because it can effectively determine ground heights. In other words, buildings and vegetation are successfully stripped away.

The horizontal resolution of IfSAR based DEMs, which can be obtained commercially or from NOAA/CSC, is very high (1/9 s). Despite the resolution of buildings and bridges features, there must be an additional processing, as these features are DSMs, in order to determine bare earth elevation in urban and vegetated areas.

Radar speckle could lead to noise addition or undulations to flat surfaces, contaminating the IfSAR DEMs including SRTM. Such a noise in flood simulation can manifest flood zone as a network of pools. Moreover, flood modelling is sometimes not valid due to the data gaps that may exist in DEMs based 1 and 3 s STRM. Such data gaps can be the result of the radar shadow.

Despite the high level of smoothness of the terrains mapped by DEMs based on 1/3 and 1 s NED, being truly DTMs, the level of vertical accuracy can be low. Hydrologic modelling is crucial for processing NED in order to have a fair representation of channel and overland flow with many models. However, when compared with other DEMs such as LiDAR, IfSAR, and SRTM, the 1/3 and 1 s NED, flood zones are seen to be as much as 25% smaller. This conclusion highlights the need for highly sensitive and accurate DEMs procedures in the context of flood zone mapping, to prevent underestimation of flood risks.

Among the drawbacks attributed to using the DEMs for flood modelling, Sanders (2007) referred that DEM cannot resolve channels smaller in width than twice the DEM resolution. Thus, the minimum for a crude definition of the cross-section is to consider three survey points, one in the middle and two on both banks of the channel. Thus, an overestimation of the flood level or underestimation of flood speed can be results of not resolving channels. In case of DEMs inaccuracy, ground surveys are recommended on study sites, as they can provide an estimation of the DEM accuracy and can pave the path for ground-truthing the DEM to support data processing.

Another drawback is the direct connection between DEM resolution and flood frequency, in which a higher DEM resolution is required to accurately measure frequent floods (2–10 year events), while in case of less frequent floods (100–500 year events) these features are not crucial.

A third issues is the confusion that might occur between predicting flood extent and the local predictions of water depth and velocity. In other words, these local accurate predictions, which occur in a spatially averaged sense, are different from the successful predictions of flood extent.

On the other hand, some possible effects of different DEMs spatial resolution on raster-based model of flood flow have been registered. These implications have been examined by Horritt and Bates (2001), depending in their investigation on the hydraulic model LISFLOOD-FP for flood river simulation. The sensitivity of the hydraulic model LISFLOOD-FP to the DEM spatial resolution has been exemplified by effecting the flow routing behaviour of the model and the importance of the water storage in the flood plain regions near the channel.

Moreover, it has been explained through the representation of near bank topography at different scales. For the model to accurately illustrate the water storage near the channel the spatial resolution must be raised, which in turn will lead to the retardation of the flood wave caused by this process. It was consequently concluded that the Floodplain topography has a major impact on model performance by the flow routing behaviour through near channel storage effects (Horritt and Bates 2001).

Despite the pivotal role that topography plays in confirming flood inundation areas accurately, high quality topographic DEM date is in fact not accessible in many regions in the United States, and in other many parts of the world. As a result, there has been a thorough inspection of the effects of DEM properties to reach a profound understanding of these effects. It is concluded by Saksena and Merwade (2015) that qualities such as horizontal resolution and vertical accuracy on flood inundation maps can contribute to modelling and mapping of improved flood inundation. Moreover, they considered some errors such as spatial resolution and vertical accuracy to flood inundation and flood inundated area.

In order to create topographic datasets that hold different horizontal resolutions, Saksena and Merwade (2015) followed to the following steps in their research; first, they resampled the DEM data needed for datasets creation; second, they introduced errors that corresponds to coarser resolution and vertical accuracy into the resampled DEMs; thirdly, they used HECGeoRAS and HEC-RAS to model floods and map inundation and finally, the relationships between the DEM properties and flood inundation map extent was developed and validated.

Findings indicated that when compared to higher resolution DEM, a coarser resolution DEM that has an identical number of cells has a higher inundation area. The smoothing of elevations due to DEM resampling increases the total surface as the DEM resolution becomes coarser, resulting in higher water surface elevations and flood inundation extents. As a result, DEM resolution and vertical error have a clear linear relationship with mean water surface elevation and flood inundation area.

The conclusion reached when comparing RMSE of resampled topographic datasets with grid size is that the amount of error and DEM resolution have an inverse relationship. Additionally, it was found that there is a high, positive, linear relationship ($R^2 > 90\%$) that linked the DEM resampling error and DEM grid size. Another result reached is that the elevation of the mean water surfaces indicated strong positive linear relationship with DEM grid size, featuring all the areas included in this research. As the DEM resolution fell, the anticipated flood inundation areas rose, leading to the conclusion that DEMs of coarser resolution over predict the flood extent. Thus, another strong positive linear relationship with the grid size is found with the flood inundation area.

A review of recent studies reveals the increasing lean towards the use of Global digital elevation models (GDEMs) in creating flood hazard maps, which are adopted on a global scale (Dottori et al. 2016, Sampson et al. 2015, and Ward et al. 2013). Nowadays, assessing flood hazard in low-data availability areas is possible because of the GDEMs extensive coverage; nevertheless, their low spatial resolution and vertical accuracy leads to higher chances of under resolution of features.

GDEMs can be used either as digital surface models (DSMs) or as digital terrain models (DTMs). However, because they include features such as trees and buildings on their surface level, GDEMs are mostly classified as (DSMs). There has been a lot of global work undertaken to convert DSMs to DTM products. Some examples of these attempts include the transformation of the Shuttle Radar Topography Mission (SRTM) e.g. Yamazaki et al., (2017)'s Multi-Error Removed Improved Terrain (MERIT), and Lehner et al., (2008)'s Hydrological data and maps based on Shuttle Elevation Derivatives at multiple Scales (HydroSHEDS).

An assessment has been conducted by McClean et al., (2020) to measure the effect of GDEMs on inundation model performance as well as to estimate its impact. This assessment has tested both GDEMs and a national LIDAR product, which would lead to a deeper understanding of these models and their impacts. Moreover, by adopting five spaceborne GDEM products and an airborne LIDAR GDEM product, McClean et al., (2020) were able to compare flood inundations, hydrographs, water depths, and the impacts on hydrodynamic simulations. In an attempt to mimic flood inundation and to address the problem of full shallow water simulation numerically by a Generalised Osher-Solomon Riemann solver, McClean et al., (2020) used Glenis et al., (2018)'s City Catchment Analysis Tool (CityCAT). McClean et al., (2020) reviewed the GDEMs spaceborne products which are:

The first produced was by Farr et al., (2007), Shuttle Radar Topography Mission (SRTM) of NASA. SRTM initially flew in 2000 and is considered the set with the best quality of land elevation observations that is freely available on a global scale. Between 60 degrees north and south, SRTM covers approximately the surface of Earth. In order to measure the distances between Earth and two fixed locations on the instrument, a single satellite was employed. This satellite carried two radar antennas that were connected by a mast for this measurement. The process used interferometry to make the evaluation possible, with a spatial resolution of the SRTM GDEM product reaching 1 arcsecond and a vertical error of 90 % below 9 m.

The second was Yamazaki et al.'s (2017) Multi-Error-Removed-Improved-Terrain (MERIT) DEM. This project attempts to improve the accuracy of SRTM and pays higher attention to flood plains. The project was set to achieve this accuracy through several elimination processes including the elimination of speckle noise from surface reflectance, removing stripe noise from motion errors of the sensor, eradicating absolute bias from limited ground control points, and removing tree height bias, as the radar considers canopies as the land surface, incorrectly. Despite all of the aforementioned attempts, the man-made structures were not removed. It is worth noting that the spatial resolution of Merit GDEM product is 3 arcsecond and its vertical error is 58 % below 2 m.

Another project is Tachikawa et al.'s (2011) Advanced Spaceborne Thermal Emission and Reflection Radiometer (ASTER). This project invested the scientific research satellite, Terra, for the purpose of creating 3 variants of a global DEM. In August 2019, the latest version was released with some additional stereo-pairs in a refined production algorithm. The aim of this version was to reduce artifacts while increasing accuracy and resolution. This ASTER GDEM product has a spatial resolution of 1 arcsecond and a vertical error of 95% below 17 m.

A fourth product is TanDEM-X, and it is a relatively newer project is produced by the German Aerospace Centre, DLR (2018). Despite the availability of the 90 m version, both 30 and 12 m products can be only obtained on demand. According to Earth Observation Center (2018), the product is not fully designed to eliminate outliers, noisy areas, or voids, because it is a new one. Although there have been some primary attempts to modify the original product, a substantial amount of work is required to create a fully hydrologically conditioned product (Archer et al., 2018). This product has a spatial resolution of 3 arcseconds and a vertical error of 90 % below 10 m.

JAXA's Advanced Land Observing Satellite (ALOS) directed its onboard Panchromatic Remote-sensing Instrument for Stereo Mapping (PRISM) to monitor the earth's surface in the period between 2006 and 2011. Tadono et al., (2014) processed the resulting data and utilized it in generating a global DEM at 0.15 arcsecond resolution with a vertical accuracy of 5 m. The spatial resolution of the AW3D30 GDEM product is 1 arcsecond and its vertical error is 5.

Finally, the Ordnance Survey (OS) produced an airborne LIDAR GDEM product, which provides elevation data that are freely available for the UK at 50 m resolution and vertical error of 4 m (Ordnance Survey 2017).

It was ultimately concluded by McClean et al., (2020) that the most suitable product for GDEM to simulate flood inundation is the modified MERIT DEM. This is because the amendments that were applied to this product positively affected flood extent accuracy, which is directly linked to other GDEMs.

2.6 Flash floods in semi-arid environments

In a study of flash floods in semi-arid environments, it is vital to reach a profound comprehension of the relationship between inflow and channel qualities. In this section the interaction between the surface flow and the infiltration as well as incorporating the channel bed infiltration within hydraulic flood routing models will be presented.

Some of the vital elements of the hydrological cycle in the semi-arid regions are the flash floods in the ephemeral river system. Goodrich et al. (1997) explained how it is necessary to consider the explicit

routing methods in order to fully comprehend the relationship between inflow discharge and channel characteristics, which manages the infiltration and downstream discharge within ephemeral river reaches. There have been many models that are explicitly simulating the ephemeral channel rivers. Some of these models adopted full solutions such as El-Hames and Richards (1998) and Mudd's (2006) models, while others adopted partial solutions of the one-dimensional (1-D) St. Venant equations, such as Smith et al.'s (1995) model.

A review of the literature shows that there has been a great deal of research that studied the interaction of surface flows and infiltration, such as the studies of Freyberg (1983), Parissopoulos and Wheater (1991), and Mudd's (2006). The effect of a time-varying hydrograph on the infiltration of flood waters into channel bed sediments, which is a simulated one-dimensional sediment column, was investigated by Freyberg (1983). Results came to confirm that there were similar proportions of infiltrated water and similar duration for equal area hydrographs, yet there were varying peak times. In the same vein, Parissopoulos and Wheater (1991) adopted a two-dimensional infiltration model to extend this analysis. Findings came with some varying data in regarding the different variables of the tested hydrographs. While hydrographs with the same area and duration but varying peak periods had the same overall infiltration volume, hydrographs with the same area but different duration had significant variations in the total volume of water infiltrated.

On the other hand, Mudd's (2006) investigation targeted the impact resulting from the correlation between a flood in an ephemeral channel and infiltration into the channel bed. In order to evaluate the significance of transmission losses on a flood's mass balance, Mudd's (2006) conducted a scaling analysis, which also led him to deduce implications of the bed slope, channel friction, changes in channel geometry, and transmission loss on the momentum equation. He created a numerical model, pairing the one-dimensional Saint-Venant equations and the Richards' equation. The model's numerical simulations have ultimately considered a simplified channel. The aim was to separate the effects of differing channel width, combined flood volumes, and different inflow hydrographs on the spatial distribution of transmission losses and downstream propagation of the flood wave.

Findings of the study reported the significance of infiltration in the mass balance. Moreover, they highlighted the pivotal role infiltration plays in the momentum balance of floods in ephemeral channels at the basin scale (Mud 2006). Moreover, the flood routing schemes adopted to make predictions about flood velocities and propagation distances should be responsible for the momentum loss during flash floods. This is due to the high importance of transmission losses in the momentum balance during flash floods, which can potentially considerably slow floods in ephemeral channels. As a result, this may allow infiltration more time, but it will result in a smaller area of the channel bed being wetted. It was also demonstrated by the numerical simulations that floods holding similar inflow

hydrograph and wider channels have a bigger volume of infiltrated water into the bed sediments. Additionally, it was concluded that a varied proportion of total volume infiltrated will result from floods with similar total volume but of different hydrograph shape. It is anticipated that sharp-peak hydrographs will lead to floods with a larger peak flow velocity and expand further through the channel, when compared with floods that have smoother peaks. Such a result would lead to a greater wetted area and more time for the flood waters to infiltrate into the bed sediments. However, the shape of hydrograph can directly affect the flood proportion, which is infiltrated into bed, yet, if the two channels have identical bed area, the amount of this proportion will be irrelevant to the alterations in channel shape.

In addition to the previous studies, other research papers have been published on the effect of incorporating intensive streambed infiltration. A review of some studies dedicated for this purpose are presented below.

By including a streambed infiltration, Cheng et al. (2015) was able to create a flood routing model, which adopted the Horton equation to estimate the infiltration loss. This model structured a method that is based on experimenting and hit-and-miss approach, in order to enumerate the rate of infiltration. Moreover, this method is designed to investigate the potential movement of the flood wave downstream. Cheng et al. (2015) chose the downstream of the Yuecheng reservoir to the Caixiaozhuang hydrometric station to put this model into application. The Haihe river basin was chosen to be the stream location particularly in the Zhangwei River. Two historical flood events were adopted as replicas, which could be used to verify and evaluate the flood routing. Findings of this experiment proved that the model had a high accuracy level, and thus it could be used for flood routing. However, this implementation should be conditioned by intensive streambed infiltration. Consequently, the model is viable in arid and semiarid zones.

Despite the constructive results recorded, it was proposed that a more precise modelling of streambed infiltration and the movement of the flood wave is needed in further research (Cheng et al. 2015). To be specific, an investigation of the streambed infiltration coupling with a hydraulic flood routing method is required. This approach is particularly needed in shallow stream slope and a notable backwater effect. Finally, the streambed infiltration method can be verified by measuring its rate and using it as a calibration constraint.

In the same vein, a new modelling framework was created by Yang and Chu (2015) for the purpose of creating a simulation that replicates the overland flow dynamics specific to infiltrating surfaces. The framework incorporated various micro topographic characteristics. The implementation of this model

has great potential for depression storage runoff infiltration relationships analysis. It can also be useful for studying the complexity of overland flow and infiltration processes across scales.

Using the complete one-dimensional Saint-Venant equations for 1-D channel flow, Balamurugan and Bhallamudi (2016) developed a model for flood routing in ephemeral channels with compound cross-sections. Different equations are used to simulate each of the surface flow and the sub-surface flow conditions. In the case of the prior conditions, a numerical solution of the complete Saint Venant's equations was used, while for the latter conditions are duplicated by numerically solving the Richards' equation, which is dedicated for unsaturated conditions.

The one-dimensional flow is the only consideration of the suggested model when used in the vertical direction in the soil column. Different soil columns were considered for main channel and flood plains. This consideration makes lateral variation a valid regard in infiltration rate at a cross section. Differences in infiltration rate is subject to many factors including the disparity in flow depth, flood wave arrival times and their underlying differences, and the variations in the soil characteristics.

There are two possibilities in prediction transmission losses as suggested by Balamurugan and Bhallamudi (2016). Depending on the situation, these can possibly be under predicted or over predicted. Therefore, there can be an important effect on the management of water resources in arid regions when the variable infiltration rate with channels with wide flood plains is disregarded. These may also be significant when there is a variation in soil characteristics between the channel and flood plains.

There have been some models, on the other hand that adopted two-dimensional (2D) equations to create an infiltration simulation. For instance, both Horton and Green-Ampt infiltration models were combined with a 2D hydraulic model for surface flow and runoff calculations to create an estimation of infiltration in a watershed by Fernandez Pato et al. (2016). They calculated the runoff volume losses, resulting from infiltration. This calculation was carried out on infiltration that was distributed spatially and temporally, utilizing the empirical laws of Horton and Green–Ampt. The estimated numerical amount of the runoff could be improved by the use of the full 2D shallow water model for the surface flow computation. This is due, in-particular, to a two factors: firstly, it can be facilitated by the combination of the models, the Horton and Green–Ampt models with a 2D surface flow, for the soil infiltration rate to be calculated for each cell, and secondly, the quality of the runoff volume approximation is improved by adopting infiltration maps to consider different soil or vegetation types.

Integrated infiltration models along with flood routing methods can have a significant effect on the overland flow hydrograph. Therefore, Gülbaz et al (2020) dedicated their study to investigate similar

effects, by combining Integrated Horton type of infiltration method equations such as the dynamic, diffusion, and kinematic wave, which represent different forms of flood wave equations. They have also examined the impacts of infiltration through a combination of the kinematic wave type of flood routing method with the Standard Horton, integrated Horton and *Infiltration Index* methods. Moreover, Gülbaz et al (2020) applied MacCormack (1971) explicit computational scheme was used to solve the flood wave equations.

Findings of Gülbaz et al (2020) study concluded with six prominent results. First, it was reported that similar results and peak flows are obtained from the dynamic and diffusion wave solutions for the cases with and with no infiltration. On the other hand, they reported that there are slight differences in the kinematic wave solution results, particularly when peak flow rate values are considered.

The second result was that there was a significant effect on overland flow volume, the peak flow rate, peak flow arrival time and the shape of hydrographs, by the integrated Horton method. Such effects were very evident during light rainfall, while infiltration effects on peak flow rate and peak flow arrival time are significant in double rainfall events.

Thirdly, it was deduced that there are major differences in the overland flow reductions in each of the dynamic, diffusion, and kinematic wave models. In particular, some similarities were seen in models of dynamic and diffusion wave, but there were slight differences with the kinematic wave model.

The fourth results indicated that there are essential impacts on overland flow rates for cases with and without infiltration, caused by rainfall intensity and the shape of the hyetograph. The effect was manifested in an inverted relationship where a rising rainfall intensity led to a reduction of the infiltration effect. Hence, the reduction of overland flow rate resulting from infiltration also dropped. This was due to the infiltration capacity limits.

A fifth conclusion was reached on the differentiation of infiltration models. Upon such comparisons, it was concluded that the infiltration method can significantly affect the shape of the hydrographs. For instance, comparing the Integrated Horton method with Standard Horton method shows that there is a rather small peak flow and late peak flow arrival time in the overland flow hydrograph that accompanies the Integrated Horton method. However, the features of both methods remain very similar. On the other hand, a comparison of Standard Horton and Integrated Horton methods with the index-H method and the index-S method showed a significant fall in both the peak flow and its arrival time. Moreover, the shape of the hydrograph of the index-H method and the index-S method can have a great difference.

Finally, it was reported that one of the critical factors in deciding the soil type is the overland flow because it can have a direct impact on the infiltration capacity limits. Infact, it would be more effective to depend on minimum infiltration capacity to modify the soil type overland flow relation. Since hydraulic conductivity determines the minimum infiltration capacity of the soil, it can be considered as the most important variable in determining soil type. Thus, an increase in one factor leads to a increase in the other.

Another model was created using two-dimensional (2D) hydrodynamic, to be used in shallow water flows but including with high infiltration losses. Based on the cell-centred finite volume method (FVM) framework which is used on unstructured meshes, Ni et al (2020) created a depth-averaged 2D hydrodynamic model. The FVM framework can be used with the three categories of shallow water flows with significant infiltration losses. These categories comprise of surface runoffs of very shallow flows, channel floods with large water depths, and swashes on beaches.

Implementing 2D hydrodynamic model on actual grounds was studied by Ni et al (2020). Through a case study conducted in southern Shanxi Province in China, a real river flood was experimented using the aforementioned model. The experiment denoted the need to incorporate the infiltration loss. This is due to the fact that disregarding the infiltration result would lead to an overestimation of discharge hydrograph, a complication that is hard to be resolved even through the variation of Manning's roughness. Furthermore, some suggestions were made following a sensitivity analysis. The first suggestion highlights the different roles infiltration parameters play in adjusting the flow processes. To be specific, there are notable effects of both, the saturated hydraulic conductivity and initial volumetric water content, whereas very small impacts are attributed to the Manning's roughness and capillary suction head. Secondly, the critical bed sediment size could be greatly changed by the infiltration losses. The critical bed sediment size is created by the flow for incipient motion; thus, it guarantees incorporation when resolving sediment transport and morphological evolution.

Another model that is considered in the current paper is that of integrated, physically based rainfall/runoff and its development, which is used to predict the arid region flash flood. There are three main sub-models that constitute the overall model, which serve varying purposes. By adopting Richard's equation, the first sub-model is responsible for summing up the excess rainfall to replicate one-dimensional infiltration. Afterwards, the second sub-model adopts the kinematic wave theory to address the overland flow routing. For the sake of simulating the effects of the ponded head of runoff, the kinematic wave theory is coupled with the first sub-model.

Finally, in order to solve for channel flow routing the third sub-model presents the complete solution of the Saint Venant equation, coupled with Richards' equation in an attempt of elucidating the losses

of infiltration into channel beds. Consequently, a simulation of dynamic transmission loss is created by this model. This is done while the hydrograph passes downstream through the ponded head in the wadi channel. Yet, one of the drawbacks attributed to this model is its relatively long CPU time it needs to create a full simulation, which is caused by the infiltration component. It is registered that as a result of having ponded head (flooding water) as the upper boundary condition, the average of iterations is 10 per time increment. Furthermore, it is noted that in extreme cases, 4 iterations per time increment are made by the channel routing component. The conclusions reached highlighted the inefficiency of this model for personal computers, because the estimated iterations required to complete the simulation is 1,440,000, considering the fact that there are 10 segments in the channel.

Another consideration of the Green-Ampt infiltration model is its combination with 2D shallow water. A model combining shallow water flow and infiltration was used in Tügel et al.'s (2020) investigation. They inspected whether it is possible to estimate the Green-Ampt parameters accurately, depending on average values available in the literature and based on the soil texture classes that are available. They have also investigated the factors leading to a faulty representation of infiltration with tabulated Green-Ampt parameters. Such factors include surface clogging, sub-grid rill-flow, and coarse DEM resolution.

The study of Tügel et al. (2020) relied on varied small-scale test cases that have accessible calibration data to study the overall suitability of using average Green-Ampt parameters based on the soil texture classes. Two of these tests are lab-based experiments, while one of them is an experiment of rainfall-runoff conducted on a small plot in Senegal. The study also utilized a case study that is made on flash floods in a desert in Egypt. The findings manifested an underestimation of the infiltration rates with average Green-Ampt parameters in the experiments conducted in the laboratory. However, there was an overestimation of rates in Senegal's infiltration that were deduced from the field experiment. Similarly, the case study in Egypt showed that the rates of measured infiltration from double ring infiltrometer tests and those with Green-Ampt parameters showed an overestimation of the model. It is essential that a precise representation of the natural conditions in the area of Egypt is actually provided. For this reason, plot-scale rainfall-runoff experiments are set to be carried on, supported by the use of a rainfall simulator. Moreover, this will allow for a better comparison of the infiltration rates available in the literature with the measured infiltration rates and the test of double ring infiltrometer.

identification of the peak discharge and volume of a catchment is of critical importance to determine the largest flash flood. This consideration has been noted in some studies. For instance, the results of Weiler et al. (2020) highlighted the importance of analysing the spatially and temporally controlled superimposition of runoff formation and runoff concentration, including the possibility of overland

flow infiltration along the flow path and depression retention. The importance of this is because of the great impact this analysis can have on modelled peak discharge and discharge volume for a given catchment.

In their attempt to finalize runoff concentration, Weiler et al. (2020) designed a method that has interactive spatial explicit features. This method coupled the potential variables of soil moisture and rainfall for runoff formation with hydraulic assumptions. This would lead to flash floods promoted by the corresponding design hydrographs and the specific conditions catchment. The effect of obtaining this information is manyfold. Firstly, it would facilitate creating risk maps of flash floods. Additionally, adequate catchment-specific information for heavy precipitation risk management can be presented. Thus, it can be concluded that in order to forecast floods for a specific return period, there should be a consideration of the factors affecting flood formation and concentration, and their implementation into a statistical framework, particularly where different runoff generation mechanisms occur at the same time.

Itzï is a more recent model, which is dynamic hydrologic and hydraulic based, and is created specifically to replicate a two-dimensional surface flow. Courty et al (2017) presented the Itzï model in their study, which adopts the joint tool of partial inertia numerical scheme simple rainfall-routing system. It is noteworthy that there is a tight connection of the tool with the open-source GIS GRASS, facilitating the management of input and output data of varying resolutions. Additionally, it demystifies data with different space and time in the form of raster time series. Such elements include precipitation or friction coefficients. Hodgson and Bresnahan (2004) referred that through two analytic benchmarks, the validity of the numerical scheme has been indicated. This has led to RMSEs 1 to 2 orders of magnitude lower than the airborne lidar vertical accuracy.

One of the attempts to improve the Green-Ampt model is the modified model of Zhang et al. (2020). They investigated the quarter-elliptic wetting profile effect on the model parameters, which are manifested in the hydraulic conductivity and wetting front suction head. Through their attempt, Zhang et al. (2020) were able to validate their modified version of the Green-Ampt model.

One of the important parameters in the Green-Ampt model, as referred by Zhang et al. (2020), is the scaling quantity. This can be manifested in the ratio of the saturated zone depth to the wetting front depth as one of the instances of this parameter, which describes the variation in the average hydraulic conductivity with the wetting profile. There were many areas that were explored by the researchers to validate the upgraded Green-Ampt model. They investigated the registered results of the traditional Green-Ampt model and HYDRUS-1D.

They have also examined the related experiments in the literature to provide an extensive comparison of these models with the modified Green-Ampt model. Moreover, some indicators were adopted to evaluate the performance of the model; such indicators include the root mean square error, percent bias, and Nash-Sutcliffe efficiency coefficient. Based on this evaluation, Zhang et al. (2020) were able to reach several significant results. They reported that the modified Green-Ampt model's performance was "*excellent*" or "*near-excellent*", whereas the wetting front depth results of the HYDRUS-1D were unsatisfactory, as it disregarded the entrapped air bubbles that occurred in the soil pores. On the other hand, there were positive results associated with the infiltration rate and accumulative infiltration performance. Intriguingly, the traditional Green-Ampt model performance was poorer than the modified one, as the latter adopted the sharpened piston profile. Consequently, it is concluded that a better estimation of the infiltration process can be reached through the updated Green-Ampt model.

2.7 Conclusion

To conclude, this chapter has provided a comprehensive description of common infiltration models based on studies from the related literature. It first presented a comparison of some existing infiltration models, featuring 13 of the most common models, which were mainly categorized as the physically based, the semi-empirical, and the empirical infiltration models. These models include Green–Ampt Model, The Linear Smith–Parlange Model, The Non-linear Smith–Parlange Model, Singh–Yu model, Mishra–Singh Model, Smith Model, Holtan Model, Overton Model, Kostiakov Model, Modified Kostiakov Model, Huggins–Monke Model, and Collis-George Model. Information such as the models' underpinning asumptions and equations were evaluated through this comparison.

Following this there was a presentation of some notable explicit modifications to the Green–Ampt (GA) model, which led to deriving 9 models, namely: Barry et al. model, Parlange et al. model, Vatankhah model, Li et al. model, Almedeij and Esen model, Salvucci and Entekhabi model, Swamee et al. model, Stone et al. model, and Ali et al. model. In this section both, the strengths and limitations of Green-Ampt Infiltration model were highlighted.

Next was presented a discussion on the trending inclination towards the Digital Elevation Models (DEMs) for flood inundation modelling, and presented an evaluation of these models accordingly. The section sheds light on the most critical effects of DEMs on flood inundation modelling, raster-based model of flood flow, and flood risk analysis in cities. Additionally, there was a description of some notable limitations associated with these DEMs. These were contrasted with literature supporting the use of Global digital elevation models (GDEMs) in creating flood hazard maps, as a solution of data

unavailability in different parts of the world. In order to measure the effects of these GDEMs, six products were adopted, five spaceborne GDEM products and an airborne LIDAR GDEM product.

Furthermore, the chapter reviewed the literature about flash floods in semi-arid environments, focusing on the interaction between the surface flow and the infiltration, the channel bed infiltration within hydraulic flood routing models, and the effect of incorporating intensive streambed infiltration. Flood routing models' simulations included a variety of equations ranging between one-dimensional and 2-dimensional (2D) equations. Many related models have been presented to support the effectiveness of the simulations created. Finally, some related studies were included to incorporate the different aspects of infiltration simulations such as the overland flow dynamics specific to infiltrating surfaces, flood routing in ephemeral channels with compound cross-sections, and shallow water flows with significant infiltration losses.

Chapter 3 - Model Case Study: Setup and Sensitivity Analysis

3.1 Introduction

In semi-arid zones such as in Saudi Arabia, flash floods are considered as the most catastrophic natural hazard events which lead to significant danger to lives and properties. Flash floods are caused by excessive rainfall in short periods of time and are affected by various factors such as the physical and the hydrological characteristics of the river catchment including slope, soil and land use type. Therefore, all measures, strategies, and emergency response plans to cope with the flooding rely on robust flood simulation.

The topographical data is crucial element for flood inundation modelling, however getting access to high resolution topographical data is not always possible for many countries due to budget constraints (Neal et al., 2012).

The aim of this chapter is to investigate the implications of channel bed infiltration to the wave propagation in an ephemeral river system. This has been carried out with flood inundation modelling of Wadi Al Batin in Saudi Arabia using the two-dimensional shallow water equation based model, LISFLOOD-FP, and applying various infiltration scenarios, various topographical spatial data and different channel Manning's friction coefficient. Furthermore, the sensitivity of the LISFLOOD-FP flood inundation model to the various topographical data is investigated and determined. It is also studied whether a higher spatial resolution digital elevation model (DEM) for Wadi Al Batin will lead to more efficient flash flood prediction in the ephemeral system.

3.1.1 Research steps

The following research steps have been conducted in order to achieve the aim of this chapter:

1. Setting up the 2D flood inundation model and the data required for running LISFLOOD-FP on Wadi Al Batin.
2. Running LISFLOOD-FP simulations with various DEs spatial resolutions and different infiltration loss scenarios in order to investigate the implications of channel bed infiltration, as well as the DEM spatial resolution, on flood wave propagation characteristics such as the flood travel time, the flooded area and the flood water volume. The two infiltration scenarios are no infiltration loss scenario, and various range of constant infiltration loss applied to the simulation domain. The various DEM spatial resolution are 85 m, 171 m, 257 m, 343 m, 429 m and 515 m.

3. Carrying out a sensitivity analysis for LISFLOOD-FP with different channel Manning's friction coefficient in order to estimate the effect of channel Manning's friction coefficient on flood wave propagation characteristics in the ephemeral system.

3.2 Methodology

The methodology used to achieve the objectives of this chapter is by use of LISFLOOD-FP to simulate the floodplain extent in the Wadi Al Batin, focusing on a 2-D model structure without channels. The Multi-Error-Removed-Improved-Terrain (MERIT) DEM produced by Yamazaki et al. (2017) was used in order to investigate the effect of the DEM spatial resolution on flood wave propagation. The LISFLOOD-FP hydraulic model was applied to 65 km of Wadi Al Batin, for an 8 day period where the flood wave is expected to pass through. Different infiltration loss scenarios, as well as channel Manning's friction coefficients applied to the simulation in order to investigate their effect on flood wave propagation characteristics.

3.2.1 Case study:

Located in the North-eastern region of Saudi Arabia, the City of Hafar Al Batin as shown in Figure 3.2.1 suffers from major floods during short duration high rainfall events. The climate in the study area is a desert climate Unlike rainfall in hydrologic models, which is a main input, rainfall in arid and semi-arid regions is distinguished by a great deal of temporal and spatial variation, occurring in short and intense intervals. These characteristics are the major factors of local flash flooding in these areas. According to Camarasa-Belmonte and Soriano-García (2012), arid and semi-arid regions have a deficiency in typical flood control hydrologic and hydraulic structures, due to the irregular and infrequent rainfall. Such shortage in structures is one of the reasons why the rare flooding events may have a more drastic effect on the cities of these regions.

In addition to the above factor, standard statistical techniques are not available to estimate storm frequency, which is essential in flood control structure design. This is due to the absence of records containing high-quality rainfall data in some regions. In Saudi Arabia, the highest level of annual rainfall is found in the south-western region and the north-western region, particularly in Hafr Al-Batin (Hasanean and Almazroui 2015). It is reported that despite the scarcity of detailed high-quality rainfall data for Hafr Al-Batin, it is registered that the average annual rainfall is about 125 mm whilst the whole country's annual rainfall average ranges between 5 and 230 mm (Al-Zahrani et al. ,2016)

Hafr Al Batin watershed consists of three main streams as shown by Figure 3.2.2 which are the main source of runoff in Wadi Al Batin. The largest stream is called Wadi Al Batin flows from the southeast to the northwest. The second stream is called the North Fleaj which flows from the north to south, and the third stream is the South Fleaj stream which runs from south to north. Hafr Al Batin city is in

an area where these three streams meet, which means Hafr Al Batin city is considered at a high risk of flooding.

This area has been chosen as a case study, due to several floods hitting the city of Hafr Al-Batin, which caused numerous losses of human life, damage to the public, private properties and the economy. Furthermore, it is located within semi-arid region and Wadi Al Batin is an ephemeral river system.

Figure 3.2.1 The location of the study area.

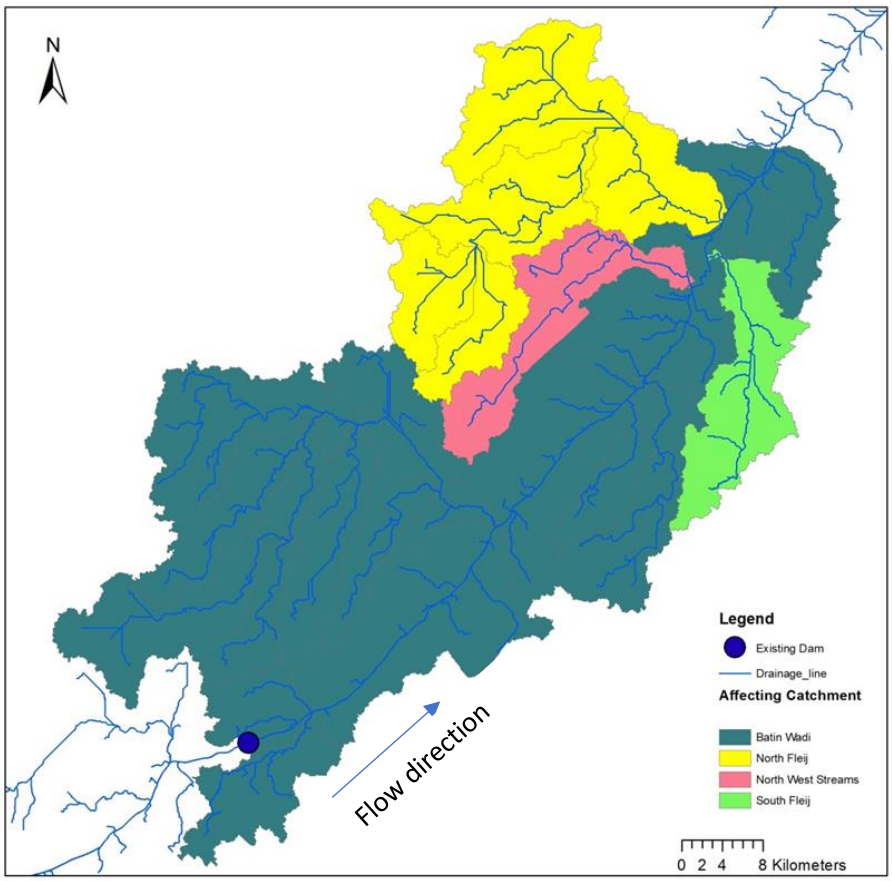

Figure 3.2.2 shows the delineation of the main catchments in the study area.

3.2.2 Description of the flood inundation model

The LISFLOOD-FP model (Bates et al., 2013) used in this research is a raster-based inundation model which is mainly based on solving an inertial formulation of the shallow water equations (SWE) to simulate the flood wave propagation along the channels and the floodplains. The SWE equations are derived from two equations (Eq 1 and 2) that govern the continuity of momentum between cells as well as the continuity of mass in each cell. The momentum and the continuity equations for the full 1D full shallow water equations are as below (Cunge et al.,1980)

$$\frac{\partial Q_x}{\partial t} + \frac{\partial}{\partial x}\left(\frac{Q_x^2}{A}\right) + gA\frac{\partial (h+z)}{\partial x} + \frac{gn^2\, Q_x^2}{R^{4/3}A} = 0 \qquad (1)$$

$$\frac{\partial A}{\partial x} + \frac{\partial Q_x}{\partial x} = 0 \qquad (2)$$

Where A is the flow cross section area in m^2, h is the water depth in (m), z is the bed elevation in m, Where Q is the flow between the cells in m^2s^{-1}, g is the acceleration due to the gravity in (ms^{-1}), and R is the hydraulic radius in (m).

The LISFLOOD-FP model solves a simplified form of the SWE by neglecting the advection term, but retaining the inertial term, and is often referred to as an inertial or acceleration solver (Bates et al., 2010).

LISFLOOD-FP model simulates two-dimensional flow over the raster grid, (Bates et al., 2010) calculating the flow Q between the cells using the equation 1

$$Q = \frac{q - gh_{flow}\,\Delta t \frac{\Delta(h+z)}{\Delta x}}{1 + gh_{flow}\Delta t n^2 |q| / h_{flow}^{10/3}} \Delta x \qquad (3)$$

h_{flow} the maximum depth of flow between cells and defined as the difference between the highest water free surface in the two cells and the highest bed elevation, x is the grid cell width in (m), t is the time in (s), q is the flux between cells, and n is Manning's roughness coefficient.

The cell water depth is estimated using the equation 2

$$\frac{\Delta h^{i,j}}{\Delta t} = \frac{Q_x^{i-1,j} - Q_x^{i,j} + Q_x^{i,j-1} - Q_y^{i,j}}{\Delta x^2} \qquad (4)$$

Where i and j are the cell coordinates in x and y directions. The equation used for calculation of time step within LISFLOOD-FP is based on Courant-Friedrich-Lewy (CFL) condition.

$$\Delta t = \alpha \frac{\Delta x}{\sqrt{gh}} \qquad (5)$$

Where α is a coefficient that ranges between 0.2 to 0.7 for most floodplain scenarios (Bates et al., 2010). This coefficient enhances LISFLOOD-FP robustness (Coulthard et al.,2013). Equation 5 shows that the time step is strongly controlled by the grid cell size and the water depth. LISFLOOD-FP (Bates et al., 2013) was chosen as a suitable model for this research because it is open source, computationally efficient, multiple dimensional and commonly used with in the hydrodynamic community. Furthermore, LISFLOOD-FP model has been tested and showed good results in flood inundation modelling in various regions in Europe (Bates et al., 2010), West Africa (Neal et al., 2012), Southern Africa (Schumann et al., 2013), North Africa (Yan et al., 2014) and the Amazon (Wilson et al., 2007).

3.2.3 Application of the LISFLOOD-FP model

LISFLOOD-FP model setup

A 2D LISFLOOD-FP model was set up for 65 km of Wadi Al Batin. LISFLOOD-FP requires input data such as the floodplain topography, which is represented by the ground digital elevation model DEM, the boundary conditions such as the discharge to inflow point to the domain and the friction parameters.

The Multi-Error-Removed-Improved-Terrain (MERIT) DEM produced by Yamazaki et al. (2017) was used as an input floodplain topography for LISFLOOD-FP. The MERIT DEM was retrieved as an enhanced product from the existing space borne DEMs such as Shuttle Radar Topography Mission SRTM and AW3D-30m. The MERIT DEM has a spatial resolution of 3 arcsecond and a vertical error of 58 % below 2 m.

(Yamazaki et al., 2014) has processed the existing SRTM and AW3D DEMs by eliminating the major error components by using various satellite data and filtering techniques. (Yamazaki et al., 2014) removed the speckle noise, stripe noise, absolute bias, and the tree height bias of the existing SRTM and AW3D DEMs.

McClean et al., (2020) concluded that the corrections applied to the MERIT DEM had a positive effect on flood extent accuracy, relative to other GDEMs, making it the most appropriate choice of GDEM for flood inundation simulation.

All the input data were created in ArcMap software and projected in the Universal Transverse Mercator system (UTM zone 38 N), apart from the discharge inflow point to the domain and the Manning's friction coefficient. All the raster data sets were exported in ascii format in order to be read by LISFLOOD-FP.

The boundary conditions are usually obtained from local ground gauges as well as the output from hydrologic models. The Manning's friction coefficient is a parameter which characterises the river channel and the floodplain flow resistance. Friction parameter values are usually obtained from a lookup table or calibrated data. The boundary condition data for LISFLOOD-FP model domain is shown in the Table 3.2.1.

Table 3.2.1 The model boundary conditions.

Upstream boundary		**Downstream boundary**			
N (m)	E (m)	N (m)	E (m)	QFIX (m^3s^{-1})	Slope
3099067	550861	3158483	601828	0.582231	0.0006

Where QFIX is the constant discharge inflow into the domain which simulate the steady state flow at the model's upstream and considered as mass flux per unit width in m^3s^{-1}. Therefore, the peak magnitude discharge inflow is 200 m^3/s, this been chosen as an arbitrary inflow. The slope of 0.0006 has defined as the overall valley slope retrieved from the DEM. N and E are the northing and easting in the UTM coordinate system.

LISFLOOD-FP model simulations sensitivity tests

Four sets of sensitivity tests were conducted with LISFLOOD-FP. These sensitivity tests are to the floodplain DEM resolution, infiltration loss, the Manning's friction coefficient and variable magnitude inflow hydrograph and duration.

Firstly, in order to test the effect of the DEM spatial resolution on LISFLOOD-FP model performance and the flow routing behaviour, 6 different 2D floodplain models were built. The most detailed model has a spatial resolution of 85 m. Other 2D simulations have run at 171 m, 257 m,343 m, 429 m and 515 m resolutions. These simulations were run to determine and analysis the evolution of the flow propagation travel time, the flooded area, and the water volume versus various DEM spatial resolution.

A mean resampling method aggregating the mean value was applied on to the initial DEM 85 m spatial resolution to derive DEM with spatial resolution of 171 m, 257 m, 343 m, 429 m, and 515 m.

Secondly, the LISFLOOD-FP sensitivity analysis to various infiltration loss scenarios was undertaken. These tests were carried out to determine the effect of the infiltration loss on the flow propagation characteristics, such as the flow travel time and the flooded area. These scenarios where no infiltration loss and other scenarios where a range of constant infiltration rate were applied to the LISFLOOD-FP run simulation. Helali (1993) used a double ring infiltrometer experiment within 50 surface soils of three different texture classes to determine the infiltration rate. Helali (1993) has stated that the infiltration rate of the loam soils texture class, which is the dominant soil texture within Al Batin River catchment, ranges from 2.8 cm/h to 6 cm/h.

Thirdly, the LISFLOOD-FP sensitivity analysis to different floodplain Manning's friction coefficient ranging from 0.01 to 1 was also tested, in order to assess the effect of Manning's friction coefficient on the flow routing behaviour and the flow propagation characteristics such as the travel time and the flooded area.

Lastly, various inflow magnitude hydrographs of 1200 m^3/s, 1500 m^3/s and 1800 m^3/s have been applied. Moreover, a doubled duration hydrograph has been applied as a part of the sensitivity analysis.

3.3 Results and discussion

In this section, LISFLOOD-FP simulations results will be presented and discussed. The effect of various DEM spatial resolution, different infiltration scenarios, different floodplain Manning's friction coefficient and various magnitude and duration inflow hydrographs on the simulated travel time and the flooded area will be presented and discussed.

3.3.1 Effect of DEM sptial resolution

Several LISFLOOD-FP runs were carried out on with DEM spatial resolution of 85 m, 171 m, 257 m, 343 m, 429 m to 515 m. All the other simulation parameters were kept the same. Manning's friction coefficient was set constant at 0.06 and no infiltration loss was applied.

Figure 3.3.1 and Table 3.3.1 show an increase of 2.99 km^2 in the flooded area when the full simulation domain becomes wet from 75 km^2 at the spatial resolution of 85 m reaching to 77.99 km^2 at the spatial resolution of 343 m. Furthermore, Figure 3.3.1 and Table 3.3.1 show an increase of 6.69 km^2 in the flooded area from 77.99 km^2 at the spatial resolution of 343 m reaching to 84.69 km^2 at the spatial resolution of 515 m.

This is mainly related to increase of bed elevation along with increasing the DEM cell size as result of smoothing due to the DEM resampling process as also found by Saksena and Merwade (2015). Therefore, this leads to higher water level which results in a greater flood extent. The higher percentage increase in the flooded area at the resolution of 429 m and the resolution of 515 m is due to the greater impact of the DEM smoothing process resulting from the resampling by aggregating the mean at coarse spatial resolutions of 429 m and 515 m.

Furthermore, Figure 3.3.1 shows monotonically increasing line pattern at 85 m, 171 m, 257 m and 343 m DEM, however the line pattern becomes steep at 429 m and 515 m DEM. This is might be because of the higher distortion in the DEM as a results of the resamplig process to high cell size DEM.

Therefore, the increase in flooded area along with increasing the DEM cells size, leads to over-prediction of the simulated flooded area as well as over prediction in the flood risk.

Also, Figure 3.3.2 and Table 3.3.1 show a decrease of 28.75 hours in the flow travel time when the full domain becomes wet from 149.75 hours at the resolution of 85 m reaching to 122 hours at the resolution of 343 m, when applying the resolution of 85 m, 171 m, 257 m and 343 m.

This decrease in travel time might also be related to the resampling process to a coarser DEM resolution. This averaging process might cause the micro-topographic flow paths to be

underestimated within the coarser DEM. Therefore, this simpler flow path leads to quicker simulated travel time with the 2D simulation domain. Thus, potentially a less reliable flood risk assessment.

However, Figure 3.3.2 shows a conversely line pattern increases of 12.25 hours in the flow travel time from 121 hours at the resolution of 343 m reaching to 133.25 hours at the resolution of 515 m, when applying the DEM spatial resolution of 343 m, 429 m and 515 m. This increase in the flow travel time is again due to the greater distortion in DEM resulting from the resampling by aggregating the mean at a coarse DEM resolution of 429 m and 515 m.

Lastly, the effect of various DEM spatial resolution on LISFLOOD-FP simulations results show that higher resolution will lead to more precise estimations of the simulated flow travel time and the flooded area. Therefore, leading to a more robust flood risk assessment, prediction and developed resilience emergency measures from the local authorities.

Table 3.3.1 The evolution of flow travel time and the flooded area versus of various DEM spatial resolution at 0.06 Manning's friction coefficient and no infiltration loss

DEM resolution (m)	**Travel time (h)**	**Flooded area (km^2)**
Dem_85	149.75	75.002
Dem_171	132.75	76.255
Dem_257	122.00	77.922
Dem_343	121.00	77.996
Dem_429	131.50	82.229
Dem_515	133.25	84.692

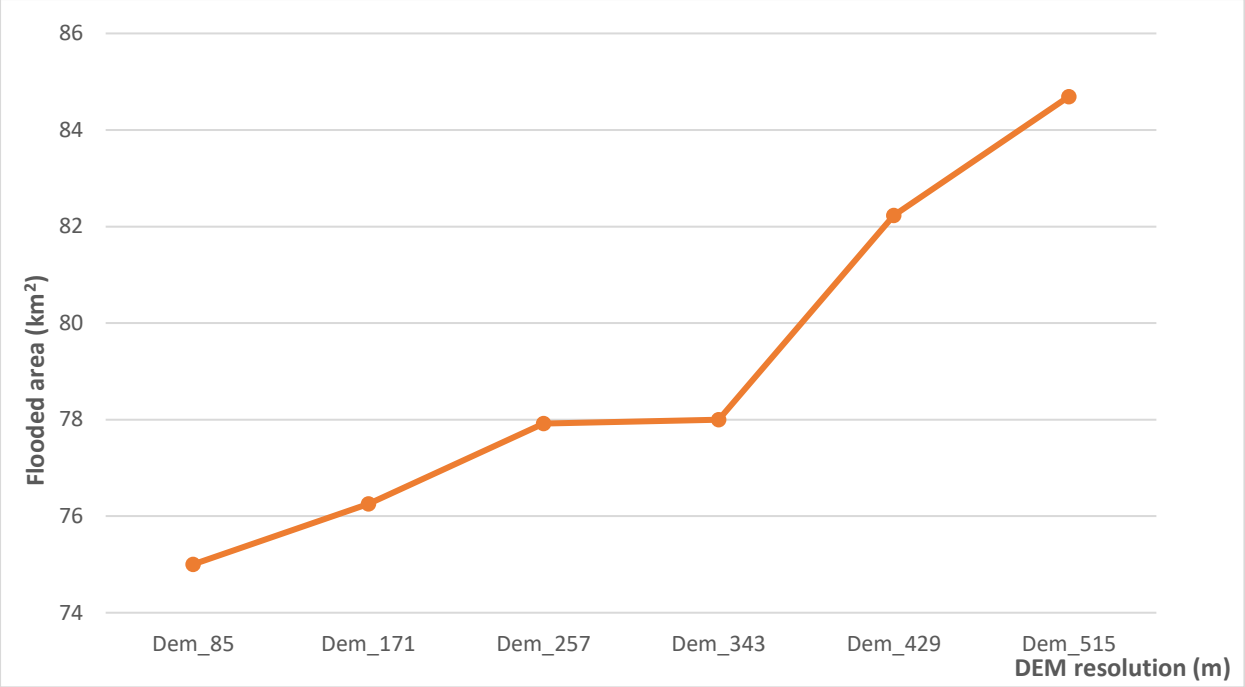

Figure 3.3.1 The evolution of flooded area versus of various DEMs spatial resolution at Manning's friction coefficient of 0.06 and no infiltration loss.

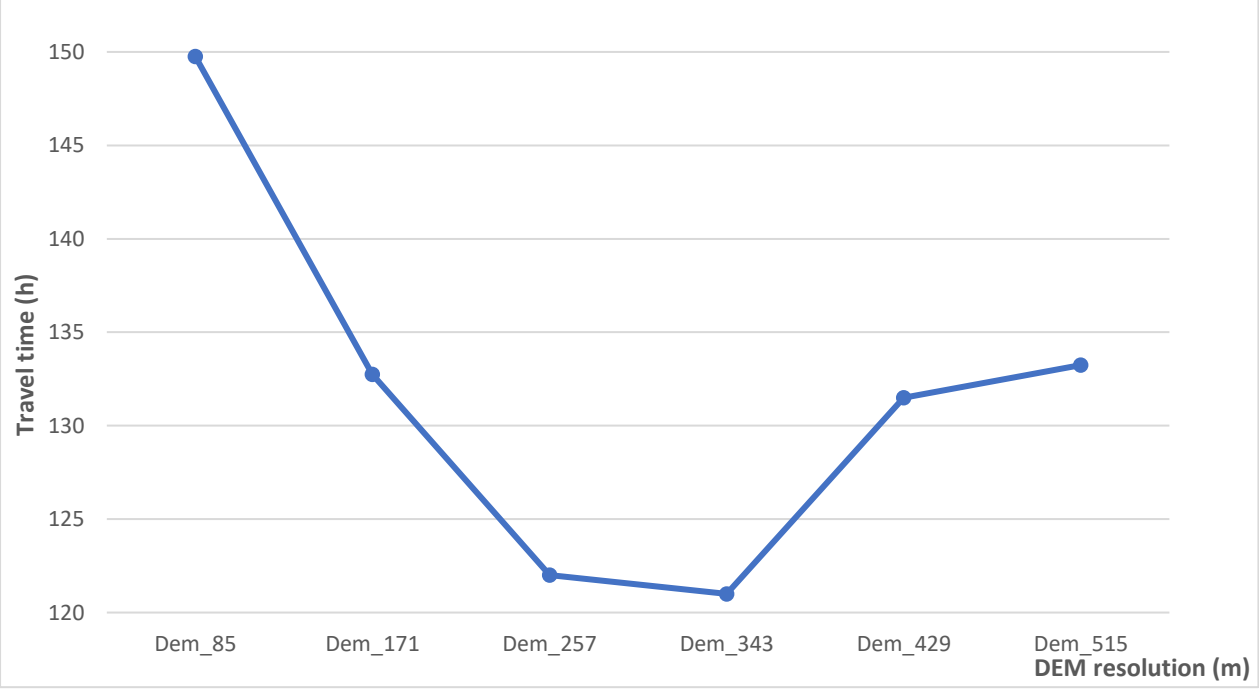

Figure 3.3.2 The evolution of travel time versus of various DEMs spatial resolution at Manning's friction coefficient of 0.06 and no infiltration loss.

3.3.2 Effect of Manning's friction coefficient

In order to assess the model sensitivity and the effect to floodplain Manning's friction coefficient, the previous LISFLOOD-FP simulations as described in the section 3.2.3 were run again while applying a wide range of channel Manning's friction coefficient of 0.01 to 1, each run with no infiltration loss. All the other parameters are kept the same as the previous simulations runs as in the section 3.2.3 including the DEM spatial resolutions of 85 m, 171 m, 257 m, 343 m, 429 m, and 515 m.

Figure 3.3.3 and Table 3.3.2 show an increase in the flow travel time of 87.25, 83.25, 83.75, 84.75, 84.75 and 87.75 hours for the full simulation domain becomes wet at the DEM spatial resolution of 85 m, 171 m, 257 m, 343 m, 429 m, and 515 m respectively. This increase in the flow travel time when increasing the Manning's friction coefficients is because of the flow travel time is linked to the flow resistance. Higher surface roughness causes an increase in the water level, which leads to reduce in the flow velocity. Therefore, a longer flow travel time, while conversely a lower surface roughness causes a shorter flow travel time.

Figure 3.3.3 shows the simulated travel time pattern of increasing with increasing the Manning's friction coefficients are similar at the various DEM resolutions mentioned above. This might indicate an approximate credibility of this results discussion.

Table 3.3.2 The evolution of flow travel time versus of various DEM spatial resolution and Manning's friction coefficient ranging from 0.01 to 0.1.

DEM Resolution (m)	**Travel time (H)**									
	Manning (0.01)	Manning (0.02)	Manning (0.03)	Manning (0.04)	Manning (0.05)	Manning (0.06)	Manning (0.07)	Manning (0.08)	Manning (0.09)	Manning (0.1)
85	92.25	108.25	121	132.25	141.25	149.75	158	165.50	172.75	179.50
171	78.25	93.25	105	115.25	124.25	132.75	140.75	148.00	155.00	161.50
257	67.75	82.25	94	104.25	113.5	122	130	137.50	144.50	151.50
343	66.25	81	92.75	103.01	112.5	121	129.25	136.75	144.25	151.00
429	76.5	91.5	103.50	113.75	123.00	131.5	139.50	147.00	154.25	161.25
515	76.5	91.75	104.00	114.51	124.25	133.25	141.50	149.50	157.00	164.25

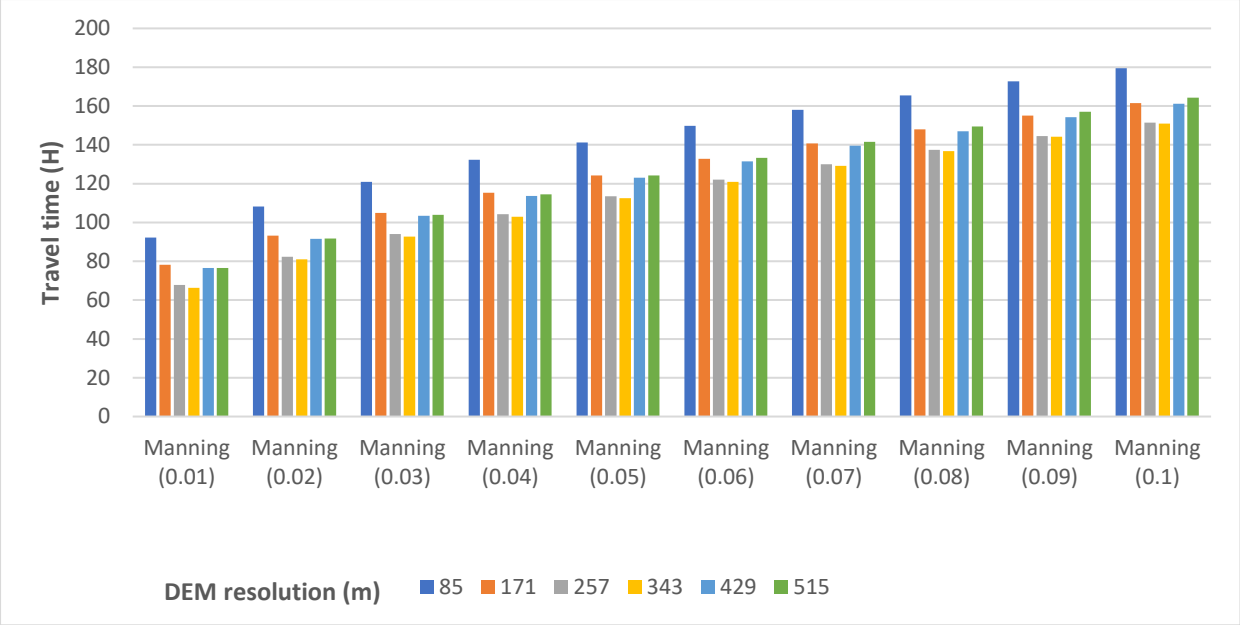

Figure 3.3.3 The evolution of flow travel time versus of various DEM spatial resolution and Manning's friction coefficient ranging from 0.01 to 0.1.

Furthermore, Figure 3.3.4 and Table 3.3.3 show a maximum increase of the flooded area of 23.63 km^2, 23.39 km^2, 22.9 km^2, 20.18 km^2, 18.81 km^2, and 17.79 km^2 in the flooded area when the full simulation domain becomes wet at the DEM spatial resolution of 85 m, 171 m, 257 m, 343 m, 429 m, and 515 m.

This increase in the flooded area when increasing the Manning's friction coefficients is again due to the impact of the flow resistance which is the surface roughness. The higher surface roughness causes a decrease in the flow velocity, and thus an increase in the water level which leads to a greater flooded area.

Again, Figure 3.3.4 shows this increase pattern in the simulated flooded area is similar to various DEM resolutions applied to the model. Therefore, again, this might give an indication of this discussion credibility.

Table 3.3.3 The evolution of flooded area versus of various DEM spatial resolution and Manning's friction coefficient ranging from 0.01 to 0.1.

DEM Resolution (m)	**Flooded area km²**									
	Manning (0.01)	Manning (0.02)	Manning (0.03)	Manning (0.04)	Manning (0.05)	Manning (0.06)	Manning (0.07)	Manning (0.08)	Manning (0.09)	Manning (0.1)
85	57.501	63.42	67.66	70.76	73.13	75.00	76.97	78.55	79.94	81.13
171	58.939	64.60	68.47	71.54	73.84	76.26	78.44	79.56	80.83	82.33
257	60.532	65.98	69.89	72.35	75.60	77.92	78.85	80.11	82.10	83.43
343	64.19	69.15	71.15	73.28	76.11	78.00	80.36	82.01	82.95	84.37
429	69.692	74.49	77.07	79.65	81.12	82.23	83.89	85.92	87.39	88.50
515	73.01	77.52	79.12	82.57	84.43	84.69	86.82	88.41	89.74	90.80

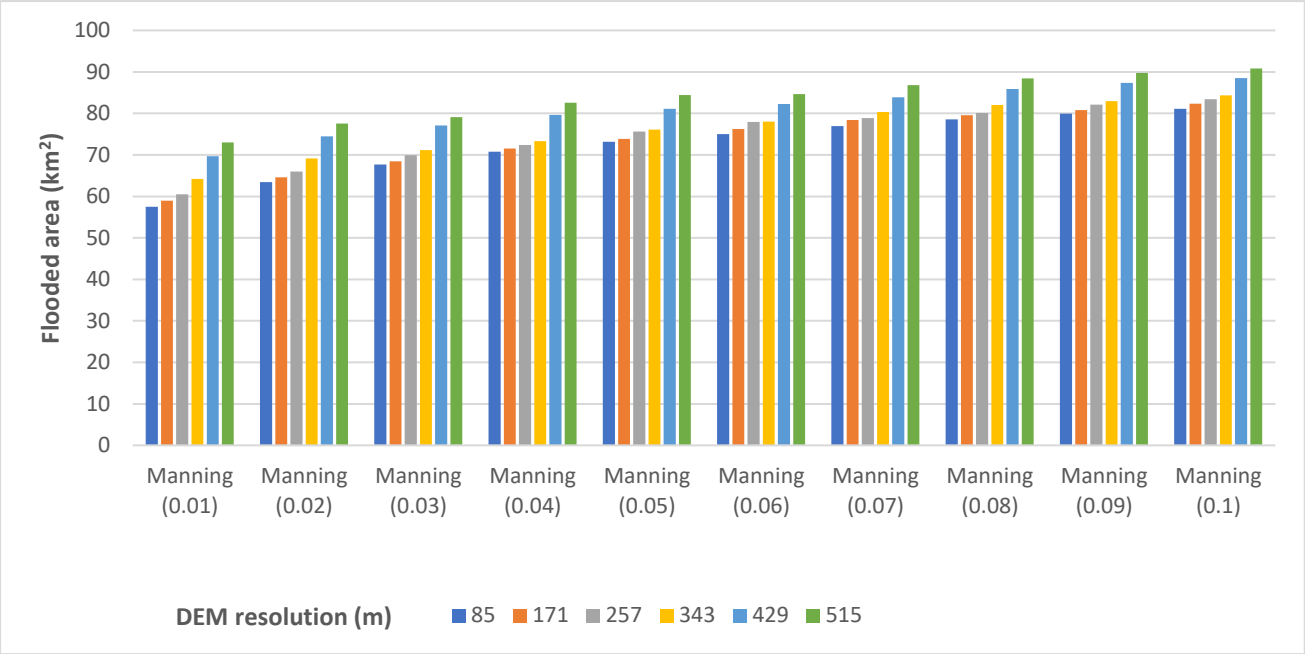

Figure 3.3.4 The evolution of flooded area versus of various DEM spatial resolution and Manning's friction coefficient ranging from 0.01 to 0.1.

3.3.3 Effect of constant infiltration

As a part of studying the implications of the infiltration on the flow wave propagation characteristics, a wide range of constant infiltration has been applied to the model. The chosen constant infiltration rate values are 0 cm/h, 2.8 cm/h, 3 cm/h, 3.1 cm/h, 3.5 cm/h, 3.9 cm/h, 4 cm/h, 5 cm/h, 5.2 cm/h, 5.3cm/h and 5.4 cm/h at DEM spatial resolution of 85 m. The parameters are kept the same as the previous runs apart from an arbitrary inflow of 1500 m^3/s has been applied to the model.

Figure 3.3.5 shows flow travel time increase of 8.25 h, 13.25 h,17.25 h, 20.75 h, 24.75 h, 28.75 h ,33 h, 37.75 h ,42.5 h and 47.75 h along with increasing the infiltration rate from no infiltration to 2.8 cm/h, 3 cm/h, 3.1 cm/h, 3.5 cm/h, 3.9 cm/h, 4 cm/h, 5 cm/h, 5.2 cm/h, 5.3 cm/h reaching the infiltration rate of 5.4 cm/h and applying the Manning's friction coefficient ranging from 0.01 to 0.1 when the full simulation domain becomes wet. This increase in the flow travel time because of increasing the volume amount of water infiltrated from the water volume added to the model during the simulation along with increasing the infiltration rate. Therefore, longer time required for the flow travel time to reach the end of the domain simulation.

Figure 3.3.5 shows a similar increase in the flow travel time of 38 h, 46.5 h,47.5 h, 48 h, 50.25 h, 53.25 h, 53.75 h, 66.25 h , 71.5 h, 73.75 and 77.5 h when increasing the Manning's friction coefficient for a range from 0.01 to 1 and applying a constant infiltration rate values of 0 cm/h, 2.8 cm/h, 3 cm/h, 3.1 cm/h, 3.5 cm/h, 3.9 cm/h, 4 cm/h, 5 cm/h, 5.2 cm/h, 5.3 cm/h and 5.4 cm/h when the full simulation domains becomes wet.

For a similar reason to that described earlier, this increase in the flow travel time along with increasing the Manning's friction coefficient and applying a constant infiltration rate values as explained earlier because of the flow travel time is linked to the flow resistance which causes reducing in the flow velocity. Therefore, higher surface roughness causes a longer flow travel time.

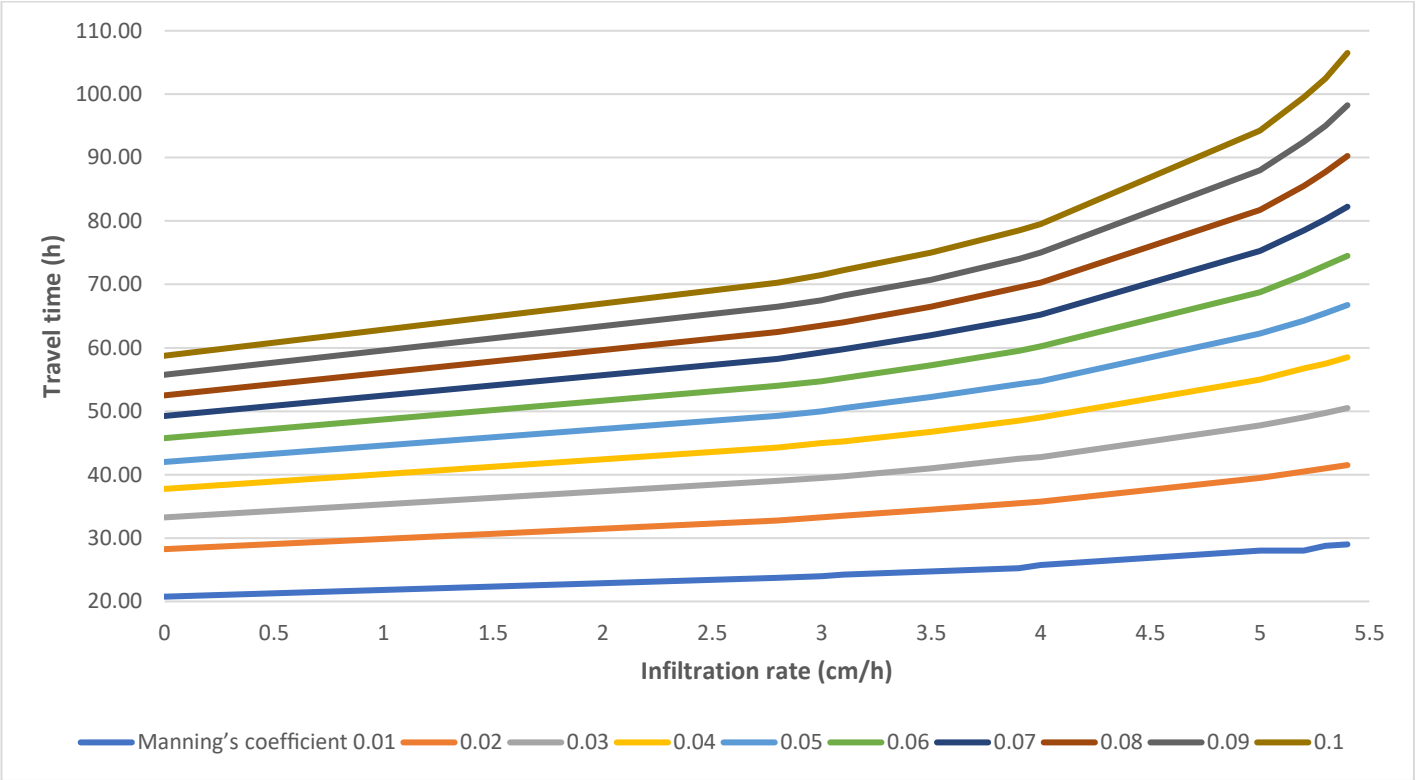

Figure 3.3.5 The evolution of flow travel time versus of various constant infiltration rate values and Manning's friction coefficient ranging from 0.01 to 0.1 at DEM spatial resolution of 85 m.

Furthermore, Figure 3.3.6 shows a decrease in the flooded area of 7.8 km^2, 8.34 km^2, 9.75 km^2, 11.26 km^2, 12.3 km^2, 13.42 km^2 , 14.88 km^2 , 15.52 km^2 ,16.94 km^2 and 17.86 km^2 along with increasing the infiltration rate from no infiltration reaching the infiltration rate of 5.4 cm/h and applying the Manning's friction coefficient ranging from 0.01 to 0.1 when the full simulation domain becomes wet.

This decrease in the flooded area because of increasing the volume amount of water infiltrated from the water volume added to the model during the simulation along with increasing the infiltration rate.

On another hand, Figure 3.3.6 shows an increase in the flooded area of 35.02 km^2, 30.65 km^2, 30.85 km^2, 30.69 km^2 ,29.59 km^2 ,28.95 km^2 ,29.17 km^2 , 25.92 km^2 ,25.56 km^2 , 25.28 km^2 and 24.97 km^2 when increasing the channel Manning's friction coefficient for a range from 0.01 to 1 and applying a constant infiltration rate values of 0 cm/h, 2.8 cm/h, 3 cm/h, 3.1 cm/h, 3.5 cm/h, 3.9 cm/h, 4 cm/h, 5 cm/h, 5.2 cm/h, 5.3 cm/h and 5.4 cm/h when the full simulation domains becomes wet.

This increase in the flooded area along with increasing the channel Manning's friction coefficient and applying a constant infiltration rate values as explained previously. Therefore, higher surface roughness causes a decrease in the flow velocity, increase in the water level which leads to greater flooded area.

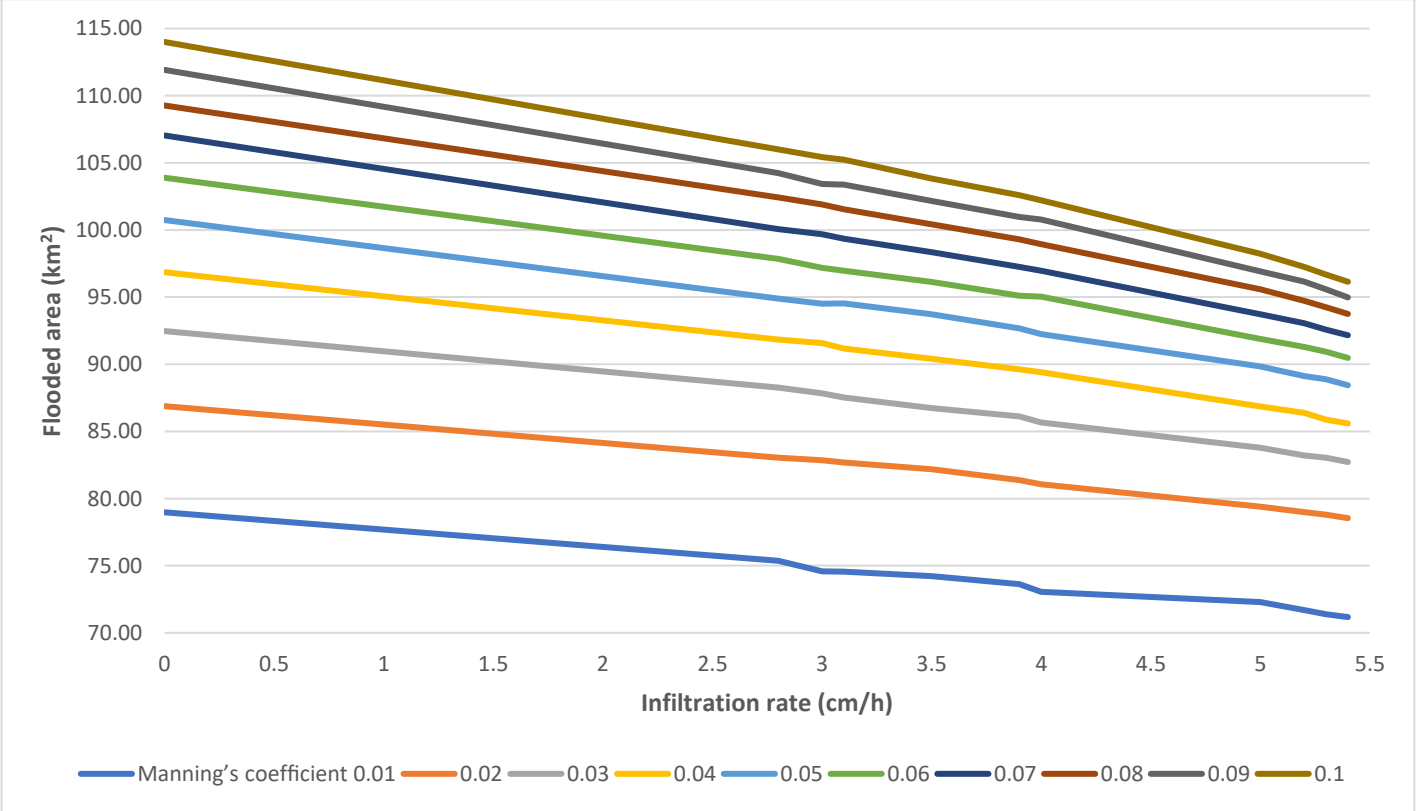

Figure 3.3.6 The evolution of flooded area versus of various constant infiltration rate values and channel Manning's friction coefficient ranging from 0.01 to 0.1 at DEM spatial resolution of 85 m.

Lastly, the sensitivity analysis results show both parameters, the constant infiltration rate and the channel Manning's friction coefficient have a significant impact on the flow travel time and the flooded area on Wadi Al Batin. Therefore, increasing the Manning's friction coefficient leads to longer flow travel time as well as greater flooded area. On the other hand, increasing the constant infiltration rate leads to decreasing the flooded area and longer flow travel time as explained earlier in this Chapter.

Therefore, this significant impact of the infiltration on the flow wave propagation characteristics, leads to consider a careful estimation of the infiltration in the ephemeral river system. Meaning that better estimation of the infiltration will lead to more reliable estimation of the flood risk in the ephemeral river system.

3.3.4 Effect of variable magnitude and duration inflow hydrographs

A flow hydrograph with varying flow magnitude has used as a model inflow as a part of the model sensitivity analysis to varying flow hydrograph magnitude. The model simulations were re-run with varying flow magnitude with a peak flow of 1500 m^3/s, 1200 m^3/s and 1200 m^3/s as shown in the Figure 3.3.7, in order to evaluate the impact of constant infiltration on the flood propagation characteristics such as the flow travel time and the flooded area.

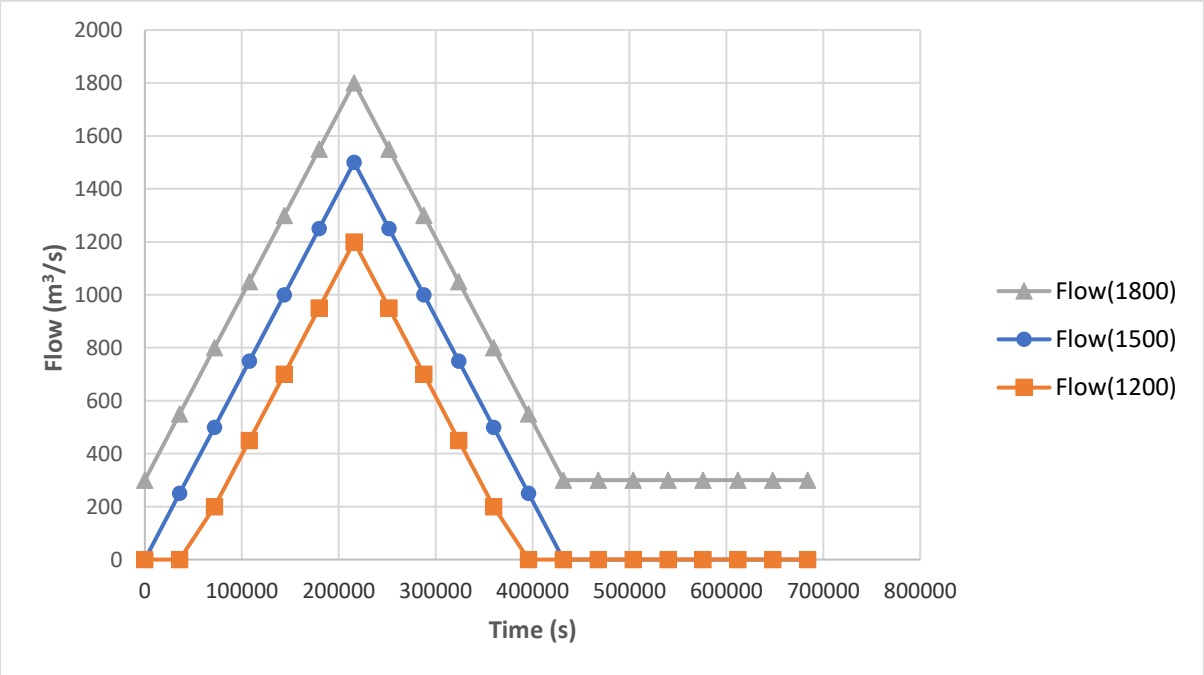

Figure 3.3.7 Flow hydrograph used as a model inflow.

Table 3.3.4, Table 3.3.5, Figure 3.3.8 and Figure 3.3.9 show similar patterns in terms of flow travel time and the flooded area, when varying flow magnitude hydrograph of 1500 m^3/s has been applied. This is in comparing against the previous runs when applying a constant inflow magnitude of 1500 m^3/s into the model.

Table 3.3.4 and Figure 3.3.8 show an increase in flow travel time along with increasing the constant infiltration rate as well as increasing the floodplain Manning's friction coefficient. This pattern in the flow travel time results was explained in detail earlier in this Chapter. Therefore, this gives more reliability to the discussion of the simulated travel time results.

Moreover, Table 3.3.5 and Figure 3.3.9 show a decrease in the flooded area along with increasing the infiltration rate. However, Table 3.3.5 and Figure 3.3.9 show an increase in the flooded area along with increasing the floodplain Manning's friction coefficient. Again, the flooded area results patterns are similar results shown and explained earlier in this Chapter when constant inflow has been applied to the model. Therefore, this might give an approximate credibility to the discussion of the simulated flooded area results.

Table 3.3.4 The evolution of flow travel time versus of various constant infiltration rate values and Manning's friction coefficient ranging from 0.01 to 0.1 at DEM spatial resolution of 85 m when applying varying inflow magnitude hydrograph.

Travel time (h)							
Manning's coefficient	**No Infiltration**	**Infiltration rate 2.8 (cm/h)**	**Infiltration rate 3 (cm/h)**	**Infiltration rate 3.1 (cm/h)**	**Infiltration rate 3.5 (cm/h)**	**Infiltration rate 3.9 (cm/h)**	**Infiltration rate 4 (cm/h)**
0.01	48.25	56.25	57.00	57.25	58.75	60.50	60.75
0.02	56.00	65.00	65.75	66.25	68.00	69.75	70.25
0.03	61.75	71.50	72.50	72.75	74.75	76.75	77.25
0.04	66.75	77.00	78.00	78.50	80.50	82.75	83.50
0.05	71.00	82.00	83.00	83.50	86.00	88.75	89.75
0.06	75.00	86.75	88.00	88.50	91.25	94.75	95.75
0.07	78.75	91.25	92.75	93.25	96.50	100.75	102.00
0.08	82.25	95.75	97.25	98.00	101.75	106.75	108.50
0.09	85.50	100.00	101.75	102.50	107.00	113.25	115.50
0.1	88.50	104.25	106.25	107.25	112.25	120.50	124.00

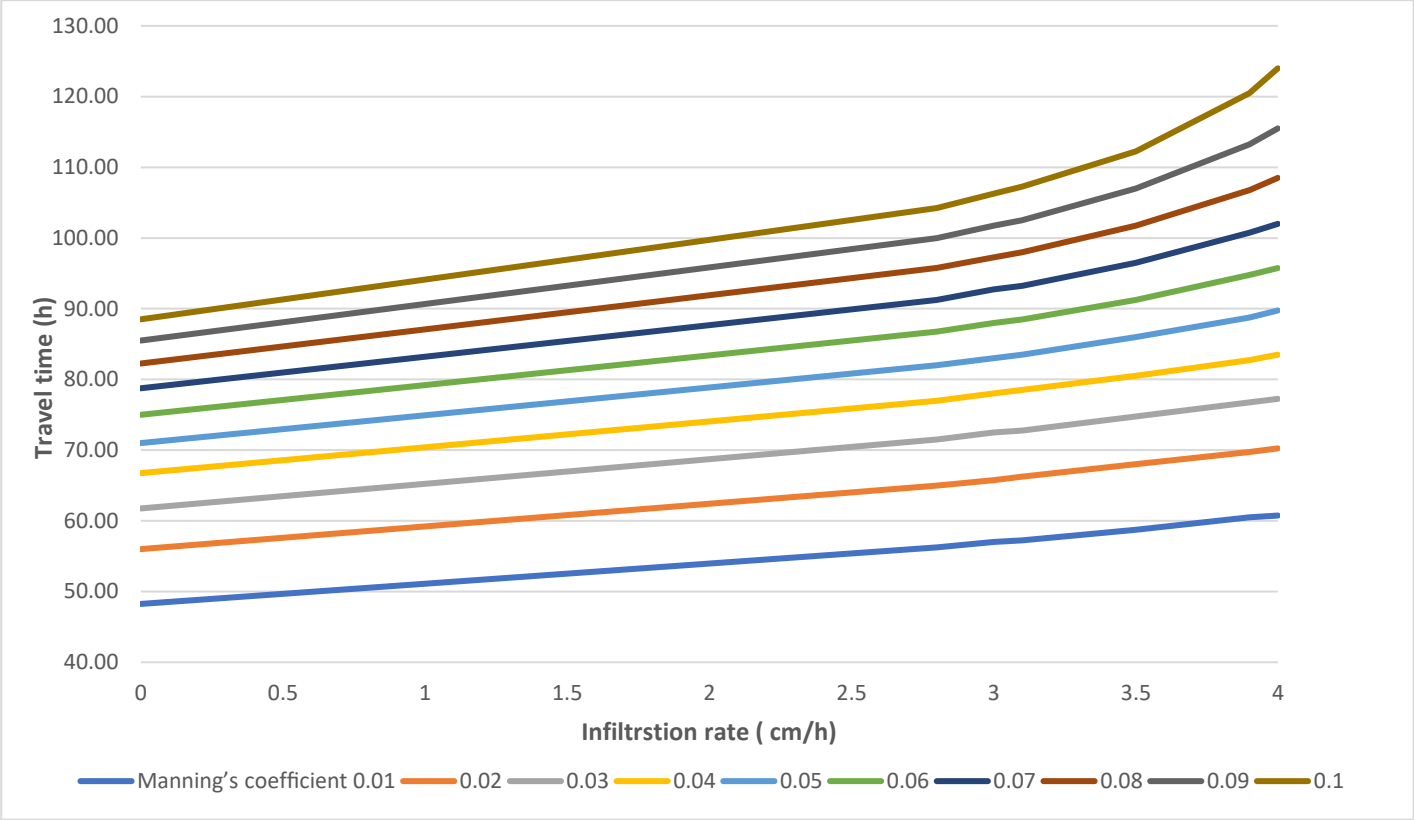

Figure 3.3.8 The evolution of flow travel time versus of various constant infiltration rate values and Manning's friction coefficient ranging from 0.01 to 0.1 at DEM spatial resolution of 85 m when applying varying inflow magnitude hydrograph.

Table 3.3.5 The evolution of flooded area versus of various constant infiltration rate values and Manning's friction coefficient at DEM spatial resolution of 85 m when applying varying inflow magnitude hydrograph.

Flooded area (km^2)							
Manning's coefficient	**No Infiltration**	**Infiltration rate 2.8 (cm/h)**	**Infiltration rate 3 (cm/h)**	**Infiltration rate 3.1 (cm/h)**	**Infiltration rate 3.5 (cm/h)**	**Infiltration rate 3.9 (cm/h)**	**Infiltration rate 4 (cm/h)**
0.02	84.17	82.09	81.70	81.70	81.25	80.38	80.16
0.04	95.69	89.59	88.96	88.68	87.32	85.41	85.02
0.06	102.09	93.15	92.46	91.73	89.35	87.62	86.91
0.08	107.24	94.88	93.48	92.74	91.20	89.23	88.40

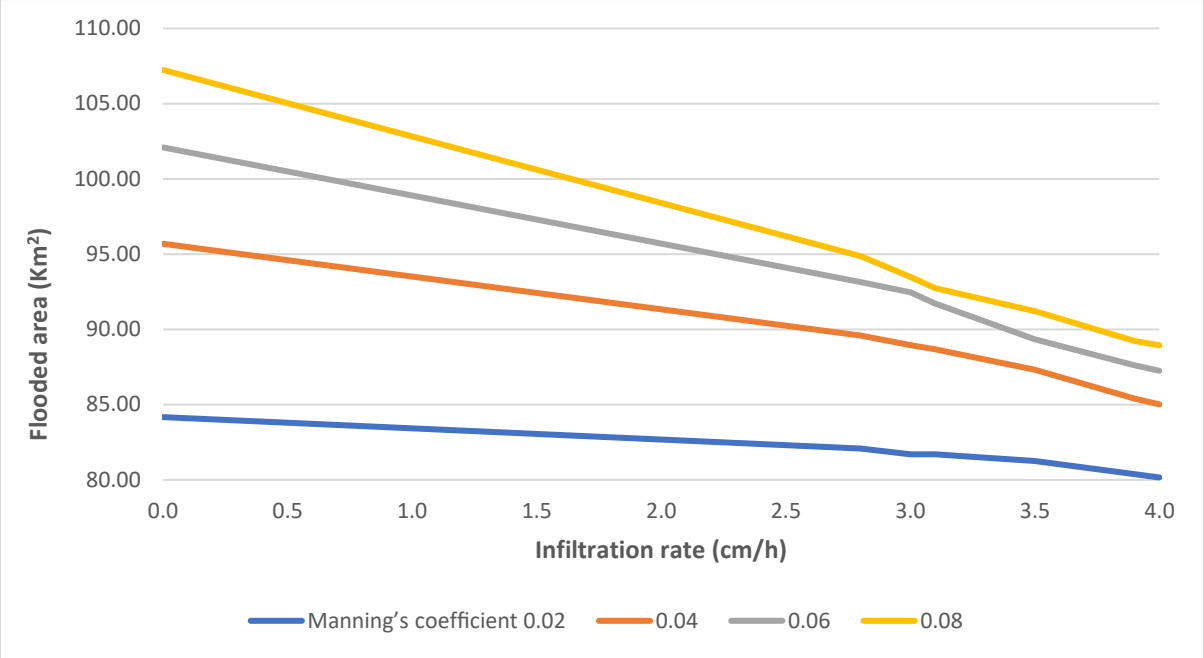

Figure 3.3.9 The evolution of flooded area versus of various constant infiltration rate values and Manning's friction at DEM spatial resolution of 85 m when applying varying inflow magnitude hydrograph.

Figure 3.3.10 shows the comparison between two scenarios where applied a constant flow to the model (SE1) and where varying flow magnitude scenario has applied (SE2) at floodplain Manning's friction coefficient of 0.06 and DEM spatial resolution of 85 m. The Figure 3.3.10 below shows a longer flow travel time of 29.25 h, 32.75 h, 33.25 h, 33.25 h, 34 h, 35.25 h and 35.5 h at the constant infiltration rate applied to the model of 0 cm/h, 2.8 cm/h, 3 cm/h, 3.1 cm/h, 3.5 cm/h, 3.9 cm/h and 4 cm/h when applied varying flow magnitude scenario in comparing with shorter flow travel time when applied a constant inflow magnitude.

This increases the flow travel time because of a decreased volume of water added to the model during this varying flow magnitude hydrograph compared to the constant inflow. The water volume added to the model shown in Table 3.3.6 The comparison of model added water volume versus constant infiltration rate values at Manning's friction of 0.06 and DEM spatial resolution of 85 m when applying two flow scenarios, SE1 constant flow scenario and SE2 varying flow magnitude scenario..

Furthermore, Figure 3.3.11 shows a decrease in the flooded area when applied varying flow magnitude scenario in comparing with greater flooded area when applied a constant inflow magnitude. This might be explained because of the decreasing the water volume added to the model when applying variable flow magnitude as shown in Table 3.3.6 The comparison of model added water volume versus constant infiltration rate values at Manning's friction of 0.06 and DEM spatial resolution of 85 m when applying two flow scenarios, SE1 constant flow scenario and SE2 varying flow magnitude

scenario.. Thus, it leads to lower water level therefore less flooded area extent within the simulation domain.

Table 3.3.6 The comparison of model added water volume versus constant infiltration rate values at Manning's friction of 0.06 and DEM spatial resolution of 85 m when applying two flow scenarios, SE1 constant flow scenario and SE2 varying flow magnitude scenario. show the volume amount of water added to the model is higher when applying the SE1 in comparing to the SE2. This water volume increase pattern at the SE1 is similar at various infiltration rate values, Moreover, Table 3.3.6 The comparison of model added water volume versus constant infiltration rate values at Manning's friction of 0.06 and DEM spatial resolution of 85 m when applying two flow scenarios, SE1 constant flow scenario and SE2 varying flow magnitude scenario. shows a 7.2% decrease in water volume added to the model by increasing the infiltration rate from 2.h cm/h to 4 cm/h when SE1 has applied. On another hand Table 3.3.6 The comparison of model added water volume versus constant infiltration rate values at Manning's friction of 0.06 and DEM spatial resolution of 85 m when applying two flow scenarios, SE1 constant flow scenario and SE2 varying flow magnitude scenario. shows 52% decrease in the water volume added to the model when SE2 has applied.

This water volume decreases pattern in both scenarios might be explained by the amount of water volume infiltrated in both scenarios, thus higher water volume infiltrated leads to less amount of water volume in the model. Furthermore, Table 3.3.6 The comparison of model added water volume versus constant infiltration rate values at Manning's friction of 0.06 and DEM spatial resolution of 85 m when applying two flow scenarios, SE1 constant flow scenario and SE2 varying flow magnitude scenario. shows significant decrease of 52% in the water volume added to the model at the SE2 in comparing to the 7.2% at the SE1. This might be explained because of applying triangular magnitude inflow hydrograph. It means much less water volume applied to the model, which leads to much less water volume left in the model by applying the same infiltration rate.

Table 3.3.6 The comparison of model added water volume versus constant infiltration rate values at Manning's friction of 0.06 and DEM spatial resolution of 85 m when applying two flow scenarios, SE1 constant flow scenario and SE2 varying flow magnitude scenario.

Water volume (km^3)						
Inflow Hydrograph scenario	**Infiltration rate 2.8 (cm/h)**	**Infiltration rate 3 (cm/h)**	**Infiltration rate 3.1 (cm/h)**	**Infiltration rate 3.5 (cm/h)**	**Infiltration rate 3.9 (cm/h)**	**Infiltration rate 4 (cm/h)**
SE1	0.217	0.215	0.214	0.208	0.203	0.202
SE2	0.017	0.015	0.014	0.011	0.009	0.008

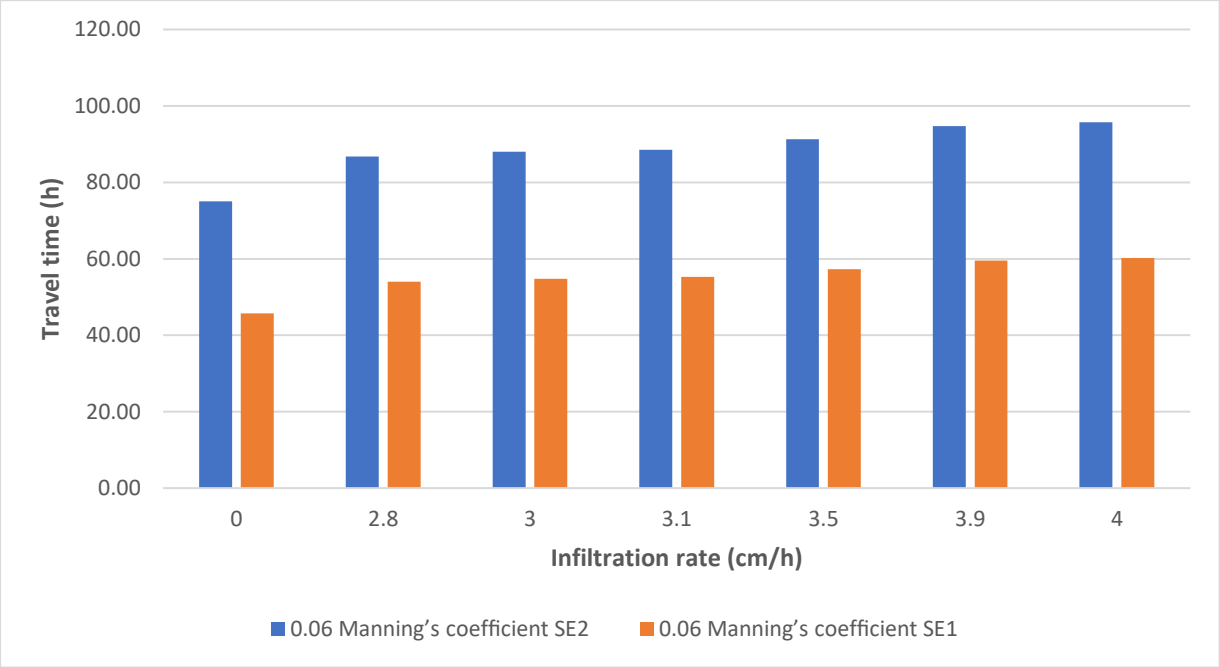

Figure 3.3.10 The comparison of flow travel time versus various constant infiltration rate values at Manning's friction of 0.06 and DEM spatial resolution of 85 m when applying two flow scenarios, SE1 constant flow scenario and SE2 varying flow magnitude scenario.

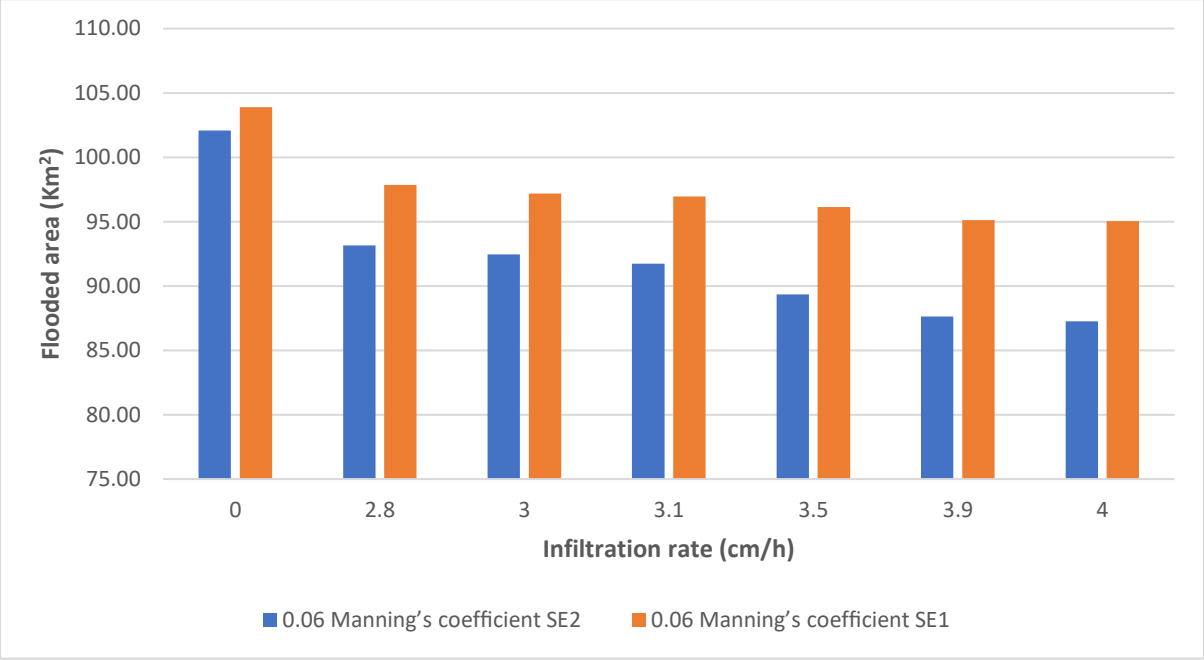

Figure 3.3.11 The comparison of flooded area versus various constant infiltration rate values at Manning's friction of 0.06 and DEM spatial resolution of 85 m when applying two flow scenarios, SE1 constant flow scenario and SE2 varying flow magnitude scenario.

As part of the sensitivity analysis, a further set of model runs has been carried out by applying three varying inflow magnitude hydrographs of 1800 m^3/s, 1500 m^3/s and 1200 m^3/s at DEM spatial resolution of 85 m and Manning's friction of 0.06. Table 3.3.7 and Figure 3.3.12 The evolution of flow travel time versus of various constant infiltration rate values at DEM spatial resolution of 85 m when applying three varying inflow magnitude hydrographs. show the evolution of travel time when three varying inflow magnitude hydrographs of 1800 m^3/s, 1500 m^3/s and 1200 m^3/s have been applied as a model inflow.

The flow travel time results show an increase in the flow travel time with decreasing peak inflows. These increasing pattern in the flow travel time is shown as well when applying various infiltration rate scenarios of no infiltration, 2.8 cm/h, 3 cm/h, and 3.1 cm/h infiltration rate. As discussed earlier, this could be explained by the volume amount of water added to the model as shown in Table 3.3.8 . Higher water volume will lead to higher flow velocity. Therefore, less travel time is required for the flow to reach the domain outlet.

Table 3.3.7 The evolution of flow travel time versus of various constant infiltration rate values at DEM spatial resolution of 85 m when applying three varying inflow magnitude hydrographs.

Travel time (h)				
Peak Inflow (m^3/s)	**No Infiltration**	**Infiltration rate 2.8 (cm/h)**	**Infiltration rate 3 (cm/h)**	**Infiltration rate 3.1 (cm/h)**
1800	64.50	75.00	76.00	76.50
1500	75.00	86.75	88.00	88.50
1200	89.25	109.75	114.50	118.25

Table 3.3.8 shows again what discussed earlier regarding the decrease in water volume added to the model with increasing the infiltration rate. On another hand, it shows an increase in the water volume added to the model by increasing the magnitude of the peak inflow hydrograph. The reason behind the water volume results pattern is explained earlier in this section.

Table 3.3.8 The evolution of water volume added to the model versus of various constant infiltration rate values at DEM spatial resolution of 85 m when applying three varying inflow magnitude hydrographs.

Water volume (km^3)				
Peak Inflow (m^3/s)	**No Infiltration**	**Infiltration rate 2.8 (cm/h)**	**Infiltration rate 3 (cm/h)**	**Infiltration rate 3.1 (cm/h)**
1800	0.129	0.066	0.062	0.060
1500	0.067	0.017	0.015	0.014
1200	0.064	0.013	0.012	0.011

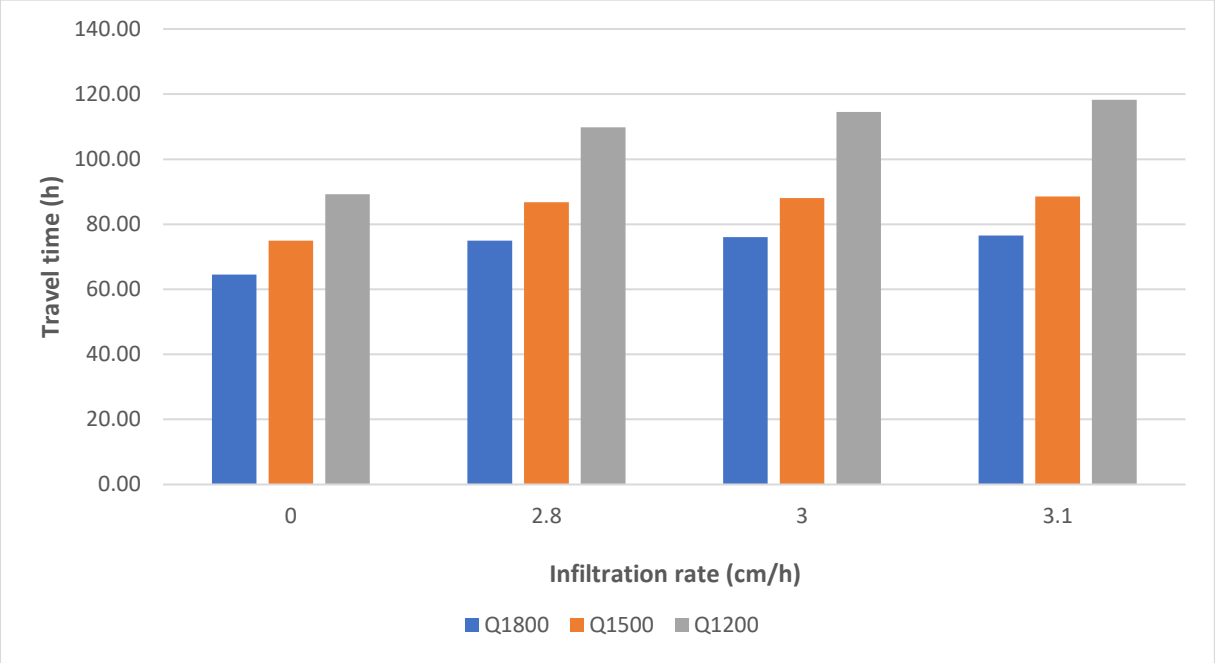

Figure 3.3.12 The evolution of flow travel time versus of various constant infiltration rate values at DEM spatial resolution of 85 m when applying three varying inflow magnitude hydrographs.

Moreover, Table 3.3.9 and Figure 3.3.13 The evolution of flooded area versus of various constant infiltration rate values at DEM spatial resolution of 85 m when applying three varying inflow magnitude hydrographs. show the evolution of flooded area when three varying inflow magnitude hydrographs of 1800 m^3/s, 1500 m^3/s and 1200 m^3/s have been applied as a model inflow.

The flooded area results show a greater flooded area with increasing the model peak inflows. These increase pattern in the flooded area has shown as well when applying various infiltration rate scenarios of no infiltration, 2.8 cm/h, 3 cm/h, and 3.1 cm/h infiltration rate. Again, as discussed earlier, this could be explained by the volume amount of water added to the model as shown in Table 3.3.8.

Therefore, similarly, greater magnitude peak inflow leads to greater flood extent within the model simulation.

Again, this consistency in the simulated flooded area and simulated travel time results pattern when applying various flow magnitude hydrographs, gives approximate confidence in terms of the validity of the simulated results discussion.

Table 3.3.9 The evolution of flooded area versus of various constant infiltration rate values at DEM spatial resolution of 85 m when applying three varying inflow magnitude hydrographs.

Flooded area (km^2)				
Peak Inflow (m^3/s)	**No Infiltration**	**Infiltration rate 2.8 (cm/h)**	**Infiltration rate 3 (cm/h)**	**Infiltration rate 3.1 (cm/h)**
1800	104.91	99.74	99.25	99.04
1500	102.09	93.15	92.46	91.73
1200	95.55	73.48	67.83	63.31

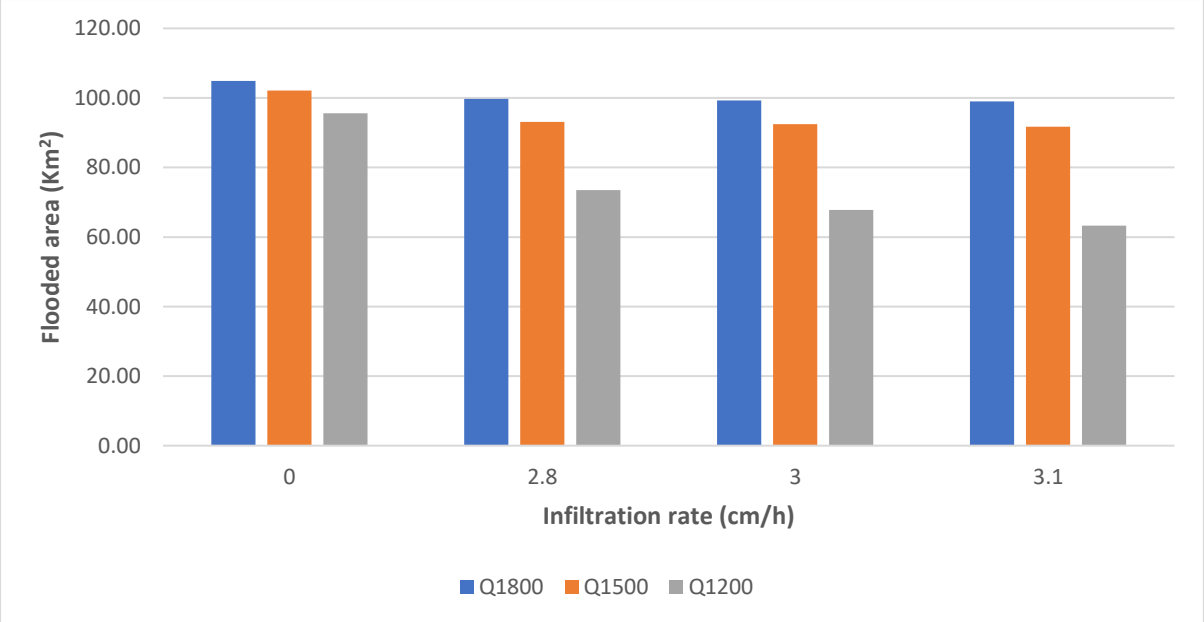

Figure 3.3.13 The evolution of flooded area versus of various constant infiltration rate values at DEM spatial resolution of 85 m when applying three varying inflow magnitude hydrographs.

Another set of model runs has been conducted by doubling the duration of the existing varying inflow magnitude hydrograph (peak inflow of 1500 m^3/s) with spatial resolution of 85 m. Various infiltration rate applied to the model of 0 cm/h, 2.8 cm/h, 3 cm/h, 3.1 cm/h, 3.5 cm/h, 3.9 cm/h and 4 cm/h.

Table 3.3.10 and Figure 3.3.14 show similar travel time results pattern to the travel time model results as shown earlier in this chapter in Figure 3.3.8. Moreover, Table 3.3.11 The evolution of flooded area versus of various constant infiltration rate values at DEM spatial resolution of 85 m when applying the doubled duration varying inflow magnitude hydrograph. Figure 3.3.15 show similar flooded area patterns as shown in Figure 3.3.9.

These sensitivity analysis results show that the simulated travel time and the flooded area pattern are as expected from a physical interpretation. Generally, the simulated travel time shows an increase with increasing the infiltration rate as well as increasing the Manning's coefficient. This is mainly related to the amount of water volume infiltrated within the simulation domain. Also, it is related to the flow resistance within the simulation domain, which leads to longer flow travel time.

In terms of the simulated flooded area, the results pattern shows decrease in the flood extent along with increasing the infiltration rate. This is again related to the water volume infiltrated with in the simulation domain. However, the simulated flooded area results pattern shows an increase in the flooded area along with increasing the Manning's coefficient. This is mainly explained by the impact of the flow resistance which leads to higher water level and therefore, greater flood extent.

Table 3.3.10 The evolution of travel time versus of various constant infiltration rate values at DEM spatial resolution of 85 m when applying the doubled duration varying inflow magnitude hydrograph.

Travel time (h)							
Manning's coefficient	**No Infiltration**	**Infiltration rate 2.8 (cm/h)**	**Infiltration rate 3 (cm/h)**	**Infiltration rate 3.1 (cm/h)**	**Infiltration rate 3.5 (cm/h)**	**Infiltration rate 3.9 (cm/h)**	**Infiltration rate 4 (cm/h)**
0.02	73.25	91.75	93.50	94.50	98.25	102.50	103.50
0.04	86.00	107.25	109.25	110.25	114.50	119.25	120.50
0.06	95.75	118.75	121.00	122.00	126.75	131.75	133.25
0.08	104.25	128.50	131.00	132.00	137.00	142.50	144.00

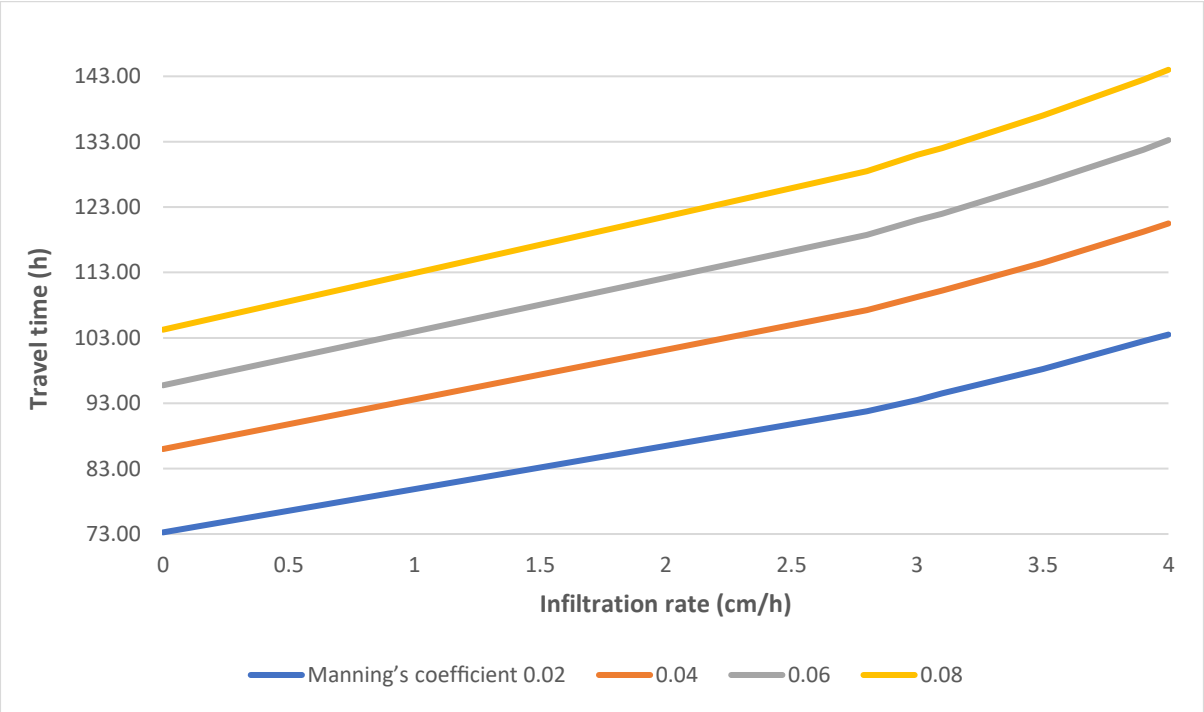

Figure 3.3.14 The evolution of travel time versus of various constant infiltration rate values at DEM spatial resolution of 85 m when applying the doubled duration varying inflow magnitude hydrograph.

Table 3.3.11 The evolution of flooded area versus of various constant infiltration rate values at DEM spatial resolution of 85 m when applying the doubled duration varying inflow magnitude hydrograph.

Flooded area (km^2)							
Manning's coefficient	**No Infiltration**	**Infiltration rate 2.8 (cm/h)**	**Infiltration rate 3 (cm/h)**	**Infiltration rate 3.1 (cm/h)**	**Infiltration rate 3.5 (cm/h)**	**Infiltration rate 3.9 (cm/h)**	**Infiltration rate 4 (cm/h)**
0.02	79.10	76.86	76.76	76.71	76.69	76.67	76.66
0.04	89.38	87.38	87.21	87.13	86.82	86.81	86.79
0.06	96.85	94.56	94.54	94.29	93.92	93.32	93.31
0.08	102.96	99.97	99.83	99.42	98.32	97.05	96.70

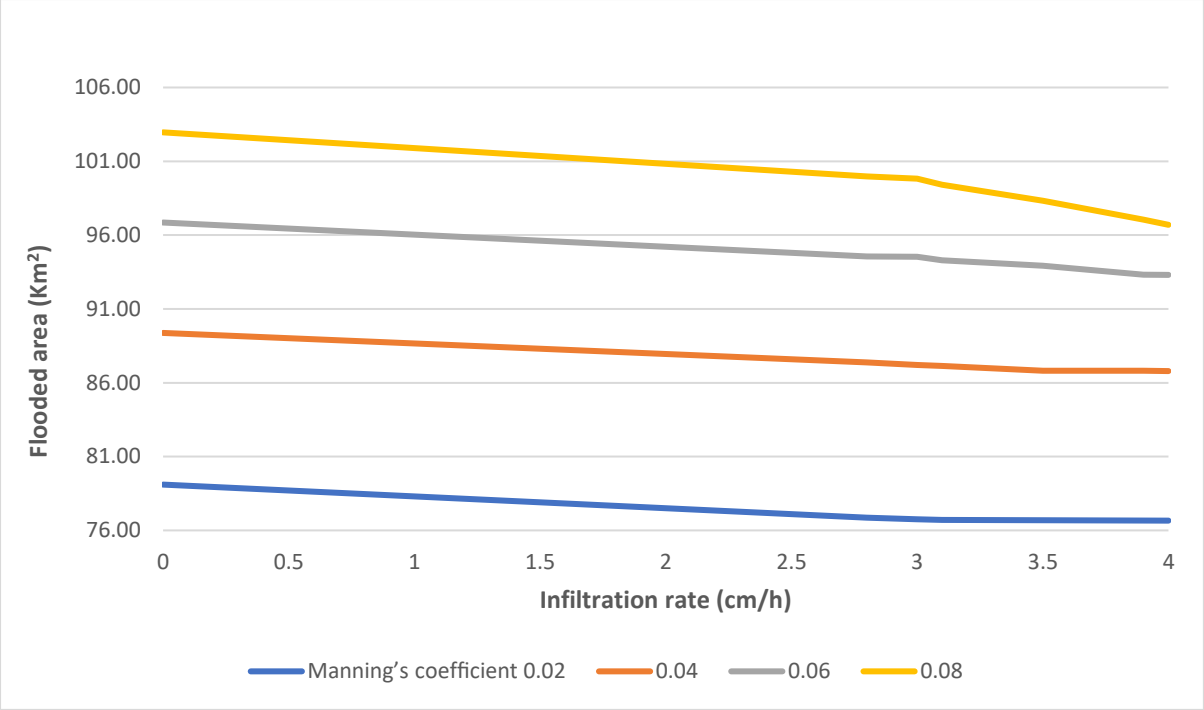

Figure 3.3.15 The evolution of flooded area versus of various constant infiltration rate values at DEM spatial resolution of 85 m when applying the doubled duration varying inflow magnitude hydrograph.

In summary, the implications of various parameters on the flow wave propagation in the ephemeral river system have been discussed. These parameters are DEM, Manning's coefficient, constant infiltration rate, and various magnitude inflow hydrographs.

The sensitivity analysis results show high importance of the constant infiltration parameters. As the implications of the parameters tested with in the sensitivity analysis are greater when they are associated with increasing the infiltration rate.

Figure 3.3.5 shows with increasing the Manning's coefficients from 0.04 to 0.06 a greater Manning's coefficient implications on the travel time by 21.2%, 22.1% and 27.4% when applying no infiltration, 3.1 cm/h and 5.4 cm/h infiltration rate respectively. This discussion is applicable as well when applying variable inflow magnitude hydrograph and duration instead of constant inflow as shown in Figure 3.3.8 and Figure 3.3.14.

Figure 3.3.12 The evolution of flow travel time versus of various constant infiltration rate values at DEM spatial resolution of 85 m when applying three varying inflow magnitude hydrographs. shows at various magnitude inflow hydrograph of 1200 m/s and 1800 m/s a greater implication on the travel time by 27.7%, 31.7%, 33.6% and 35.3% when applying no infiltration, 2.8 cm/h, 3 cm/h and 3.1 cm/h infiltration rate respectively.

Moreover, the sensitivity analysis shows significant implications of DEM spatial resolution as well. This implication becoming greater with increasing the DEM resolution. Figure 3.3.1 shows an implication of 12% to the simulated flooded are when applying the DEM resolution of 85 m and 515 m.

Therefore, based on the significant implications of the infiltration and the DEM, finer DEM spatial resolution and spatial Green-Ampt infiltration will be tested and discussed in Chapter 5.

Lastly, the sensitivity analysis shows a consistency in the simulated results pattern when applying various range of same parameters such as DEM, Manning's coefficient, constant infiltration rate and variable magnitude inflow hydrograph. Therefore, this gives an approximate confidence in the simulated results and the discussion of the implications of the parameters mentioned above.

3.4 Conclusion

It is concluded from the Chapter 3, that there is a significant impact of the infiltration loss in Wadi Al Batin on the wave propagation characteristics such as the travel time, the flooded area, and the water volume. This implication leads to the conclusion that more accurate estimation of the infiltration loss is needed by incorporating spatial variable infiltration over all the simulation domain rather than applying a constant infiltration across the domain.

Furthermore, this would be expected to lead to a more accurate flash flood risk assessment prediction, warning flood system and developed emergency plan response from the local authorities. This will be investigated and studied further in Chapter 5.

Moreover, it is concluded that various DEM spatial resolutions and the Manning's coefficient has crucial and significant impact which in turn shows that it also has an effect on simulating the wave propagation characteristics through its effect on infiltration.

In addition to the above conclusions, a further the limitation of the simulations of Wadi Al Batin is that no formal calibration nor verification was conducted due to the data scarcity in the Wadi Al Batin.

However, a set of sensitivity analysis has been conducted such as various DEM spatial resolution, range of Manning's coefficient, range of constant infiltration rate and various inflow magnitude hydrographs and duration.

This consistency and the similarity in the simulated results' patterns when sensitivity analysis has conducted, gives an approximate credibility and more strength to the validity of the above conclusions.

Lastly, based on the above conclusions, the next chapter will discuss implementation of a spatially distributed, variable infiltration Green-Ampt model into LISFLOOD-FP and testing the updated model on various scenarios.

Chapter4 Development of a Green-Ampt variable infiltration model within the Hydrodynamic model.

4.1 Introduction

The effects of the constant infiltration rate on the propagation of a flood wave in the Wadi Al Batin ephemeral river system were explored in Chapter 3. The implications of a constant infiltration rate were shown that compared to a no infiltration scenario, the infiltration scenario has significant and important impacts on the flood wave propagation, such as 41.75 hours difference in the flow travel time, 4.278 km^2 difference in the flooded area, and 0.0112 km^3 in water volume.

Effective hydrological modelling and better estimation of the infiltration rate is an important component of the water cycle and plays a crucial part of the flood risk assessment, potential flood risk and flood prediction. Therefore, this generally leads to more flood resilient measures. One approach to estimation of infiltration that has gained much traction is that originally described by Green and Ampt (1911). A number of Green-Ampt infiltration-based models have been developed since, and these are classified into three categories as: empirical, semi empirical and physical models, Mishra et al. (2003).

The original Green-Ampt model, Green and Ampt (1911), is used for estimating variable infiltration. It simulates the process of one-dimensional vertical infiltration into soil based on the soil characteristics, such as the hydraulic conductivity, soil suction head and the soil moisture content, in order to estimate the infiltration rate. The Green-Ampt parameters have been successfully correlated with the soil texture classification Rawls et al. (1983) which means the soil texture type can be used to define the Green-Ampt model parameters.

The aim of this chapter is to implement spatially variable distributed Green-Ampt infiltration into the LISFLOOD-FP model, in order to better understand the implications of the spatial variable channel bed infiltration process on the wave progression and characteristics in ephemeral systems. Once implemented, it will be necessary to assess and evaluate the effectiveness of the updated version of LISFLOOD-FP which will be referred to as LISFLOOD-FP-vGA. The assessment is carried out by estimating the spatially distributed accumulated infiltration on various testing models and scenarios of increasing complexity. These tests include: ponding infiltration testing with a non-flowing one-metre cell, a more sophisticated flowing test of a simple conceptual river channel represented by a line of 1 m cell size of 10 cells, and the testing of a subset of a 2D river channel with spatially varied

soil types from the Wadi Al Batin in Saudi Arabia, which is within this research study area, and finally estimating the spatially distributed accumulated infiltration by testing model of spatially distributed pounding accumulated infiltration test with non-flowing of 10×10 cells. Starting with simplified built modelling to test an individual element which is testing Green-Ampt ponding infiltration in a single cell, then more sophisticated infiltration testing from flowing water of a simple conceptual river channel. Furthermore, testing the spatially varied infiltration of 2D river channel with spatially varied soil texture types.

The reason for starting the testing with the simplified model, was because of testing an individual element makes the test more comparable with simple presentation of the explicit solution of Green-Ampt model as will be described in section 4.2.2

4.1.1 Research steps

The following methodology was conducted to achieve the aim of this chapter:

1. A literature review and comparison of numerical solutions of the Green-Ampt equation.
2. Selection of an explicit solution of the Green-Ampt model for implementation based on solution accuracy and ease of implementation within the LISFLOOD_FP code structure.
3. Implementation of the chosen explicit solution of spatially distributed Green-Ampt model of Parlange et al. (2002) into LISFLOOD-FP-vGA.
4. The updated version of LISFLOOD-FP-vGA was evaluated through 4 tests of increasing complexity.
    - Level 1 testing of the LISFLOOD-FP-vGA model which is ponding infiltration testing with non-flowing on a small scale of 1 m cell size and with a digital elevation model of 20 m a ponding water depth of 0.09 m. Level 1 testing is mainly for testing the variable Green-Ampt ponding infiltration with non-flowing water.
    - Level 2 testing of the LISFLOOD-FP-vGA model on more sophisticated model which is a river channel conceptual simplified and represented by line of 1m cell size of 10 cells of 10 with digital elevation model varies from 1m to 0.991m, a small gradient of 0.001 and a constant inflow of 0.01m^3/s. Level 2 testing is for testing the variable Green-Ampt infiltration on flowing water.
    - Level 3 testing of LISFLOOD-FP-vGA model by assessing the spatially distributed Green-Ampt accumulated infiltration on ponding infiltration testing with non-flowing of 10×10 cells of 200 m cell size and setting an initial model depth of 0.4 m at the start of the simulation run.

- Level 4 testing of LISFLOOD-FP-vGA on a more complex model representing a real geometry small subset of 2D river channel from Wadi Al Batin in Saudi Arabia. Level 4 testing is for testing the variable Green-Ampt infiltration on flowing water in a real context.

4.2 Methodology

4.2.1 Green-Ampt Implementation

The Green-Ampt model, Green and Ampt (1911), is common method to estimate the infiltration loss within the rainfall runoff modelling process. The Green-Ampt equation is function of the hydraulic conductivity, soil suction head, porosity and time. It assumes a water movement is piston type with homogenous isotropic soil with two water contents, the initial water content and the saturated water content. The model assumes a soil profile that is separated by a sharp wetting front into upper saturated zone and lower unsaturated zone.

The infiltration rate under continuous ponding conditions is defined by Bouwer (1978) as the following:

$$f(t) = K_s \left[1 + \frac{H+\psi_f}{L_f(t)}\right] \quad (1)$$

Where $f(t)$ is the infiltration rate per unit area at a certain time [LT^{-1}], K_s is the hydraulic conductivity [LT^{-1}], H is the pounding depth [L], ψ_f is the suction head at the wetting front [L] and $L_f(t)$ is the wetting front progression at time t [L].

Substituting $L_f(t)$ by $\frac{F(t)}{\eta}$ and integrate it to equation (1) will lead to the equation (2):

$$f(t) = K_s \left[1 + \frac{\eta(H+\psi_f)}{F(t)}\right] \quad (2)$$

Where $F(t)$ is the accumulated infiltration at the time (t), η is the fillable porosity, which is equal to $\theta_s - \theta_i$, where θ_s is the saturated water content and the θ_i is the initial water content.

Substituting $f(t)$ by $\frac{dF(t)}{dt}$ this will lead to the implicit Green-Ampt equation by Kale and Sahoo (2011) as per the equation (3).

$$K_s t = F(t) - \eta\left(H + \psi_f\right) \ln\left[1 + \frac{F(t)}{\eta\left(H+\psi_f\right)}\right] \quad (3)$$

In order to implement Green-Ampt equation with in LISFLOOD-FP-vGA model's code, a literature review was conducted examining existing explicit approximate solution for this implicit Green-Ampt model. Ali et al. (2016) reviewed and compared nine explicit approximations of Green-Ampt model. The nine explicit models reviewed by Ali et al. (2016) are Li et al. (1976) (LI), Stone et al. (1994) (ST), Salvucci and Entekhabi (1994) (SE), Parlange et al. (2002) (PA), Barry et al. (2005) (BA), Swamee et al. (2012) (SW), Ali et al. (2013) (AL), Almedeij and Esen (2014) (AE), and Vatankhah (2015).
Ali et al. (2016) used six statistical indicators, various soil type classes and infiltration periods.
The study concluded that the BA was the most efficient model followed closely by the PA and the VA models.
Based on the results of Ali et al. (2016), a study was undertaken to determine the most appropriate for incorporating in the LISFLOOD-FP code. This concluded that based on the accuracy (confirming Ali et al.) and the programming structure of LISFLOOD-FP, the model referred to by Ali et al as the PA explicit model developed by Parlange et al. (2002) was most appropriate to be implemented in LISFLOOD-FP model's code.
Parlange et al. (2002) proposed expression is based on the Lambert W-function, an explicit solution for Green-Ampt model given by the following equation (4).

$$F(t)_{PA} = \frac{S^2}{2K_s}\left\{t^* \ln\left\{1 + t^* + \frac{\sqrt{2t^*}}{1+\sqrt{2t^*}/6}\right\}\right\} \quad (4)$$

Where t^* is the dimensionless infiltration time and it is defined by Ali et al. (2016) as the per the equation (5).

$$t^* = \frac{2K_s^2\, t}{S^2} \quad (5)$$

Where S is the sorptivity parameter $[LT^{-1/2}]$ which is defined by Parlange (1975) and Neuman (1976) as the following;

$$S^2 = 2\,\eta\, K_s\left(H + \psi_f\right) \quad (6)$$

The Parlange model was implemented within the LISFLOOD-FP-vGA Hydrodynamic model by modifying the existing LISFLOOD-FP code to integrate the explicit solution of Green-Ampt model set

by Parlange (1975). Table 4.2.1 shows an implementation of Green-Ampt within LISFLOOD-FP-vGA Hydrodynamic model code.

Table 4.2.1 The implemented Green Ampt infiltration code with in LISFLOOD-FP Hydrodynamic model.

```
INFILTRATION AND EVAPORATION
*******************************************************************************/

#include "lisflood.h"
#include "utility.h"
//------------------------------------------------------------------------------
void FPInfiltration(Pars *Parptr, Solver *Solverptr, Arrays *Arrptr)
{
  …
  …
  // Calculate Infiltration
  for(j=0;j<Parptr->ysz;j++){
    for(i=0;i<Parptr->xsz;i++){
      if(Arrptr->ChanMask[i+j*Parptr->xsz]==-1) { //only on non-channel cells
        h0=Arrptr->H[i+j*Parptr->xsz];
        if(h0>Solverptr->DepthThresh){
          if(Solverptr->GreenAmpt == 1){
              // From the cell location get the corresponding soil type as the GreenAmpt_index
              GreenAmpt_index = Arrptr->GreenAmpt_spatial_infiltration_map[i+j*Parptr->xsz];

              // Look up the parameters required for the Green-Ampt
              //calculation for the soil type at this location
              GreenAmptParams = GetGreenAmptParams(GreenAmpt_index,Parptr,Solverptr, verbose);
              K_s = GreenAmptParams[0];
              theta_s = GreenAmptParams[1];
              theta = GreenAmptParams[2];
              Wf = GreenAmptParams[3];

              // update the wetted time at this cell location
              Arrptr->GreenAmpt_accumulated_time_wet[i+j*Parptr->xsz] += Solverptr->Tstep;
              t_wet = Arrptr->GreenAmpt_accumulated_time_wet[i+j*Parptr->xsz];

              // Equation 6: Sorptivity squared
              S2 = 2*(theta_s-theta)*K_s*(Wf+h0);
              // Equation 5: dimensionless time
              t_star = 2*K_s*K_s*t_wet/S2;
              // Equation 4:
              F_t = 0.5*S2/K_s*(t_star + log(1+t_star+sqrt(2*t_star)/(1+sqrt(2*t_star)/6)));

              // Equation 2: the infiltration rate calculation
              f_t = K_s *(1+(theta_s-theta)*(Wf+h0)/F_t);

              // Infiltration calculation
              GA_infiltration = f_t * Solverptr->Tstep;

              //update the value of accumulated infiltration for this cell
              Arrptr->GreenAmpt_accumulative_infiltration[i+j*Parptr->xsz] += GA_infiltration;


              cell_inf = GA_infiltration;
          }else{
              cell_inf = Parptr->InfilRate * Solverptr->Tstep; //rate for depth, not area
          }
          h0-=cell_inf;
          //check for -ve depths
          if(h0<0) {
            cell_inf+=h0;
            h0=0;
          }
          // Save the depth for the cell
          Arrptr->H[i+j*Parptr->xsz]=h0;
          //Update the mass-balance
          Parptr->InfilTotalLoss+=cell_inf*Parptr->dA;
        }
      }
    }
  }
  return;
}
```

4.2.2 Test models descriptions

In this section, the testing models will be described for each testing level.

1 Level 1 testing

Level 1 testing consists of building two models. The first model built with in LISFLOOD-FP-vGA which is based on 1 m cell simulation with a model input of 20 m DEM spatial resolution, and a pounding water depth of 0.09 m and 10 hours of the simulation period.

The second model is the explicit solution of Green-Ampt coded by visual basic. As mentioned earlier in section 4.2.1., this model has built within a Microsoft Excel sheet and embedded with in visual basic. The two iterative methods used as a PA solver are the Newton–Raphson method after Rao et al (2006) and the secant iterative method.

The first model simulation was carried out by LISFLOOD-FP-vGA and the second model simulation via visual basic embedded within the Microsoft Excel sheet.

The test conducted using the Green-Ampt physical parameters for the *sandy loam* texture soil type from Rawls et al. (1982) as per the Table 4.2.2. Moreover, the model's simulation results of the accumulated infiltration as well as the infiltration rate compared to each other.

Table 4.2.2 Green-Ampt physical parameters of sandy loam texture soil type from Rawls et al. (1982).

Soil texture class	**Residual porosity**	**Effective porosity**	**Suction head (cm)**	**Hydraulic conductivity (cm/h)**
Sandy loam	0.041	0.412	11.01	1.09

2 Level 2 testing

Level 2 testing is based on creating a model of 10 cells row with cell size of 1m. The cell elevation varies from 1m to 0.991 m with a small gradient of 0.001 and a constant inflow of 0.01 m^3/s as shown in Figure 4.2.1

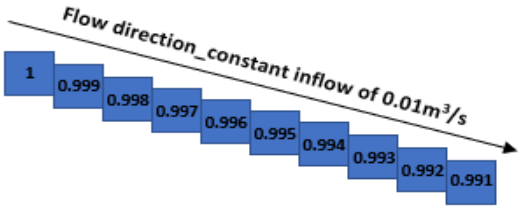

Figure 4.2.1 Schematic overview of the test 2 model set up.

Testing the LISFLOOD-FP-vGA model by running the simulations initially with three scenarios, initial simulation time step of 1 s and the simulation duration of 900 s as follows;

S1: running the simulation with no infiltration applied to the model.

S2: running the simulation with the steady constant infiltration of 0.00006 m/s applied to the model.

S3: running the simulation with variable infiltration, Green-Ampt infiltration applied to the model.

Evaluating the effectiveness of LISFLOOD-FP-vGA model within Level 2 testing started by comparing and analysing the characteristic of the simulated wave propagation of each three model scenarios S1, S2, S3 such as flood travel time. The accumulated infiltration, the water depth and the water surface elevation compared for different scenarios as well.

Further confirmation testing of LISFLOOD-FP-vGA with three more simulation scenarios were run with the same boundary conditions of S1, S2, S3 but with adding a pounding water depth of 0.09 m to LISFLOOD-FP-vGA simulations. The added three more scenarios are the following;

S1 A: the S1 model with no infiltration and a pounding water depth of 0.09 m.

S2 A: the S2 model with a steady constant infiltration rate of 0.00006 m/s and a pounding water depth of 0.09 m.

S3 A: the S3 model with a Green-Ampt variable infiltration and a pounding water depth of 0.09 m.

3 Level 3 testing

Level 3 testing of LISFLOOD-FP-vGA was undertaken by assessing the spatially distributed Green-Ampt accumulated infiltration on ponding infiltration testing with non-flowing of 10 x 10 cells of 200 m cell size and setting an initial model depth of 0.4 m at the start of the simulation run and two deferent soil types. One soil texture type of *sandy clay loam* at the centre cells of the simulation domain, where surrounded by another soil texture type of *clay loam* as shows in Figure 4.2.2 as soil reference 1 for *clay loam* and soil reference 2 for *sandy clay loam*. The Level 3 testing was undertaken with a simulation time of 691200 s and a time step of 3600 s.

1 1 1 1 1 1 1 1 1 1

1 1 1 1 1 1 1 1 1 1

1 1 1 1 1 1 1 1 1 1

1 1 2 2 2 2 2 2 1 1

1 1 2 2 2 2 2 2 1 1

1 1 2 2 2 2 2 2 1 1

1 1 2 2 2 2 2 2 1 1

1 1 1 1 1 1 1 1 1 1

1 1 1 1 1 1 1 1 1 1

1 1 1 1 1 1 1 1 1 1

Figure 4.2.2 Schematic soil texture type reference overview of the test 3 LISFLOOD-FP-vGA model set up.

4 Level 4 testing

Level 4 testing of LISFLOOD-FP-vGA model was representing a real geometry subset of the 2D river channel from the Wadi Al Batin in Saudi Arabia. This small subset of approximately 13 km (in river reach length) from the 2D river channel of Wadi Al Batin has chosen to build this testing model with an inflow of 100 m^3/s. This inflow has chosen as an arbitrary for testing purposes. The topography of this chosen area varies from 350.39 m to reach the maximum elevation of 416.51 m presented by the Digital Elevation Model (DEM) of 90 m spatial resolution as shown in the Figure 4.2.3.

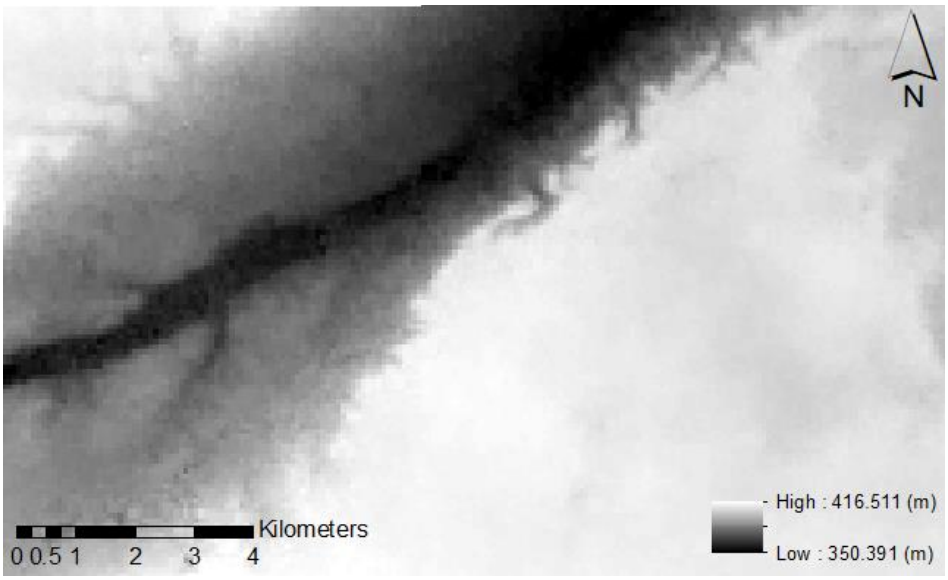

Figure 4.2.3 The Digital Elevation Model as the subset of 2D river channel of Wadi Al Batin.

Level 4 testing was for testing the variable Green-Ampt infiltration on flowing water and examining how it affects the simulated flow travel time within LISFLOOD-FP-vGA.

Testing the level 4 of LISFLOOD-FP-vGA model by running the simulations with three scenarios of initial simulation time step of 100 s and the simulation duration of 691,200 s as follow;

T4 S1: the simulation with no infiltration.

T4 S2: the simulation with steady constant infiltration of 0.000006 m/s.

T4 S3: the simulation with variable infiltration, Green-Ampt infiltration.

4.3 Results and discussions

The updated version, of the LISFLOOD-FP-vGA hydrodynamic model with the implementation of the Parlange model (PA) for explicit solution of Green-Ampt model has been tested at four main different testing levels as follows:

4.3.1 Testing level 1:

Figure 4.3.1 shows the accumulated infiltration and the infiltration rate on a simple case scenario over 10 hours simulations using the coded version of the explicit solutions of Green-Ampt model. It shows a monotonically increasing line of the accumulated infiltration over the simulation period starting from 0.012 m^3 at the first hour, and climbs reaching a maximum value of 0.04 m^3 at the end of the 10 hours simulation time. Figure 4.3.1 shows a monotonically decreasing infiltration rate over the simulation period starting from 0.000001767 m/s reaching the lowest value of 0.0000007202 m/s at the end of the 10 hours. Furthermore, the accumulated infiltration and the infiltration rate shows expected trends of monotonically decreasing and increasing lines all over the simulations period of 10 hours. The steeper curve shape at the start of the simulations is because of the amount of water infiltrated is higher at the beginning of the simulation run. Further testing to LISFLOOD-FP-vGA conducted by applying a steady infiltration rate of 0.000002 m/s to the model simulation run and compare the accumulated infiltration when applying the Green-Ampt variable infiltration versus applying the constant infiltration to the simulation run. The steady infiltration rate has arbitrary chosen for testing purposes.

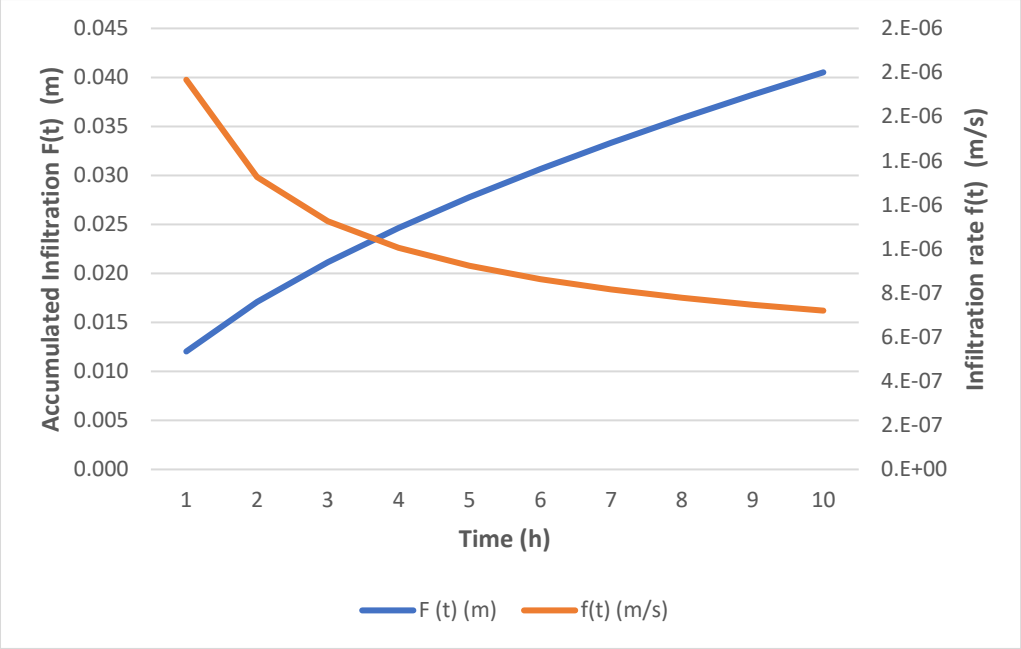

Figure 4.3.1 Accumulated infiltration and the infiltration rate of the test case 1 using the coded version of Green-Ampt model by visual basic.

Figure 4.3.2 shows high correlation between the accumulated infiltration results of the coded versions of the explicit solutions of Green-Ampt model which is embedded in Microsoft visual basic within Microsoft Excel sheet and the accumulated infiltration from the LISFLOOD-FP-vGA. Therefore, this gives promising initial indication that LISFLOOD-FP-vGA is working as expected. This similarity in the simulated accumulated infiltration results is expected because the accumulated infiltration is simulated using the same infiltration Green-Ampt variable model. Furthermore, the simulation flooded area over the 10 hours simulation time is equal to the single cell area of $1m^2$ as expected.

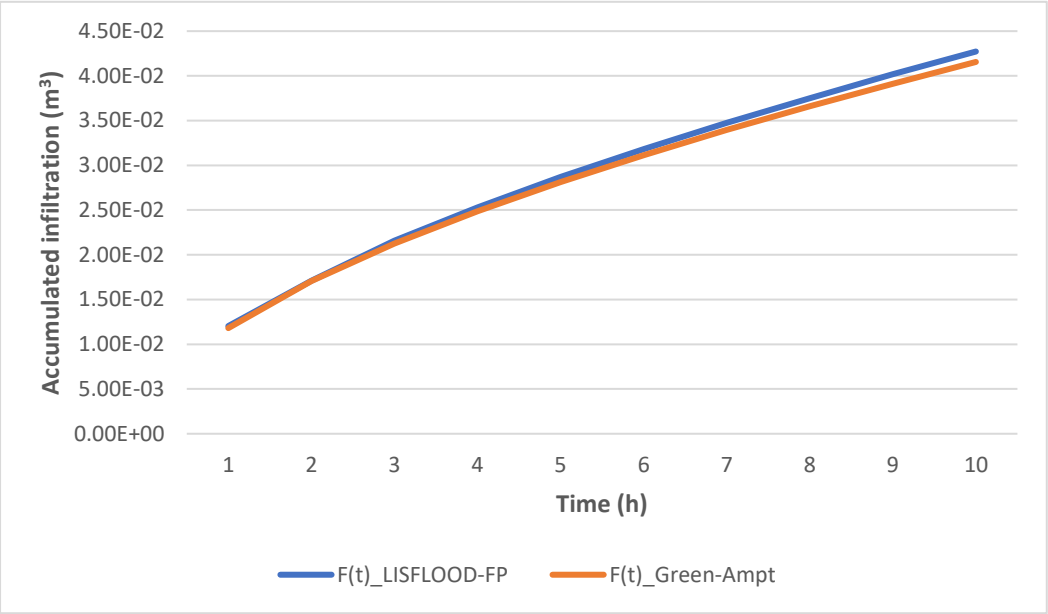

Figure 4.3.2 Accumulated infiltration F(t) comparison between LISFLOOD-FP-vGA model and the Green-Ampt model coded by visual basic.

The simulation results retrieved from LISFLOOD-FP-vGA model *mass* output file shows the water volume remaining on soil over the 10 hours simulations starts of 0.0828 m^3 from the first hour of the simulation reaching 0.018 m^3 at the end of the simulation time of 10 hours. On another hand, the simulation flooded area over all of the 10 hours simulation time is 1.0 m^2.

Figure 4.3.3 shows the infiltration comparison between steady infiltration simulation of LISFLOOD-FP-vGA model and the Green-Ampt simulation of LISFLOOD-FP-vGA. Figure 4.3.3 shows monotonically increasing of Green-Ampt accumulated infiltration starting from 0.0118 m^3 at the first hour to reach 0.0416 m at the end of the simulation time of 10 hours. Figure 4.3.3 shows constant accumulated infiltration increase over all of the simulation when applying a constant infiltration rate of 0.000002 m/s. This accumulated infiltration increased as at a constant rate from 0.0072 m^3 at the first hour of the simulation until reaching the 0.072 m^3 at the end of the simulation of 10 hours. Figure 4.3.3 shows that amount of water infiltrated when applying a constant infiltration is higher when applying variable Green-Ampt infiltration. Therefore, this gives an initial indication of an approximate successful testing as the model behaving as expected.

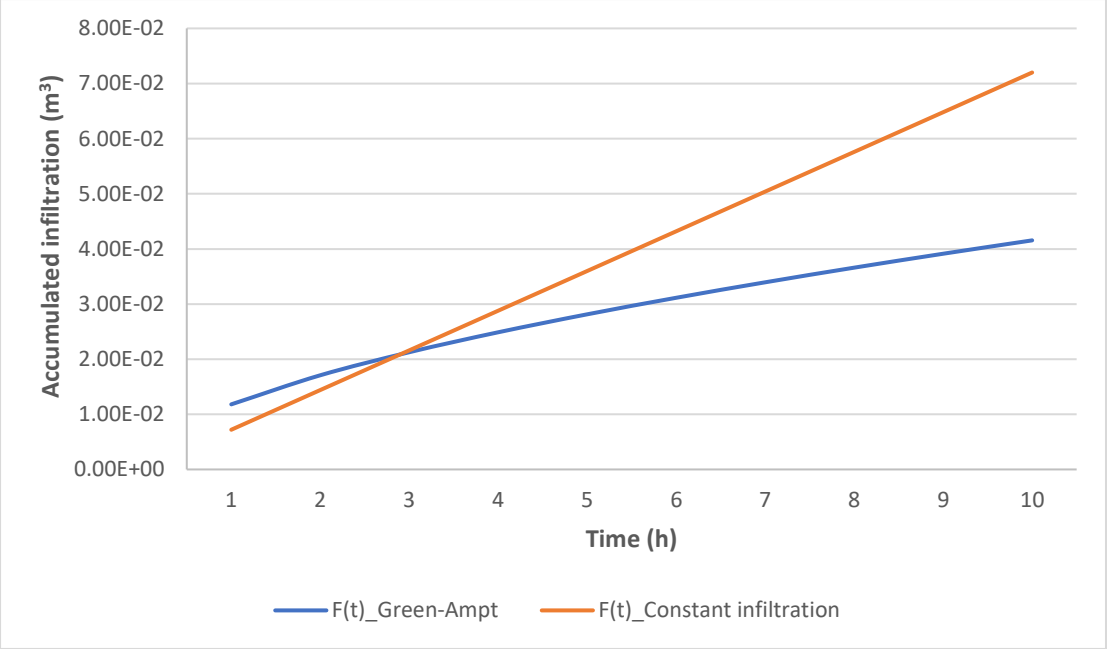

Figure 4.3.3 Comparison between the steady infiltration and the Green-Ampt variable infiltration by LISFLOOD-FP-vGA model simulation.

4.3.2 Testing level 2

Figure 4.3.4 shows for the S1 scenario where there is no infiltration applied to the model, the travel time needed for the model to start getting wet is 39 s. Therefore, this travel time takes longer for the S2, where there is a steady infiltration of 0.00006 m/s applied to the model which starts getting wet at 43 s. Furthermore, Figure 4.3.4 shows that travel time for the S3 simulations is 40 s.

This difference in travel time is because there is no infiltration loss for the S1 scenario which makes the flow travel time quicker in comparison with S2 and S3. Furthermore, Figure 4.3.4 shows the travel time is shorter for S3 in comparison with S2. This is again because of the amount of water infiltrated at S3 is less than in S2 which makes the flow travel quicker.

The simulation results of the three scenarios show that the model reaches the steady state after approximately 500 s with a water depth of 0.093 m.

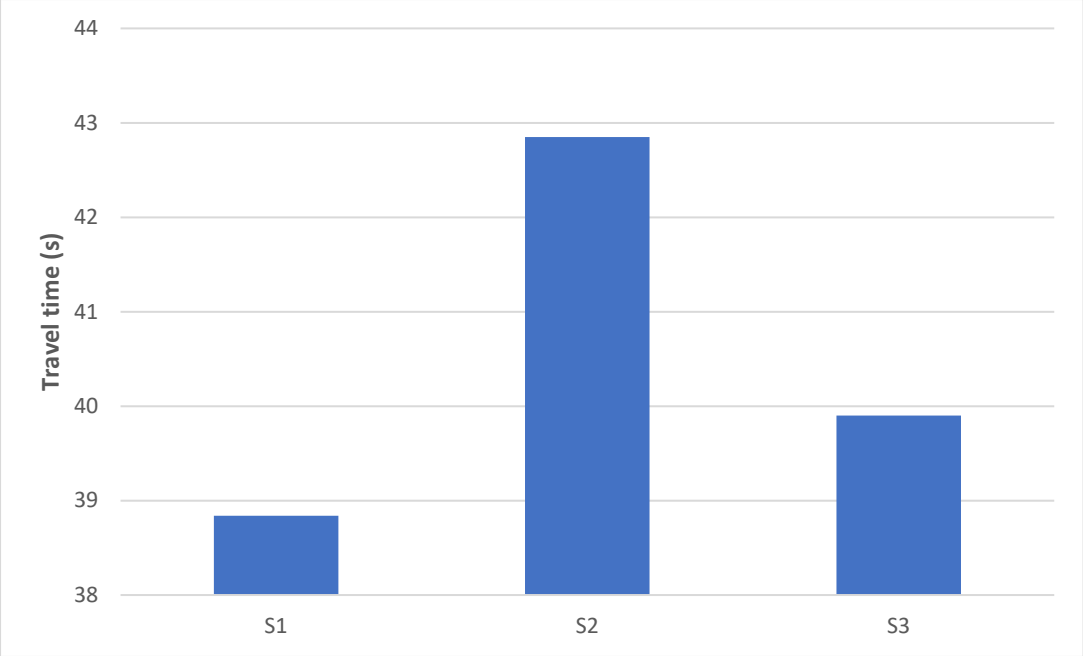

Figure 4.3.4 Comparison of the flood travel time of the LISFLOOD-FP-vGA model three scenarios (S1, S2, S3).

Figure 4.3.5, shows the accumulated infiltration LISFLOOD-FP-vGA comparison between S2 and S3 scenarios (as described in 4.2.2) simulated by LISFLOOD-FP-vGA, where the S2 steady infiltration increased constantly to reach 0.53 m and presented by a straight line on the graph. Figure 4.3.5, also shows that the S3 Green-Ampt variable infiltration increasing as a curve from the start of the simulation run to approximately at 200 s where the model reaches the steady infiltration, and the line becomes straight (constant rate of increase) reaching the maximum infiltration value of 0.649 m.

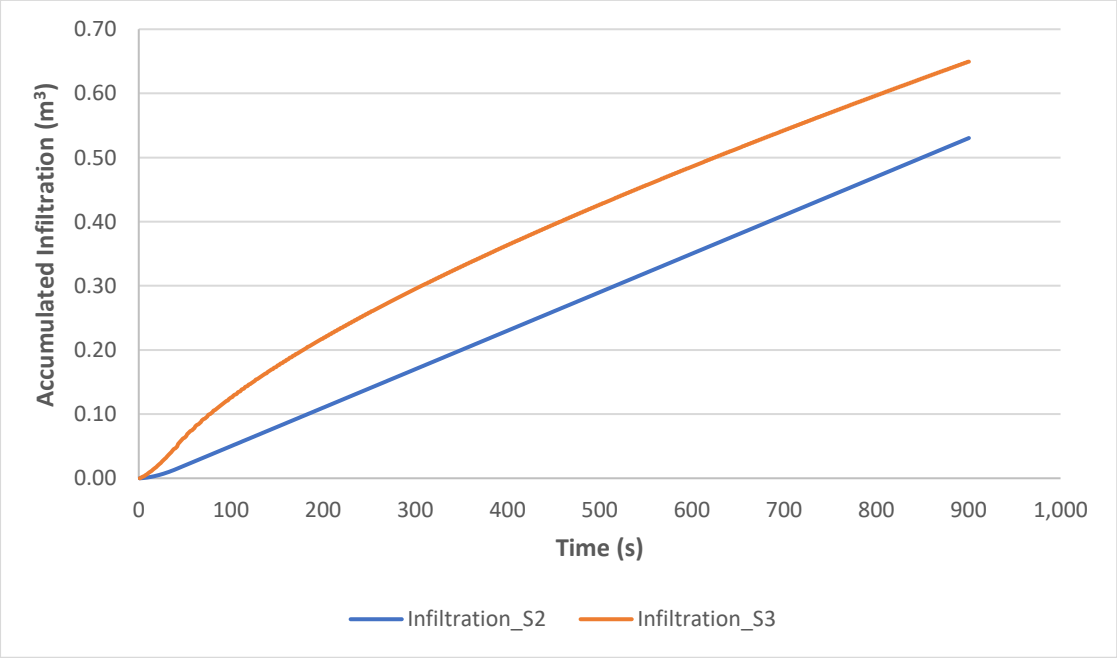

Figure 4.3.5 Shows the infiltration loss comparison between S2 and S3 scenarios simulated by LISFLOOD-FP-vGA.

Figure 4.3.6, shows for S1 at the steady state, around 500 s, a constant level all over the 10 cells for a water depth value of 0.093 m. Furthermore, Figure 4.3.6, also shows a water surface elevation decreasing from 1.093 m for the cell 1 reaching 1.084 m for the cell 10. This result shows a reasonable explanation of constant water depth all over the 10 cells due to there is no infiltration loss applied to the S1 LISFLOOD-FP-vGA simulation.

The simulation results retrieved from LISFLOOD-FP-vGA model mass output file for the scenario 1 shows the water volume over the 900 s simulation starts of 0.01m^3 and reaching 0.9266 m^3 at the end of the 900 s. The simulated flooded area reaches 10 m^2 at time.

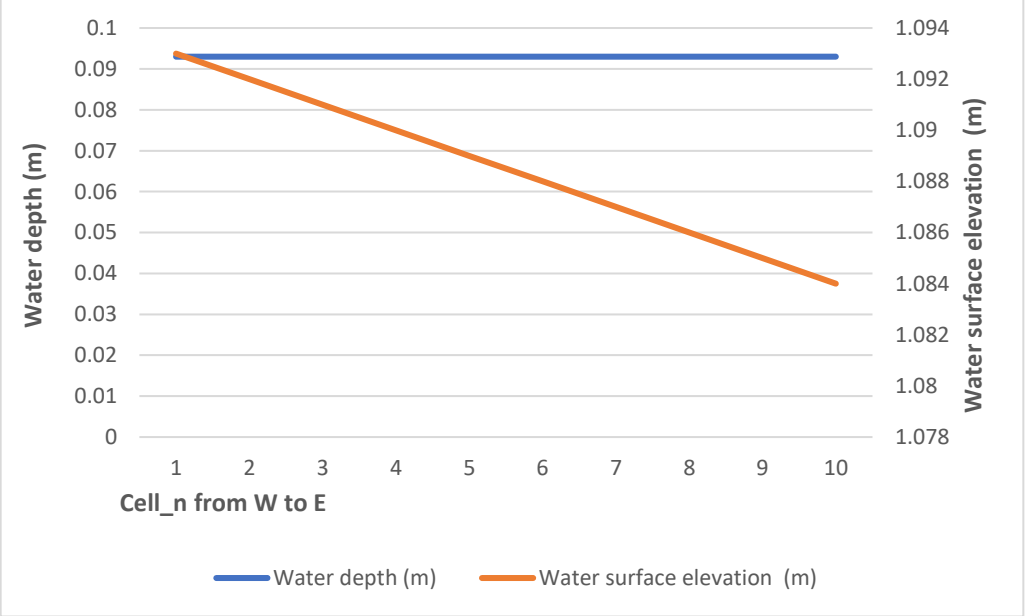

Figure 4.3.6 Water depth and water surface elevation for the scenario 1 at the steady state simulated by LISFLOOD-FP-vGA.

Figure 4.3.7 shows for the S 2 at the steady state around 500 s a decreasing straight line over all 10 cells for a water depth from 0.0898 m on the cell number 1 reaching the water depth of 0.0893 m on the cell number 10. This result shows a reasonable explanation of decreasing water depth from cell number 1 to cell number 10 due to the constant infiltration loss, therefore less water reaching the lower cells elevation. Furthermore, Figure 4.3.7 shows a water surface elevation decreasing from 1.09 m for the cell 1 reaching 1.08 m for the cell 10.

The simulation results retrieved from LISFLOOD-FP-vGA model mass output file for the S2 shows the water volume over the 900 s simulations starts of 0.01 m^3 from the start of the simulations reaching 0.89474 m^3 at the end of the simulation time of 900 s. The simulated flooded area reaches 10 m^2 at the end of the simulation time of 900 s.

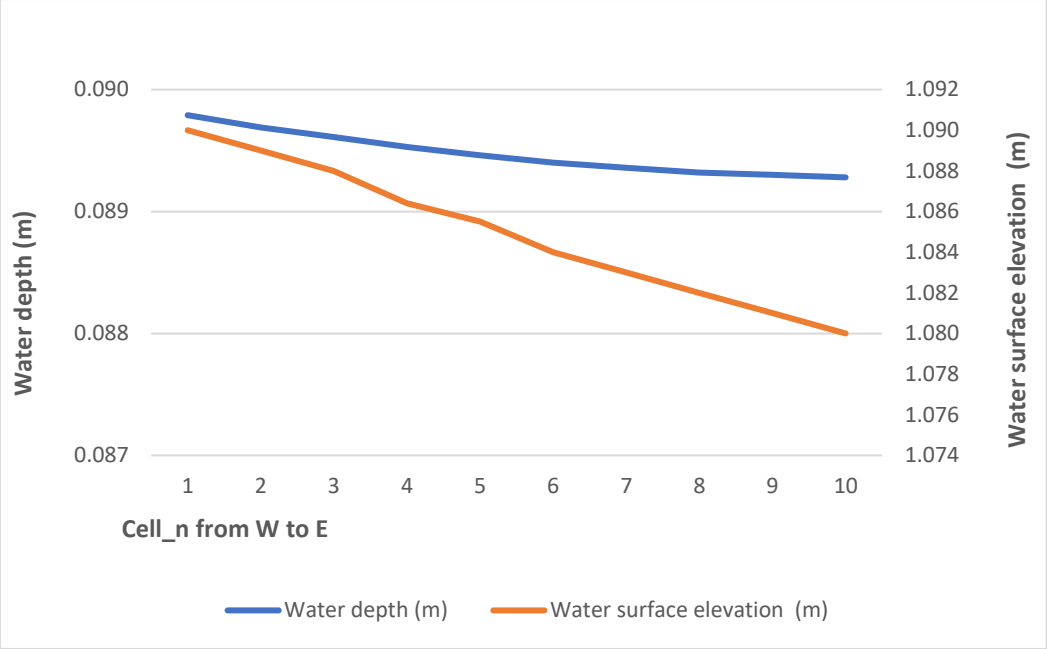

Figure 4.3.7 Water depth and the water surface elevation for the scenario 2 at the steady state simulated by LISFLOOD-FP-vGA.

Figure 4.3.8, shows the S3 results at the steady state (around 500 s) as a monotonically decreasing line over all the 10 cells for a water depth from 0.0901 m at cell number 1 reaching the water depth of 0.0897 m at cell number 10. This result shows a reasonable explanation of decreasing water depth from cell number 1 to cell number 10 due to the variable Green-Ampt infiltration loss, therefore less water reaching the lower elevation cells. Furthermore, Figure 4.3.8 shows a water surface elevation decreasing from 1.09 m for cell 1 reaching 1.0810 m for cell 10.

The simulation results from LISFLOOD-FP-vGA model mass output file for the scenario 3 shows the water volume over the 900 s simulations starts of 0.01 m^3 from the start of the simulations reaching 0.89866 m^3 at the end of the simulation run time of 900 s.

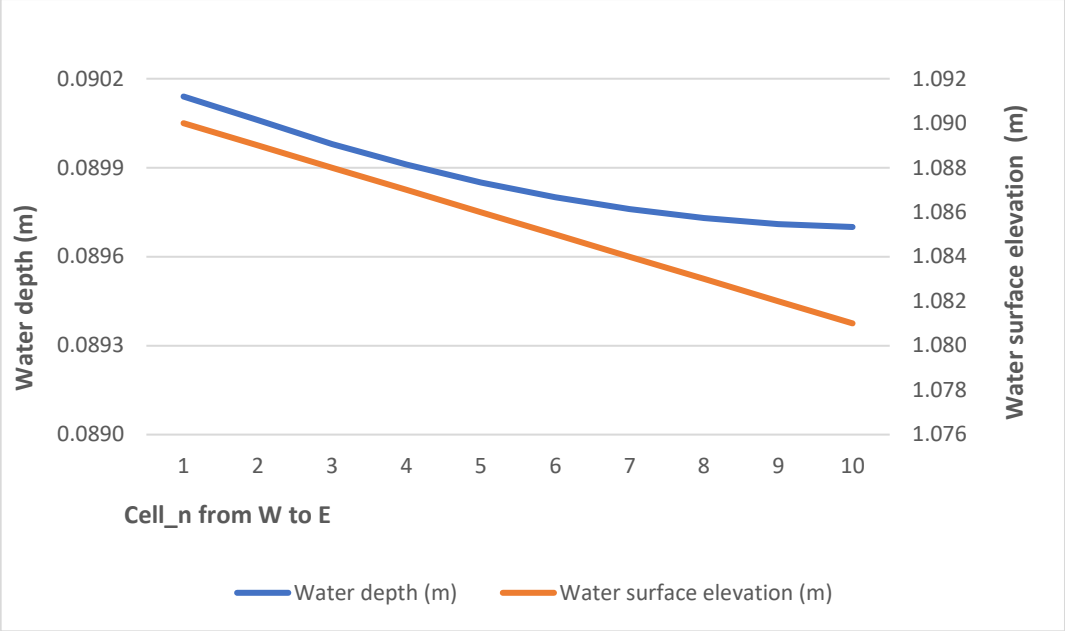

Figure 4.3.8 Water depth and the water surface elevation for the scenario 3 at the steady state simulated by LISFLOOD-FP-vGA.

4.3.3 Further Level 2 testing:

LISFLOOD-FP-vGA simulated Infiltration Loss comparison between the S2 A and S3 A scenarios as described in 4.2.2 has carried out as shown in the Figure 4.3.9.

Figure 4.3.9, shows as expected for S2 A scenario a straight line increase of the infiltration loss reaches 0.54 m at the end of the model simulation period by LISFLOOD-FP-vGA. On the another hand, the Figure 4.3.9 shows for an S3 A a clear curve for the first 200 s from the LISFLOOD-FP-vGA model simulations of the variable Green-Ampt infiltration loss until reaching the steady infiltration loss to the end of the model simulation.

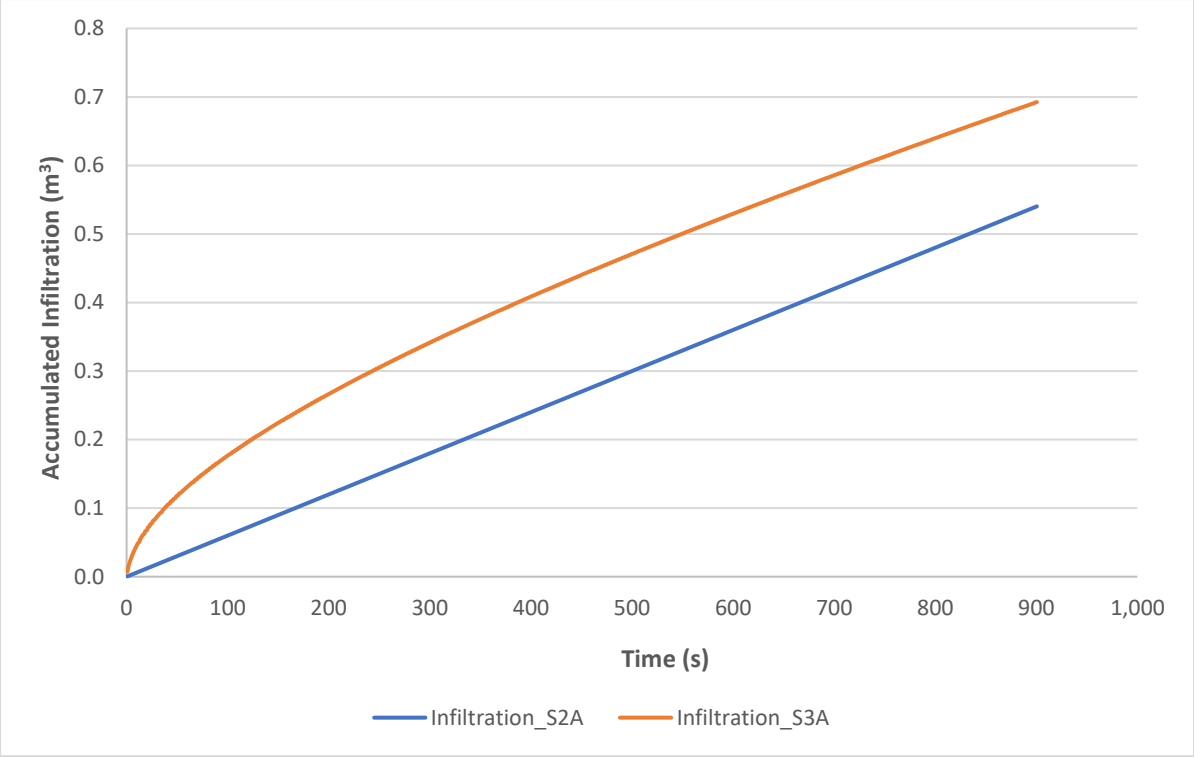

Figure 4.3.9 The infiltration loss comparison between S2 A and S3 A scenarios simulated by LISFLOOD-FP-vGA.

A comparison between simulated Infiltration loss by LISFLOOD-FP-vGA for S3 and S3 A scenarios as shown in the Figure 4.3.10 explains the effect of setting an initial model depth of 0.093 m at the start of the simulation run as in the S3 A. Figure 4.3.10 shows the clear curve for the S3 A scenarios from the start of the simulation however, the curve takes longer, by approximately 50 s, than the S3 scenario where the model takes time to start getting wet. This is what is expected when the simulation has added initial model depth at the start of the simulation.

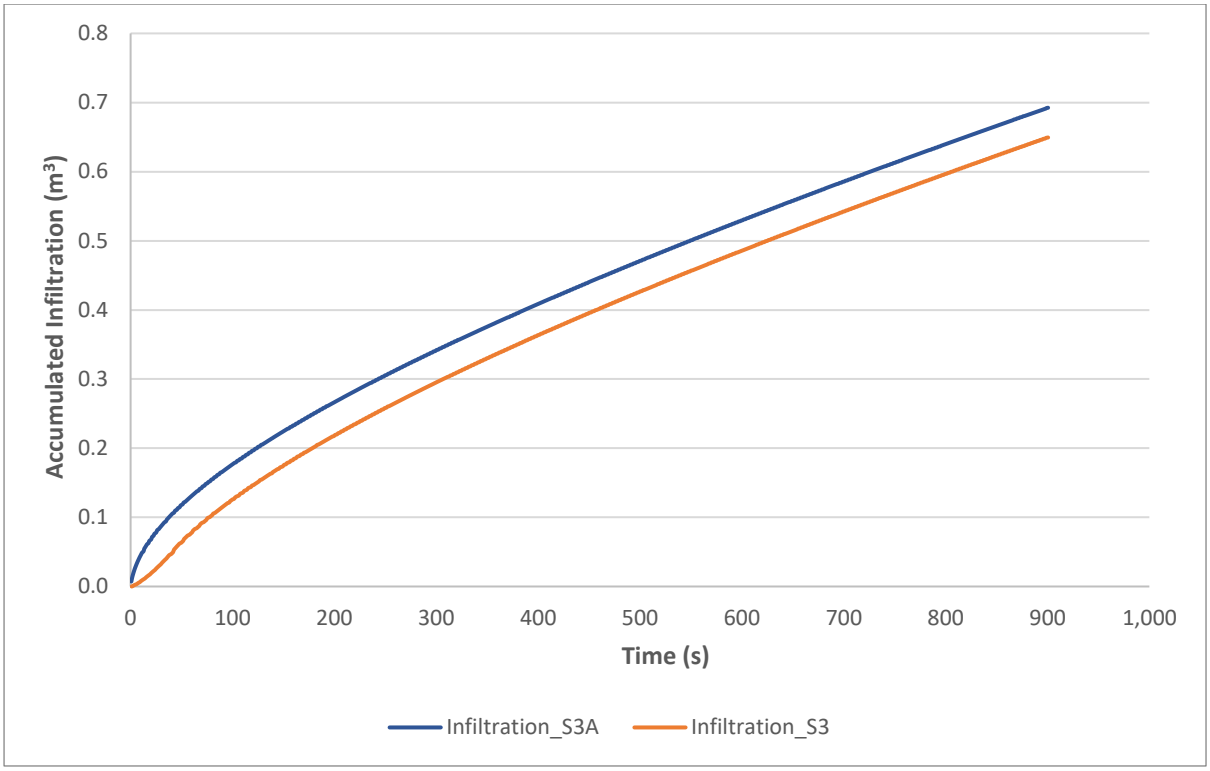

Figure 4.3.10 The infiltration loss comparison between S3 and S3 A scenarios simulated by LISFLOOD-FP-vGA.

Further testing was carried out by calculating the water balance for the three S1 A, S2 A and S3 A scenarios. The water balance calculation was estimated by subtracting the out flow and the model errors from the constant inflow applied to the LISFLOOD-FP-vGA model simulation run for the three scenarios.

The water balance calculation was carried out for the scenarios with setting an initial model depth of 0.093 m at the start of the simulation run S1 A, S2A and S3 A as shows in the for the steady state simulation period of the LISFLOOD-FP-vGA model.

Figure 4.3.11, shows the water balance calculation of the S1 A all the water entering the model domain exits the model, this is presented in the graph by straight line of 0 m^3/s value over all the steady state simulation period. The straight line is explained as there is no infiltration loss applied to LISFLOOD-FP-vGA model.

For the S2 A, Figure 4.3.11 shows constant line all over the steady state simulation period. This is explained because of the constant infiltration rate applied to LISFLOOD-FP-vGA.

Therefore, for the S3 A Figure 4.3.11 shows monotonically decreasing curve due to the Green-Ampt variable infiltration which shows a higher water balance residue in comparison with the S2 A at the start of the simulation and getting less than S2 from around 550 s of LISFLOOD-FP-vGA simulation run.

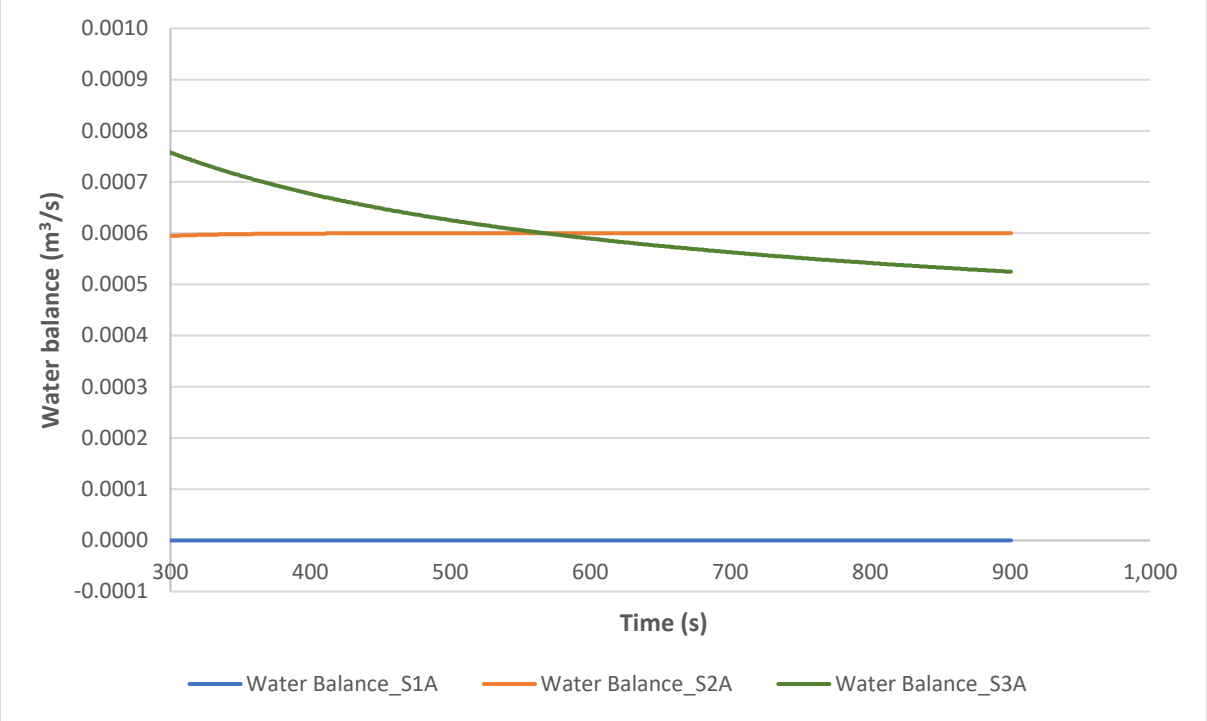

Figure 4.3.11 Water balance calculations for the three scenarios S1 A, S2 A and S3 A simulated by LISFLOOD-FP-vGA.

4.3.4 Testing level 3:

Figure 4.3.12, shows the water depth simulation results on various time steps simulation run of 100 hours by LISFLOOD-FP-vGA which clearly shows a water depth variation between the model domain centre cells and the surrounded cells. This is due to the centre cells soil characters which have soil reference 2 of sandy clay loam are varies from the surrounded cells in the model domain which have soil reference 1 of clay loam.

Furthermore, Figure 4.3.12 also shows water depth results vary from 0.25 m at the early simulation time of 50 hours in the domain reducing to 0.044 m at the end of the simulation time of 190 hours due to the loss from the accumulated infiltration all over the simulation time of 3600 s. Therefore, these results show a successful testing of assessing the spatially distributed accumulated infiltration using LISFLOOD-FP-vGA.

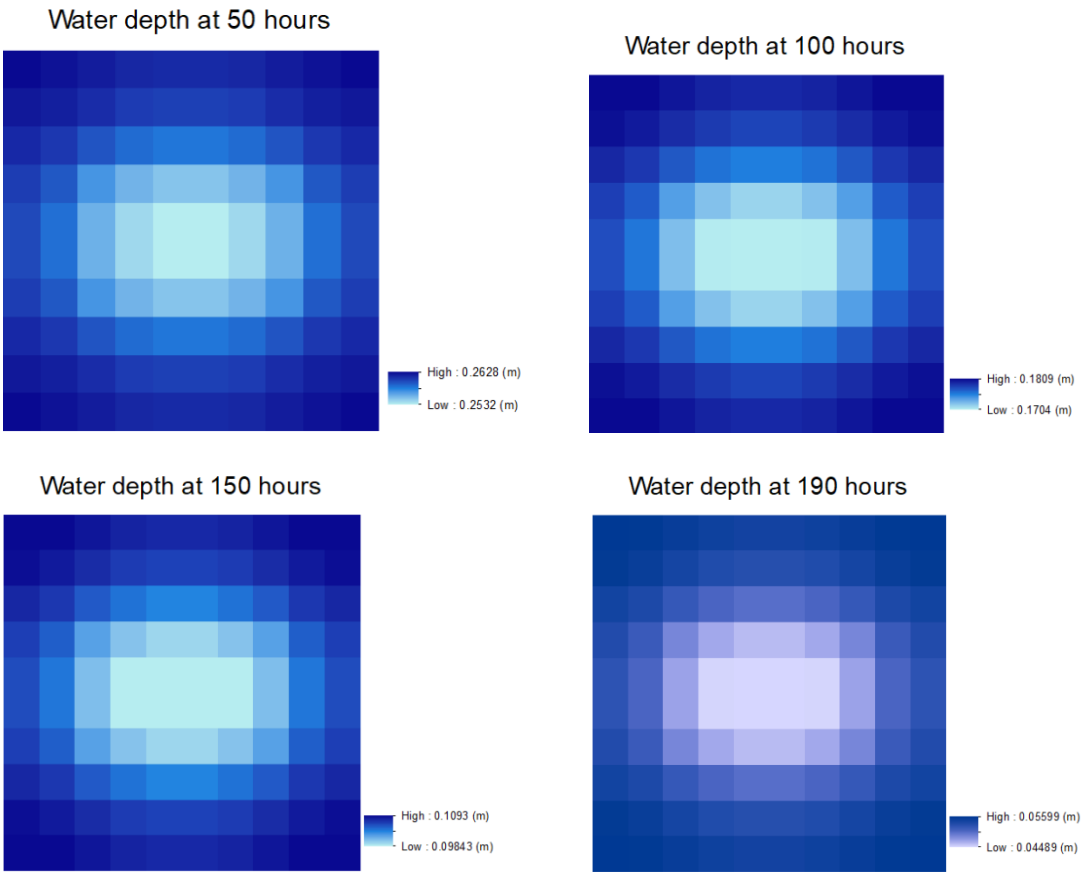

Figure 4.3.12 Water depth variation at deferent simulation run time by LISFLOOD-FP-vGA.

4.3.5 Testing level 4:

Figure 4.3.13 shows for the scenario T4 S1 where there is no infiltration applied to the model, the flow travel time needed for the simulation LISFLOOD-FP-vGA model to start getting wet is 137,000 s. Therefore, this travel time is longer for the scenario T4 S2, where a steady infiltration has applied to the simulation model which start getting wet at 158,000 s. Furthermore, Figure 4.3.13 shows that the travel time for the T4 S3 simulations is 142,000 s which is less than the travel time for the scenario T4 S2.

Figure 4.3.13, shows the flow travel time for the T4 S1 is shorter than T4 S2 and T4 S3 because of no infiltration loss is applied to the model, therefore the flow is quicker. Furthermore, it is expected that the travel time for T4 S3 is shorter than T4 S2 because of the water volume infiltrated in T4 S3 is less than the amount of water volume infiltrated in T4 S2.

The LISFLOOD-FP-vGA simulation results of the three scenarios show that the model reaching the steady state approximately on 400,000 s with an average water depth of 2 m.

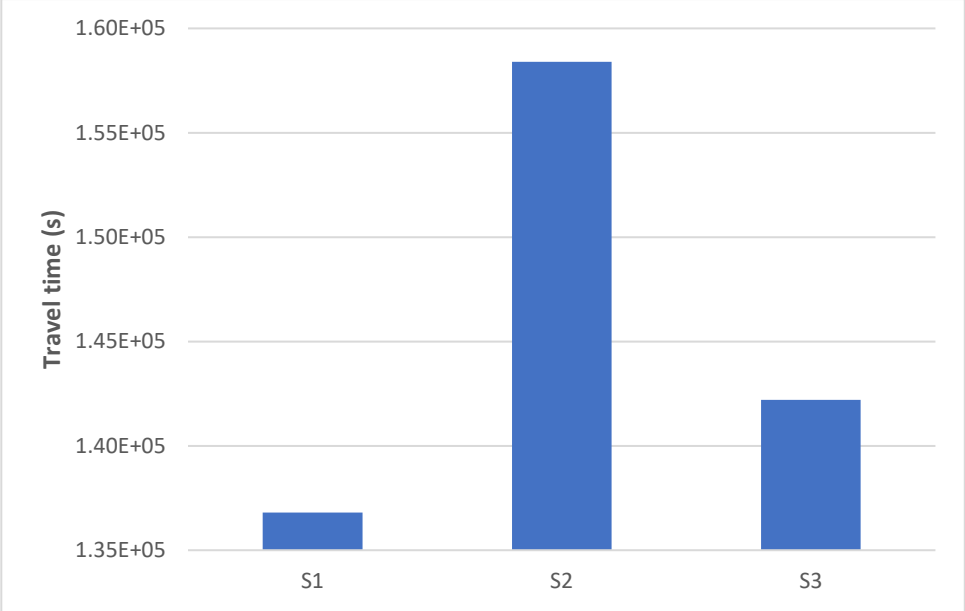

Figure 4.3.13 Comparison between the flood travel time of the three scenarios (T4 S1,T4 S2,T4 S3) simulated by LISFLOOD-FP-vGA.

Figure 4.3.14, shows the accumulated infiltration comparison between T4 S2 and T4 S3 scenarios where the T4 S2 steady infiltration starts from 0 to be increased constantly to reach 20,900,000 m^3 and presented by a straight line over all the simulation period of 691,200 s.

Figure 4.3.14 shows the T4 S3 variable infiltration monotonically increasing as a curve from 0 to approximately 200 s where the model reaches the steady infiltration, and the curve becomes straight reaching the maximum infiltration value of 2,970,000 m^3.

This comparison shows as expected that the water volume infiltrated when applying variable Green-Ampt infiltration is less than the amount of water volume infiltrated when applying a constant infiltration to LISFLOOD-FP-vGA simulation run.

The simulation results retrieved from LISFLOOD-FP-vGA model mass output file for the scenario T4 S2 shows the water volume over the 691,200 s simulations starts of 10,000 m^3 from the start of the simulations reaching 13,305,000 m^3 at the end of the simulation time of 691,200 s. The simulation flooded area starts from 29,499 m^2 at the start of the simulation, therefore, it reaches 5,737,600 m^2 at the end of the simulation time of 691,200 s.

Furthermore, the simulation results retrieved from LISFLOOD-FP-vGA model mass output file for the scenario T4 S3 shows the water volume over the 691,200 s simulations starts at 10,000 m^3 and reaches 13,760,000 m^3 at the end of the simulation time of 691,200 s. The simulation flooded area starts from 29,499 m^2 at the start of the simulation reaches 5,892,500 m^2 at the end of the simulation time of 691,200 s.

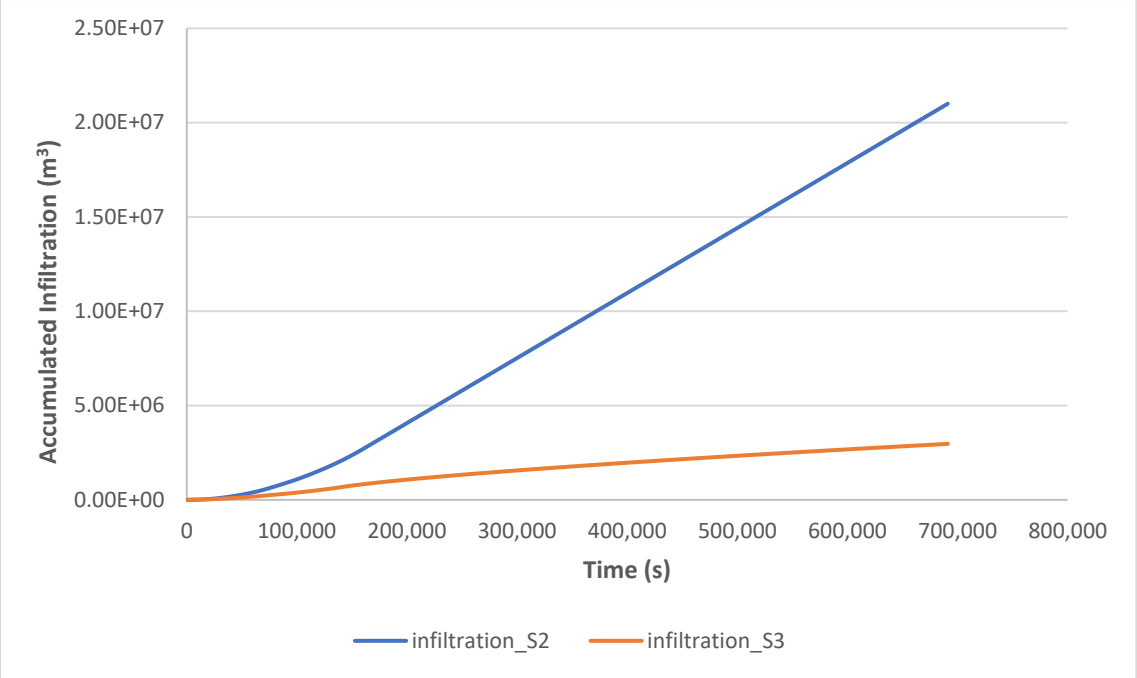

Figure 4.3.14 infiltration loss comparison between T4 S2 and T4 S3 scenarios simulated by LISFLOOD-FP-vGA.

Lastly, the above discussion shows the models results pattern as expected. This again gives an indication of an approximate credibility of the successful testing of this model.

4.4 Slope angle Sensitivity testing

The effect of slope angle on the Green-Ampt model has been tested by incorporating the angle in the implicit Equation 3 and then solved using the Newton–Raphson method (Rao et al., 2006). The test has been conducted on clay Loam, silt loam and sandy loam with ponding water of 9 cm. The Green-Ampt parameters used are those developed by Rawls et al. (1983) as shown in the Table 4.4.1.

Figure 4.4.1 and Table 4.4.2 Simulated accumulated infiltration of various slope angles of clay loam soil type. show at 10 hours simulation time a minor accumulated infiltration variation of 0.011, 0.025, 0.043, 0.067, 0.096, 0.13, 0.168, 0.209, 0.255, 0.303, and 0.355 cm with increasing the angle slope of 5°, 10°, 15°, 20°, 25°, 30°, 35°, 40°, 45°, 50°, 55° and 60° respectively. Figure 4.4.1 and Table 4.4.2 show a decrease in accumulated infiltration with increasing the slope, therefore, more surface runoff generation.

Figure 4.4.1 shows monotonically increasing gradient curves over the 10 hour simulations. Furthermore, it shows the simulated infiltration difference becomes greater during the simulation duration.

Figure 4.4.1 and Table 4.4.2 show the implication of the slope angle as increasing with increasing the slope. However as mentioned above, the largest increase is of 0.355 cm after 10 hours of simulations

at 60° of slope angle, therefore it is not having a significant impact on the data analysis and the conclusion of this study. Moreover, as mentioned earlier, Wadi Al Batin valley is not a steep catchment having an approximate slope of 0.0006. Therefore, the effect of the slope angle on Green-Ampt equation at Wadi Al Batin is negligible.

Moreover, Chen and Young (2006) studied the implications of sloping surfaces on modelling with the Green-Ampt equation. They found that the effect is negligible for slope angle less than 10°. Therefore, in most practical cases, it will not affect the simulated accumulated infiltration by anything more than a negligible amount.

Lastly, Figure 4.4.2 and Figure 4.4.3 show both similar simulated patterns of the accumulated infiltration when silty loam and sandy loam soil types were considered in comparing to Figure 4.4.1 when clay loam soil type was considered. Therefore, it can be considered to give an approximate credibility of the sensitivity analysis conclusion, which is related to the negligible effect of the slope angle on Green-Ampt equation at Wadi Al Batin.

Table 4.4.1 Green-Ampt physical parameters of various soil type textures from Rawls et al. (1982).

Soil texture class	**Residual porosity**	**Effective porosity**	**Suction head (cm)**	**Hydraulic conductivity (cm/h)**
Clay loam	0.155	0.309	20.88	0.1
Silt loam	0.015	0.486	16.68	0.65
Sandy loam	0.041	0.412	11.01	1.09

Table 4.4.2 Simulated accumulated infiltration of various slope angles of clay loam soil type.

Accumulated Infiltration (cm)													
T(h)	**0°**	**5°**	**10°**	**15°**	**20°**	**25°**	**30°**	**35°**	**40°**	**45°**	**50°**	**55°**	**60°**
1	1.204	1.204	1.203	1.201	1.200	1.197	1.195	1.191	1.188	1.184	1.179	1.175	1.170
2	1.743	1.742	1.741	1.738	1.734	1.730	1.724	1.718	1.710	1.702	1.694	1.684	1.674
3	2.173	2.172	2.170	2.166	2.160	2.153	2.145	2.135	2.124	2.112	2.098	2.084	2.069
4	2.546	2.545	2.542	2.537	2.529	2.520	2.509	2.496	2.481	2.465	2.447	2.428	2.408
5	2.884	2.883	2.879	2.872	2.863	2.851	2.837	2.821	2.802	2.781	2.759	2.735	2.710
6	3.197	3.195	3.190	3.182	3.171	3.157	3.140	3.120	3.097	3.073	3.046	3.017	2.986
7	3.490	3.488	3.482	3.473	3.460	3.443	3.423	3.400	3.374	3.345	3.313	3.279	3.244
8	3.768	3.765	3.759	3.748	3.733	3.714	3.691	3.664	3.634	3.601	3.565	3.526	3.486
9	4.033	4.031	4.023	4.011	3.994	3.973	3.947	3.917	3.883	3.845	3.805	3.761	3.715

10	4.288	4.285	4.277	4.264	4.245	4.221	4.192	4.158	4.121	4.079	4.034	3.985	3.934

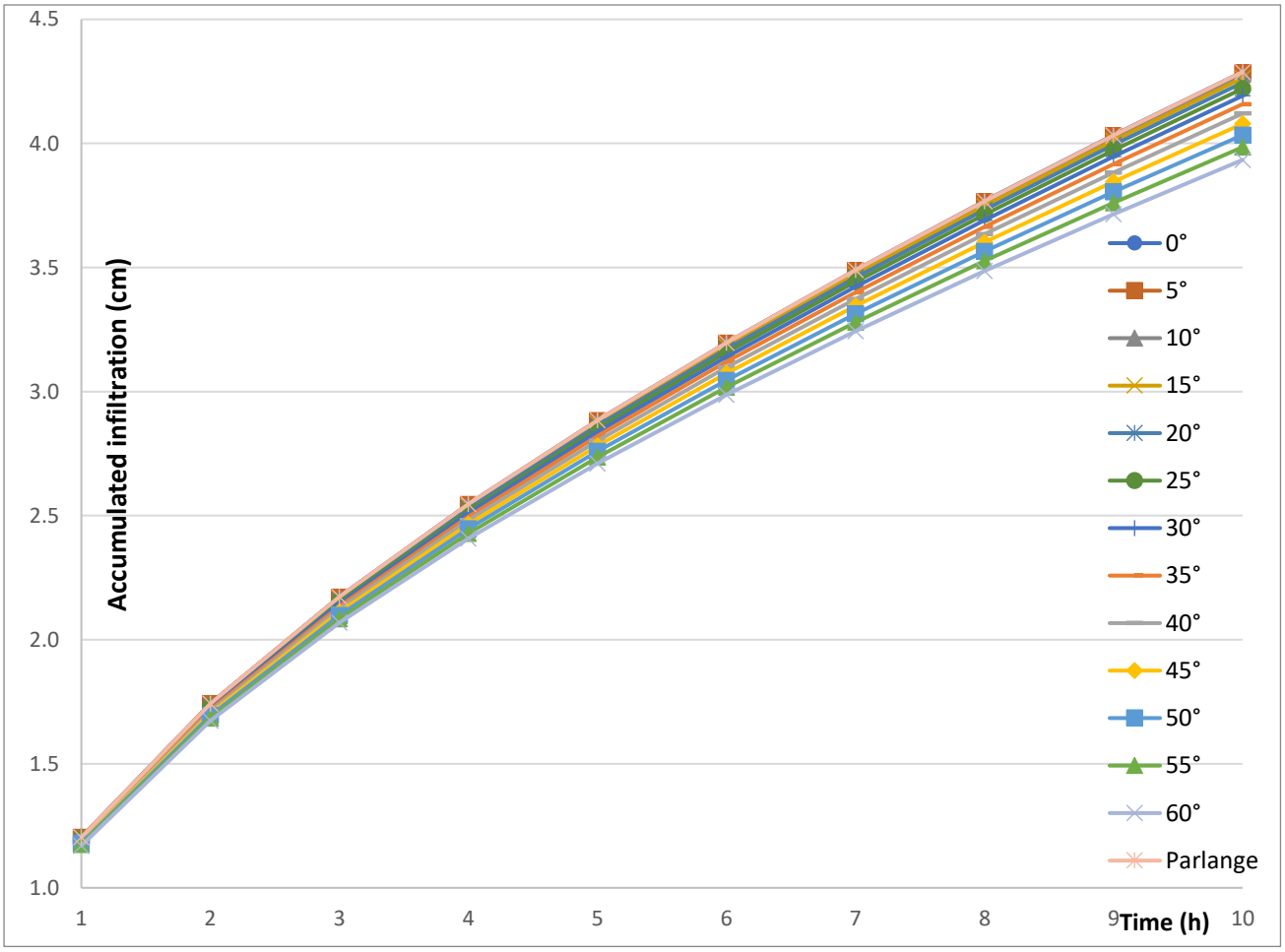

Figure 4.4.1 Simulated accumulated infiltration of various slope angles of clay loam soil type.

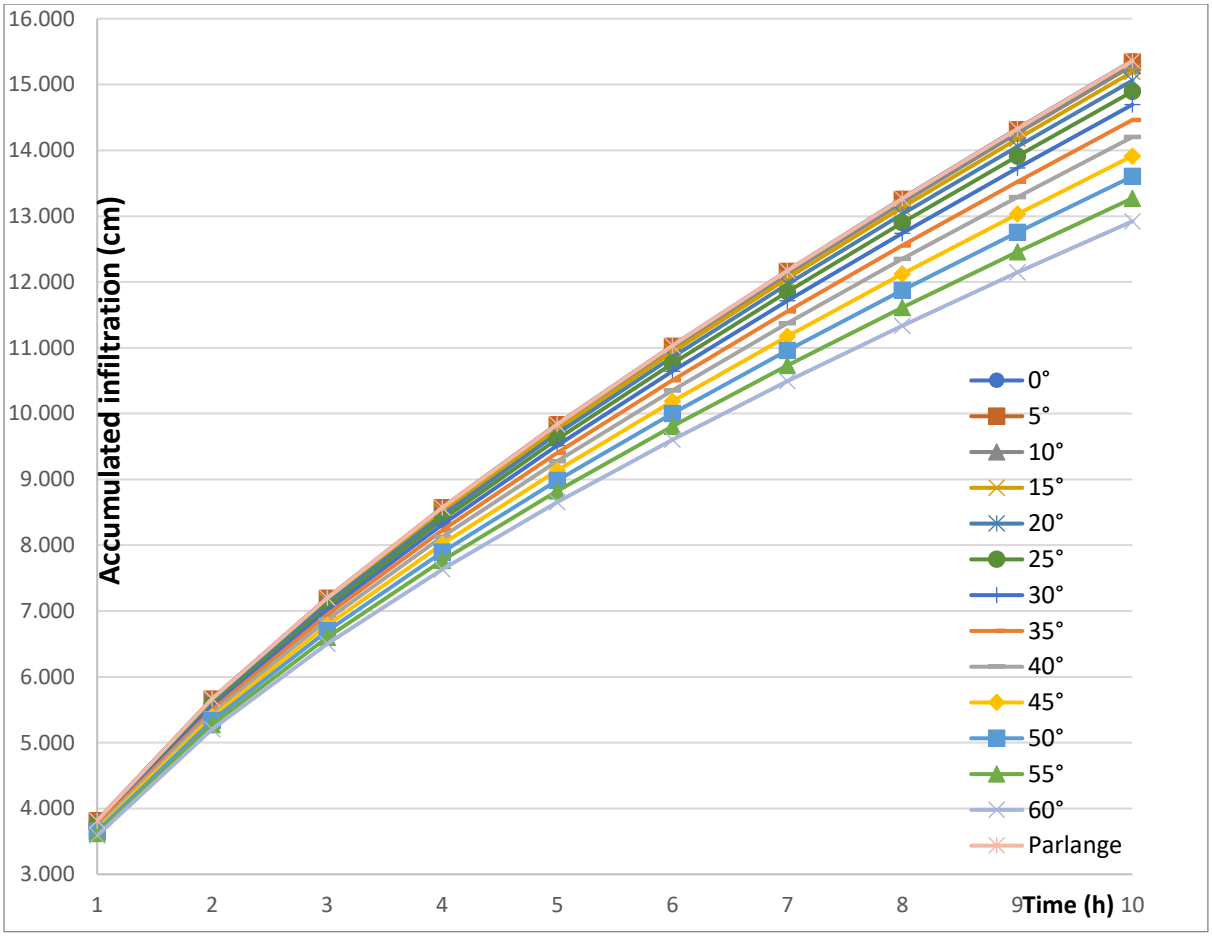

Figure 4.4.2 Simulated accumulated infiltration of various slope angles of silt loam soil type.

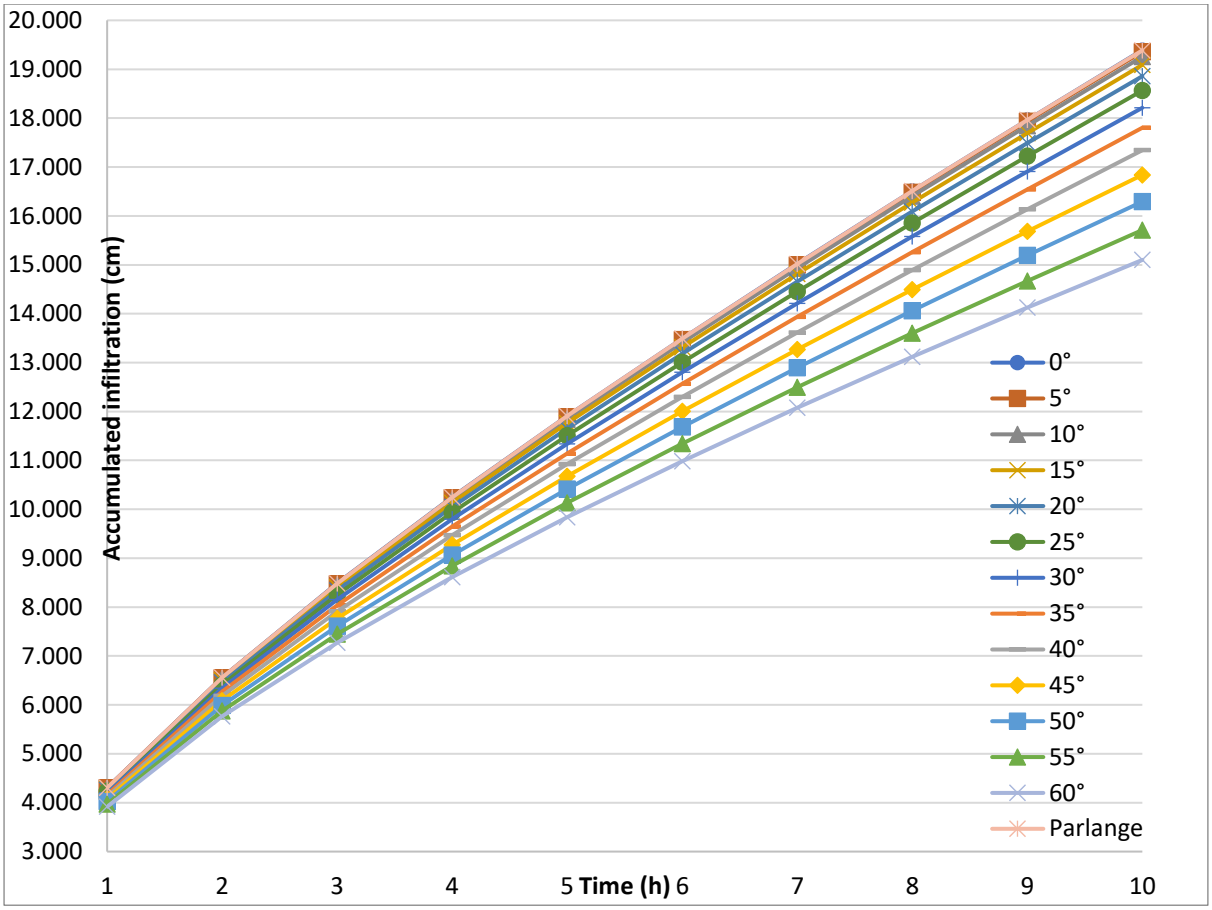

Figure 4.4.3 Simulated accumulated infiltration of various slope angles of sandy loam soil type.

4.5 Conclusion:

This chapter has presented results of simulations testing LISFLOOD-FP-vGA at various levels of complexity to understand the performance of the Green-Ampt infiltration model. These tests include the spatial distribution of variable Green-Ampt accumulated infiltration. The simulated infiltration results from LISFLOOD-FP-vGA show reasonably expected results from Green-Ampt variable infiltration across the simulations domain. It also shows how significant the effect of the Green-Ampt variable infiltration is on the flow travel time.

The tests undertaken are gradually varying in complexity: from ponding infiltration testing with non-flowing of one-meter cell size testing to more sophisticated testing of river channel conceptual simplification. This channel is represented by a line of 1m cell size of 10 cells, simulating a small subset of a 2D river channel from Wadi Al Batin in Saudi Arabia. Also tested was the Green-Ampt accumulated infiltration spatial distribution on 10x10 cells of 200 m cell size while setting an initial model depth of 0.4 m of ponding water and two deferent soil texture types.

Firstly, it is concluded that Test 1, looking at ponding infiltration with non-flowing water on a one-meter cell size, was successful. This conclusion is based on the similarity of the accumulated infiltration

results from the LISFLOOD-FP-vGA simulation in comparison with the accumulated infiltration from Green-Ampt model.

Secondly, it is concluded that Test 2 was also successful. This test was a more sophisticated testing using a conceptually simplified river channel represented by line of 1m cell size of ten cells. This conclusion is based on the LISFLOOD-FP-vGA simulation results of various scenarios where there was no infiltration, steady infiltration and Green Ampt variable infiltration.

The simulation results show a constant water depth over all 10 cells for the no-infiltration scenario. It shows for steady and variable infiltration scenarios decreasing water depth results all over 10 cells simulation domain from cell number 1 until cell 10 due to the infiltration loss, which leads to less volume of flow reaching the end of the 10 cells simulation domain. The Test 2 conclusion is also based on the accumulated infiltration of LISFLOOD-FP-vGA simulation results that are judged as physically reasonable and sensible. The comparison between the constant infiltration scenario and the Green-Ampt variable infiltration scenario shows an increasing gradient for the constant infiltration scenario while it shows a monotonically increasing gradient curve for Green-Ampt variable infiltration scenario as expected.

Furthermore Test 2 also demonstrated the correct water balance when testing 2 of the three simulations scenarios where the LISFLOOD-FP-vGA simulations run with no infiltration, steady infiltration and Green-Ampt variable infiltration. I.e., the results show all the inflow into the model are the same as the outflow where the simulation run with no infiltration. Therefore, the water balance results of second scenario where the simulations run with steady infiltration show a constant gradient line which presents the infiltration loss. Also, the water balance results of the third scenario with variable Green-Ampt infiltration show a monotonically decreasing curve which presents the variable infiltration loss.

Thirdly, Test 3, which was specifically aimed at testing the implementation of Green-Ampt infiltration with spatial distribution within LISFLOOD-FP-vGA was successful. This conclusion is drawn predominantly due to the results of this test that show a variation in the simulated water depth associated with various soil types in the simulation testing domain as expected.

Finally Test 4, which is more complex testing using a real river geometry - a short subset of 2D river channel from the Wadi Al Batin - was also successful. This conclusion is based on the results comparison between the constant infiltration and the Green-Ampt variable infiltration scenarios.

It is also concluded from the slope sensitivity testing analysis on Green-Ampt equation using various soil type textures, that the effect of the slope angle on Green-Ampt equation at Wadi Al Batin, is negligible.

In summary, the four tests and scenarios presented above together show a successful implementation of Green-Ampt within LISFLOOD-FP-vGA, and that this provides a tool for robust estimation of the spatial infiltration losses. This is important for the next steps of the work as this will be testing how significantly the flow travel time is affected by the infiltration loss.

During the LISFLOOD-FP-vGA testing no calibration was conducted to the model due to the data scarcity regarding the Wadi Al Batin from the water authority in Saudi Arabia. Furthermore, the model could not be tested on variable return period events because of the lack of the rainfall gauge data.

Following the four testing scenarios of LISFLOOD-FP-vGA, Chapter 5 will show results from runs of the simulations using the LISFLOOD-FP-vGA of the whole Wadi Al Batin and will discuss in detail the implications of Green-Ampt variable channel bed infiltration on the wave propagation in the Wadi Al Batin.

Chapter 5 The application of 2D hydraulic models to the study catchment and exploration of its implications on the flood wave progression in the ephemeral system

5.1 Introduction

In Chapter 3, the implications of a constant infiltration rate on the propagation of a flood wave in the Wadi Al Batin ephemeral river system were explored. Findings show that compared to a no infiltration scenario, the infiltration scenario has significant and important implications on the flood wave propagation, such as a 41.75 hour difference in the flow travel time, a 4.278 km^2 difference in flooded area, and 0.0112 km^3 in water volume. In addition, experiments were performed to test the effects of LISFLOOD-FP-vGA model spatial resolution on these impacts. These simulated results of flood wave propagation were shown to be sensitive to LISFLOOD-FP-vGA model resolution. In Chapter 4, a Green-Ampt numerical solution was developed with the ability to include a representation of spatial variable infiltration and implemented in LISFLOOD-FP-vGA.

In this chapter the application of variable spatial infiltration through the Green-Ampt model is demonstrated through the implementation in LISFLOOD-FP-vGA. In doing this the implications on the flood wave propagation characteristics such as, the flooded area, the water volume, and the flow travel time are determined. The study catchment area of Wadi Al Batin in Saudi Arabia as described in detail in Chapter 3 is again utilised.

In addition, in this chapter the implications of the digital elevation model spatial resolution on the wave propagation characteristics are assessed. These include the flooded area, the water volume and the flow travel time from the start of simulation until the flow wave reaches the outlet point.

Therefore, the aim of this chapter is to ascertain the importance and the role of the variable spatial infiltration and explore its implications for various flood wave propagation characteristics which will lead to more robust flood risk assessments, particularly in ephemeral systems, and potentially provide more effective flood risk resilience measures.

5.1.1 Research steps:

The following research steps have been conducted in order to achieve the aim of this chapter:

4. Setting up and building the 2D flood inundation model, the model boundary conditions, and the data input required for running the simulations using LISFLOOD-FP-vGA on Wadi Al Batin.

5. Running of LISFLOOD-FP-vGA with DEM at multiple spatial resolutions and various infiltration loss scenarios in order to conduct a sensitivity analysis. This also serves to explore the implications of these scenarios on the flood propagation characteristics such as, the flooded area, the water volume and the flow travel time in the study catchment area of Wadi Al Batin in Saudi Arabia.
6. Discussing the implications of spatial variable infiltration on the flood wave propagation, and whether multiple spatial resolution has an effect on these implications.

5.2 Methodology:

In order to assess the application of LISFLOOD-FP-vGA to the study catchment and explore the implications of spatial variable infiltration on flood wave propagation in the catchment study area of Wadi Al Batin in Saudi Arabia, two different 2D floodplain models have been built with DEMs at two spatial resolutions, 171m and 257m. The full details of these two models are described in Chapter 3. The simulations run using LISFLOOD-FP-vGA cover three different scenarios. These scenarios consist of:

1. applying no infiltration over the whole simulation flow domain.
2. applying the constant infiltration over the whole simulation flow domain.
3. applying the variable Green-Ampt spatial infiltration over the whole simulation flow domain.

These will enable to establishment of the implications of the various infiltration loss scenarios on the flood wave propagation characteristics as discussed previously.

As stated above each simulation was carried out at a resolution of 171m and 257m to establish whether and how the Green-Ampt variable infiltration may be affected by various DEM's spatial resolution.

5.2.1 Setting up the model simulations:

These simulations setup required generating data input files as follows:

- *DEM floodplain*: Digital Elevation Model (DEM) MERIT was used as an input floodplain topography for LISFLOOD-FP-vGA. The MERIT DEM data was processed by the mean resampling method in Arcmap to produce the of 171m and 257m spatial resolution as shown in Figure Figure 5.2.1. The topography of Wadi Al Batin varies from 293m in the valley downstream area to rises to reach the maximum elevation of 418m on the valley upstream area, which is presented by the DEM of 171m and 257m spatial resolution shown in Figure

5.2.1. The 171m DEM gives 117,342 cells in the LISFLOOD-FP-vGA model, while the 257m DEM gives 52,152 cells.

An additional DEM product, FABDEM produced by Laurence Hawker,Jeffrey Neal (2021), was used as an input floodplain topography for LISFLOOD-FP-vGA. FABDEM (Forest And Buildings removed Copernicus DEM). This DEM is a processed version where the tree height and building biases of Copernicus GLO 30 Digital Elevation Model (DEM) have been removed. FABDEM has an approximate 30 m cell size. It was resampled by the mean resampling method on Arcmap to produce the DEMs of 60m and 90m spatial resolutions as shown in Figure 5.2.2. FAB DEM 30m, FAB DEM 60m, and FAB DEM 90m gives 4,687,320 cells, 962,927 cells, and 427,328 cells respectively in the LISFLOOD-FP-vGA model.

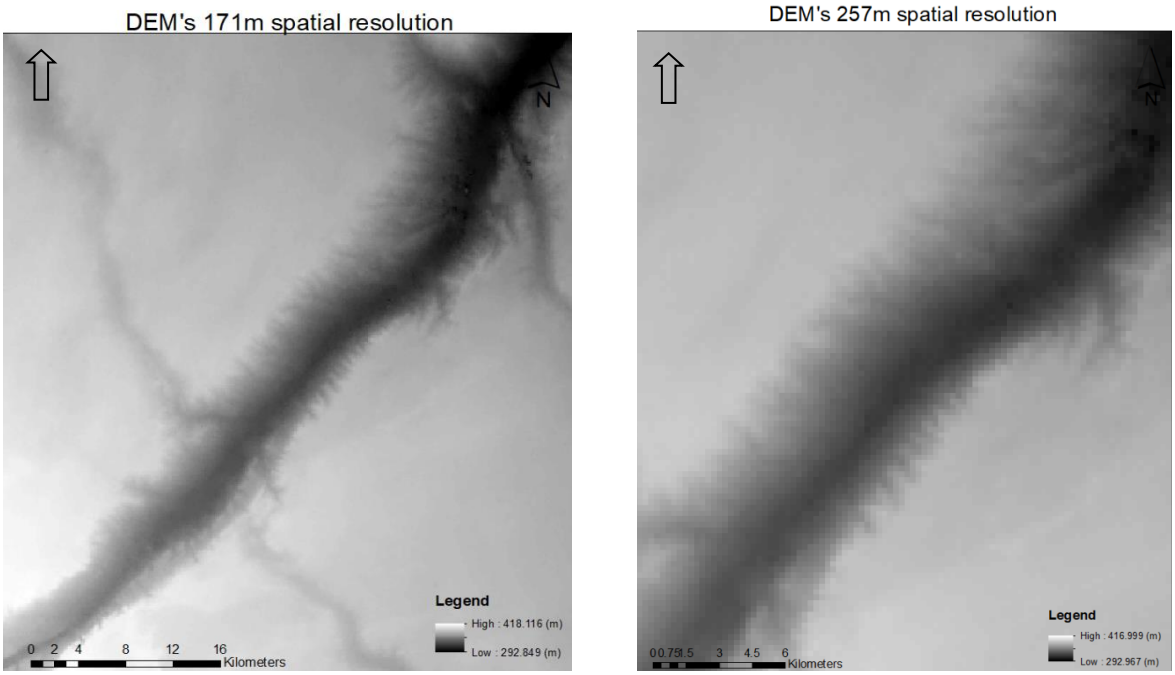

Figure 5.2.1.Digital Elevation model MERIT at 171m and 257m spatial resolution.

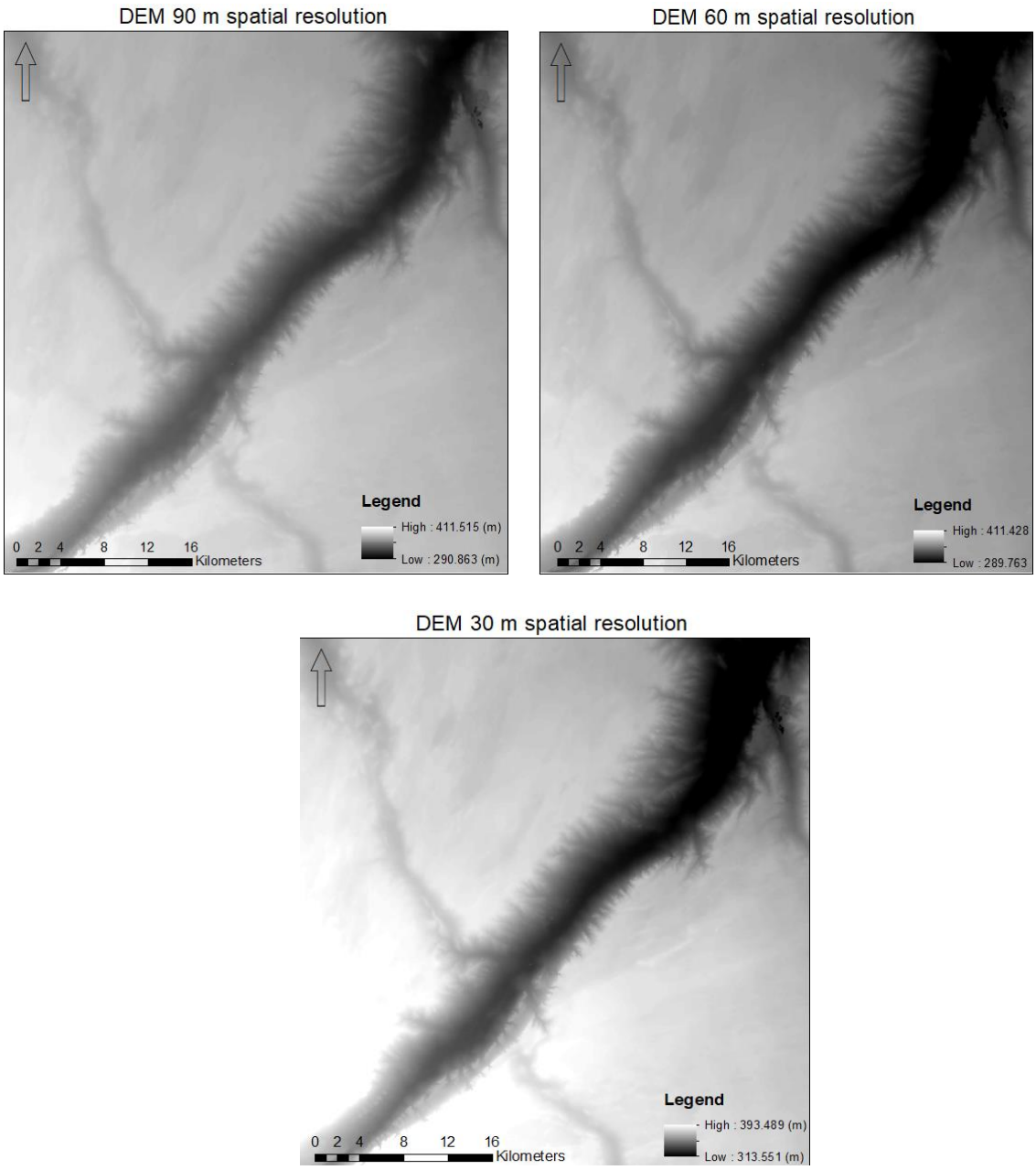

Figure 5.2.2.Digital Elevation model FABDEM at 30m, 60m and 90m spatial resolution.

- *Boundary condition data*: the boundary conditions (for the .bci file) for the two model domains of 171m and 257m resolution are shown in Table 5.2.1 and Table 5.2.2. The boundary condition data for the 30m, 60m, and 90m FAB DEM spatial resolution models are shown in Table 5.2.2Table 5.2.4 and Table 5.2.2

Table 5.2.1.The boundary conditions of 171m DEM spatial resolution model.

Upstream boundary		**Downstream boundary**			
N (m)	N (m)	E (m)	E (m)	QFIX (m^3s^{-1})	Slope
3099067	550861	3158483	601828	0.582231	0.0006

Table 5.2.2.The boundary conditions of 257m DEM's spatial resolution model.

Upstream boundary		**Downstream boundary**			
N (m)	N (m)	E (m)	E (m)	QFIX (m^3s^{-1})	Slope
3099067	550861	3158483	601828	0.388154	0.0006

Table 5.2.3.The boundary conditions of 30m DEM spatial resolution model.

Upstream boundary		**Downstream boundary**			
N (m)	N (m)	E (m)	E (m)	QVAR (m^3s^{-1})	Slope
3099067	550861	3158483	601828	.QVAR	0.0006

Table 5.2.4.The boundary conditions of 60m DEM spatial resolution model.

Upstream boundary		**Downstream boundary**			
N (m)	N (m)	E (m)	E (m)	QVAR (m^3s^{-1})	Slope
3099067	550861	3158483	601828	QVAR	0.0006

Table 5.2.5.The boundary conditions of 90m DEM spatial resolution model.

Upstream boundary		**Downstream boundary**			
N (m)	N (m)	E (m)	E (m)	QVAR (m^3s^{-1})	Slope
3099067	550861	3158483	601828	QVAR	0.0006

QFIX is the constant discharge inflow into the domain which simulates the steady state flow at the model's upstream boundary and is considered as mass flux per unit width in m^3s^{-1}. The QFIX value is associated with the constant inflow discharge at the model upstream boundary. QFIX is multiplied within LISFLOOD-FP-vGA code by the length of boundary segment.

Therefore, the constant volume inflow into the 171m and 257m spatial resolution model's upstream of 200 m^3/s.

QVAR is the time varying flow magnitude and corresponds to the data within the *.bdy file. The QVAR boundary is given as mass flux per unit width. This is multiplied within LISFLOOD-FP-vGA code by the length of the boundary segment to give the discharge mass flux of m^3s^{-1}.

The .bdy file consists of time varying boundary conditions associated with the boundary segment specified in the Table 5.2.4 and Table 5.2.5. Therefore, a time varying flow with a peak flow of 1500 m^3/s was applied with the 30m, 60m and 90m spatial resolution models, as shown in Figure 5.2.3.

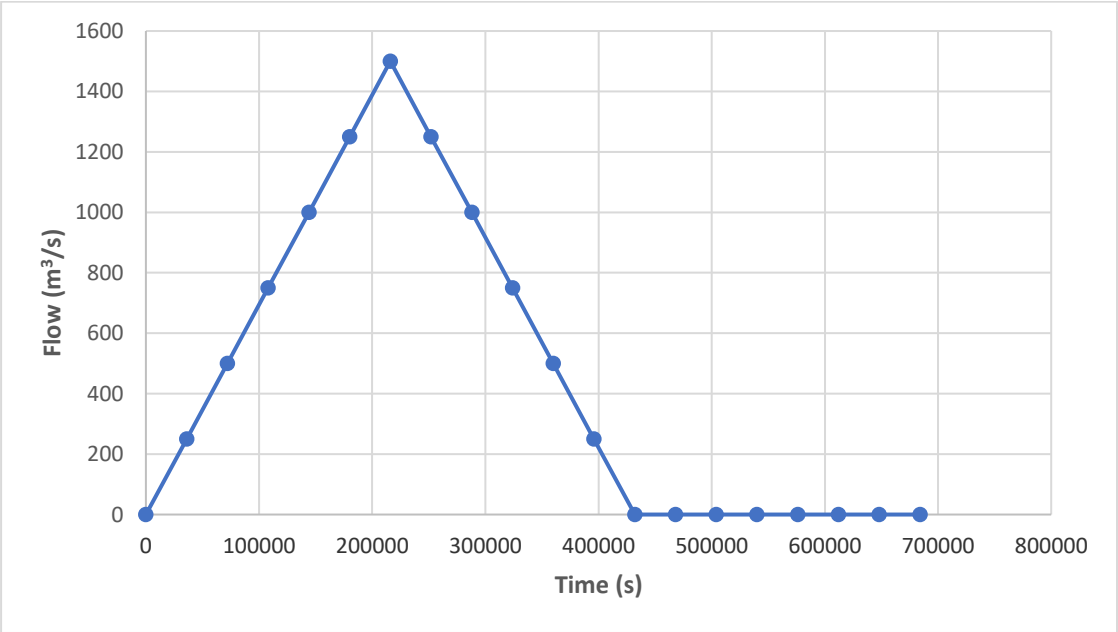

Figure 5.2.3.Time varying flow hydrograph magnitude used as a model inflow.

Furthermore, the slope of 0.0006 is defined as the overall Al Batin valley slope. Therefore, LISFLOOD-FP-vGA uses the user determined slope to calculate the normal depth for the downstream water level. N and E are the northing and easing defined in the UTM coordinate system.

- *The model input parameters*: generating the model input parameters files (referred to as the "par" file, or the ".par" file). The model simulation time has been defined in the *.par file as 8 days (691200 seconds), the initial time step has been defined as 100 seconds, while the save interval for results has been defined as 3600 seconds.

  The Manning's n value for floodplain over the entire domain was defined within the *.par files for both models as 0.06 used for 171m and 257m DEM spatial resolution models. This

Manning's n value considered as a standard value estimate representing the type of the floodplain within Al Batin catchment.

Furthermore, wider range of Manning's coefficient of 0.03, 0.04, 0.05 and 0.06 has applied into 30m, 60m, 90m DEM spatial resolution models as a part of the sensitivity analysis.

The LISFLOOD-FP-vGA implementation has allowed the infiltration rate to be added as a model input and with this specified in the *.par files either as a constant infiltration all over the floodplain model domain, or as a variable Green-Ampt spatially distributed infiltration loss distributed variably over the floodplain. As explained earlier in this chapter, the model simulations run using this approach allow various infiltration scenarios such as constant infiltration rate, spatial Green-Ampt infiltration, and no infiltration loss.

A constant infiltration rate of 1.6×10^{-6} m/s has been applied to the 171m and 257m resolution models. This value has been chosen to apply a minimum amount of constant infiltration and it is compared later in this chapter with spatial Green-Ampt infiltration applied to the model.

A constant infiltration rate of 7.778×10^{-6}m/s (2.8 cm/h) has been chosen and applied to the 30m, 60m and 90m DEM spatial resolution models. This was based on the experiment carried out by Helali (1993). A double ring infiltrometer was used in this experiment within 50 surface soils of three different texture classes. Helali (1993) has stated that the infiltration rate of the loam soils texture class, which is the dominant soil texture within Al Batin River catchment, ranges from 2.8 cm/h to 6 cm/h. Therefore, a minimum of that range, 2.8 cm/h, has been used to apply a constant infiltration to model simulation.

The spatially distributed variable Green-Ampt infiltration applied over the floodplain model domain through the generating of an infiltration map file (in ASCII format) referenced from within the *.par file and in conjunction with the parameters enable soil data relevant to Green-Ampt to be distributed. This map file must have the same dimensions and spatial resolution as the digital elevation model.

The soil data for the Wadi Al Batin catchment was retrieved from the FAO soil map (The Digital Soil Map of the World Food and Agriculture Organization of The United Nations Version 3.6, completed January 2003). The three soil texture classes in Wadi Al Batin catchment are silt loam, loamy sand and sandy loam.

The Green-Ampt parameters used as an input for LISFLOOD-FP-vGA developed by Rawls et al. (1983) based on the soil texture classes, are shown in Table 5.2.6.

Table 5.2.6: Green-Ampt parameters developed by Rawls et al. (1983)

Soil texture class	Residual porosity	Effective porosity	Suction head (cm)	Hydraulic conductivity (cm/h)
Clay loam	0.155	0.309	20.88	0.1
Silt loam	0.015	0.486	16.68	0.65
Sandy loam	0.041	0.412	11.01	1.09

5.3 Results

5.3.1 171m and 257m DEM spatial resolution model run simulations:

This section consists of discussing the implications of the infiltration loss at multiple DEM spatial resolution models of 171m and 257m on flood wave progression characteristics for the three infiltration loss scenarios. Green-Ampt infiltration, constant infiltration and no infiltration. Considering the flow travel time, results are shown in Figure 5.3.3 and Table 5.3.1 for the 171m and 257m DEM spatial resolution. These three infiltration scenarios show a longer flow travel time with the finer, 171m DEM. With a 12.75 hours, 15.0 hours and 10.75 hours increase between the two model resolutions for Green-Ampt infiltration, constant infiltration, and no infiltration respectively.

When implementing a Green-Ampt variable spatial infiltration and having a bigger DEM cell, the surface roughness that unrepresented surface features or vegetation plays a significant role. Therefore, higher surface roughness causes a longer flow travel time, while conversely a lower surface roughness causes a shorter flow travel time.

Furthermore, it shows even a longer flow travel time difference of 15 hours when implementing the constant infiltration and comparing the DEM spatial resolution models of 171m and 257m due to higher volume of the amount of water infiltrated as shown in the Figure 5.3.1 and Figure 5.3.2

These figures show, during the simulation runs of 171m and 257m DEM spatial resolution models, 138,240,000 m^3 entered the flow domain, therefore for the Green-Ampt infiltration simulation run 17.9 % was infiltrated and for constant infiltration 33.6 % was infiltrated for 171 m DEM spatial resolution model. However, 18.3 % was infiltrated and for constant infiltration 36.1 % was infiltrated for 257 m DEM spatial resolution model.

The above leads to less volume of water reaching the end of the domain simulation run and longer travel time. This also means that a consequence of the higher cell size is bigger when implementing the constant infiltration loss scenario in comparison with Green-Ampt infiltration loss scenario.

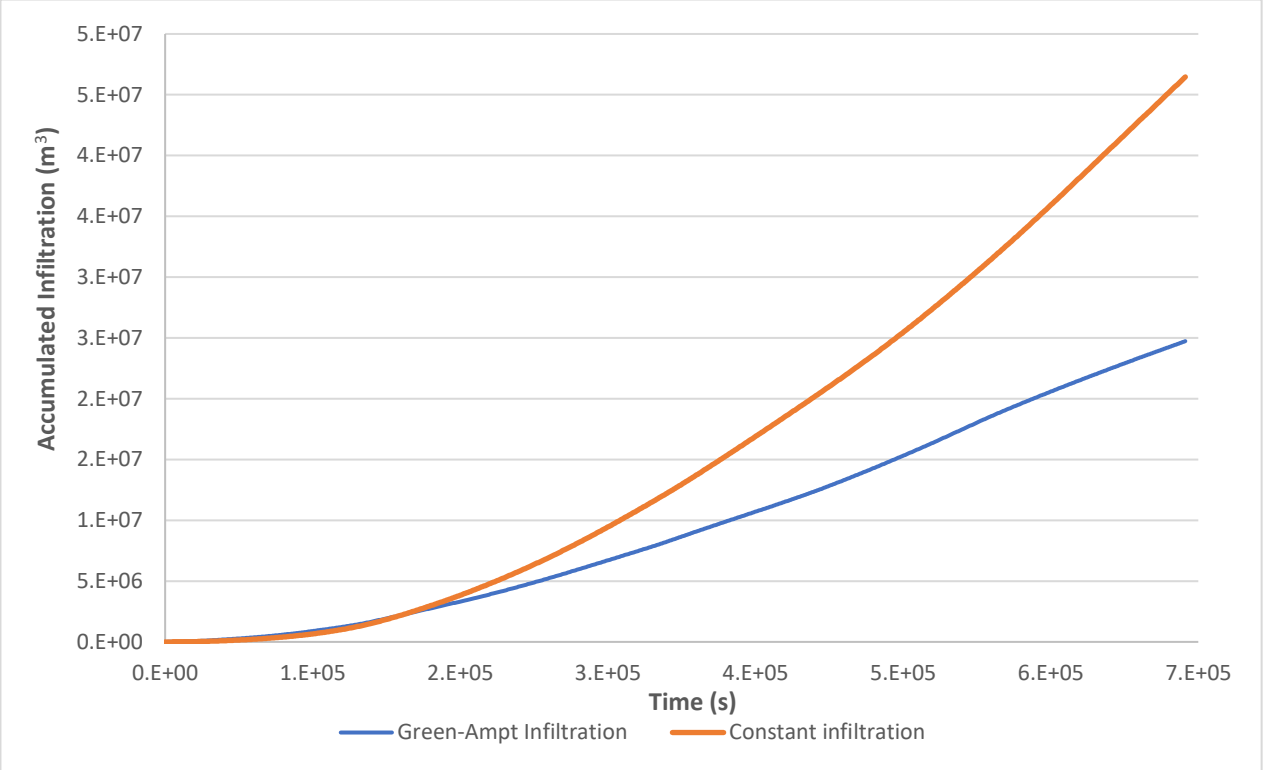

Figure 5.3.1 accumulated infiltration loss comparison between the two scenarios where a constant infiltration and Green-Ampt infiltration applied to the simulation model of 171m DEM spatial resolution.

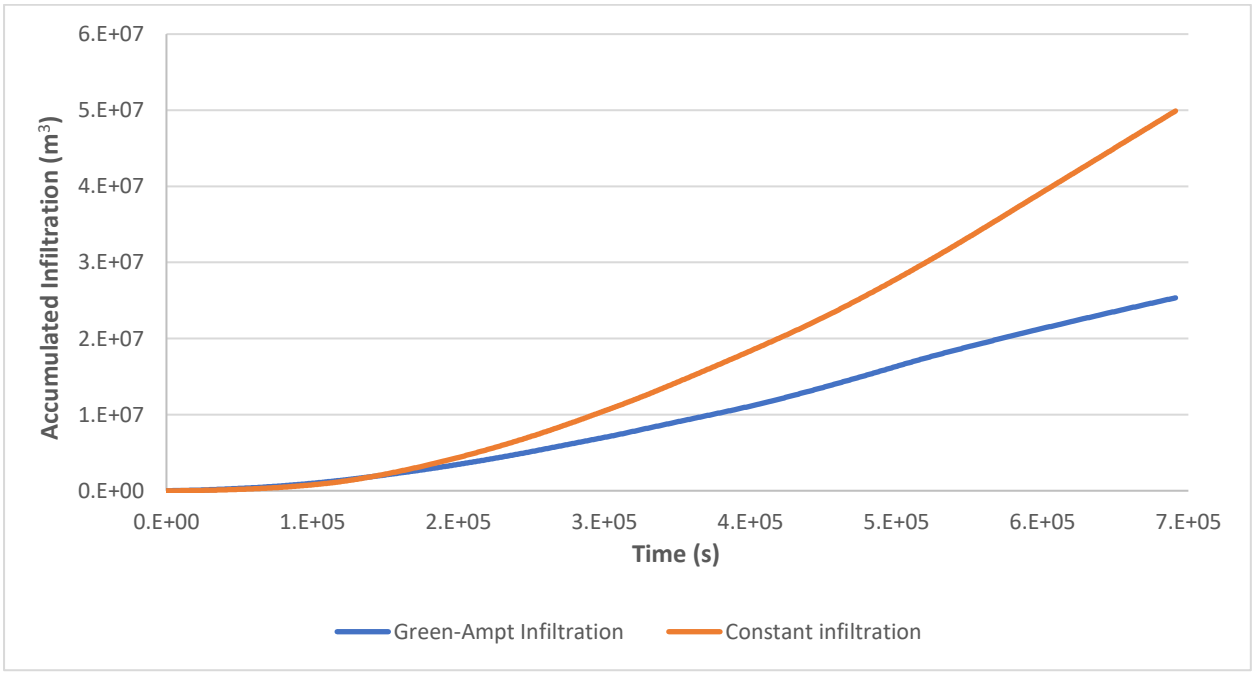

Figure 5.3.2 accumulated infiltration loss comparison between the two scenarios where a constant infiltration and Green-Ampt infiltration applied to the simulation model of 257m DEM spatial resolution.

At the same time, it also shows a shorter travel time, with the difference being 10.75 hours with no infiltration, which means that the implications on the flow travel time are related only to the size of the DEM, therefore there is no infiltrated water in the floodplain simulation domain. Thus, this is consistent with the simulated travel time pattern found in Chapter 3. Moreover, this could be explained that the flow travel time difference when having a coarser DEM is linked to the resampling process which might causes an underestimate of the micro-topographic flow paths. Therefore, it leads to quicker simulated travel time.

Table 5.3.1 two models DEM spatial resolutions of 171m and 257m simulations comparison and the implications on the flow travel time.

DEM (m)	Travel time Spatial GA Infiltration (h)	Travel time Constant Infiltration (h)	Travel time no infiltration (h)
171	151.50	168.00	132.75
257	138.75	153.00	122.00

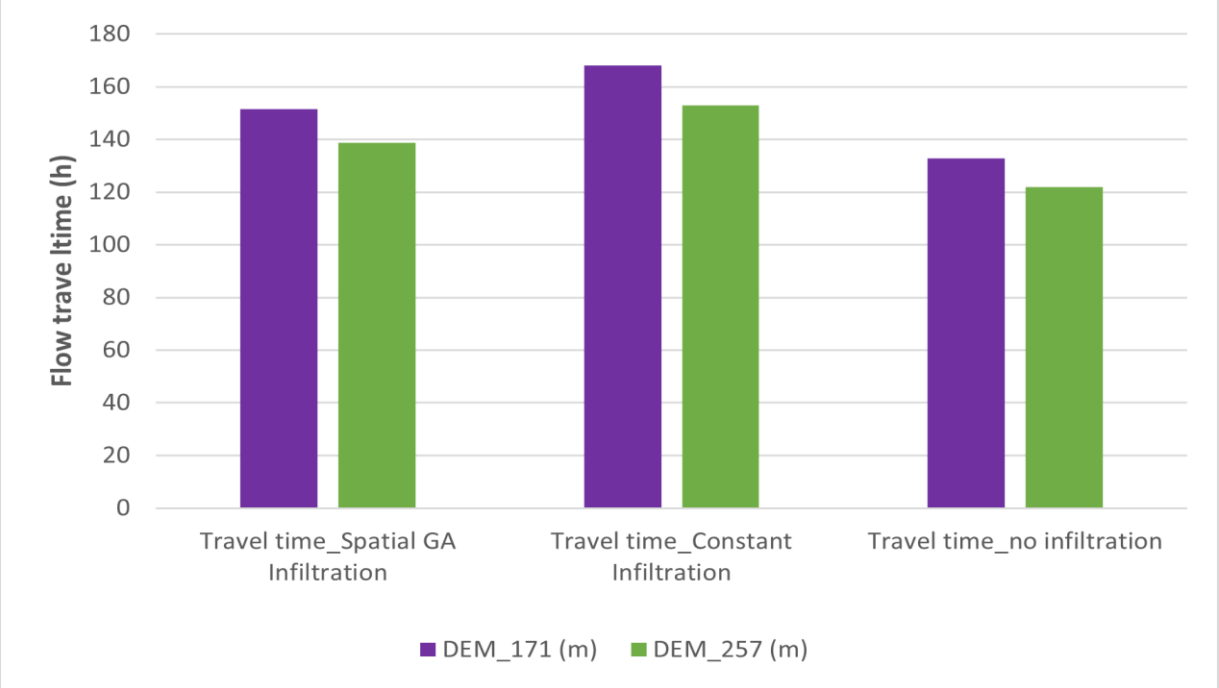

Figure 5.3.3 models DEM spatial resolution of 171m and 257m simulations comparison and the implications on the flow travel time.

The comparison of results of the two spatial resolutions of flooded area are shown in

Table 5.3.2 and Figure 5.3.4. The results show for each of DEM spatial resolution model, a decrease in the flooded area when applying a constant infiltration loss and Green-Ampt infiltration, in comparison with the flooded area when no infiltration applied to the model. Furthermore, the flooded area is greater when applying Green-Ampt infiltration compared to the flooded area when applying a constant infiltration loss.

This could be explained because of the volumes of water infiltrated vary when applying the various infiltration scenarios as explained earlier and shown in the Figure 5.3.1 and Figure 5.3.2.

Figure 5.3.1 shows that the volume of water infiltrated at the end of the simulation is approximately 46% less when applying Green-Ampt infiltration. Furthermore, 5.3.2 shows that water volume infiltrated is approximately 49%.

For each of the finer DEM simulations the flooded area is reduced with 1.74 km^2, 0.65 km^2 and 1.67 km^2 less for Green-Ampt infiltration, constant infiltration, and no infiltration respectively. As explained in Chapter 3, it is in relation to the increase in the water level because of increasing the channel bed level due to features smoothing as a result from the resampling process. Therefore, greater inundated area, as found by Saksena and Merwade (2015) hence, as suggested earlier in Chapter 3 higher spatial resolution, may lead to a better estimation of the flooded area.

Table 5.3.2: The two models DEM spatial resolutions of 171m and 257m simulations comparison and the implications on the flooded area.

DEM (m)	**Flooded area - Spatial GA Infiltration (Km^2)**	**Flooded area - Constant Infiltration (Km^2)**	**Flooded area - no Infiltration (Km^2)**
171	73.92	71.03	76.25
257	75.66	71.68	77.92

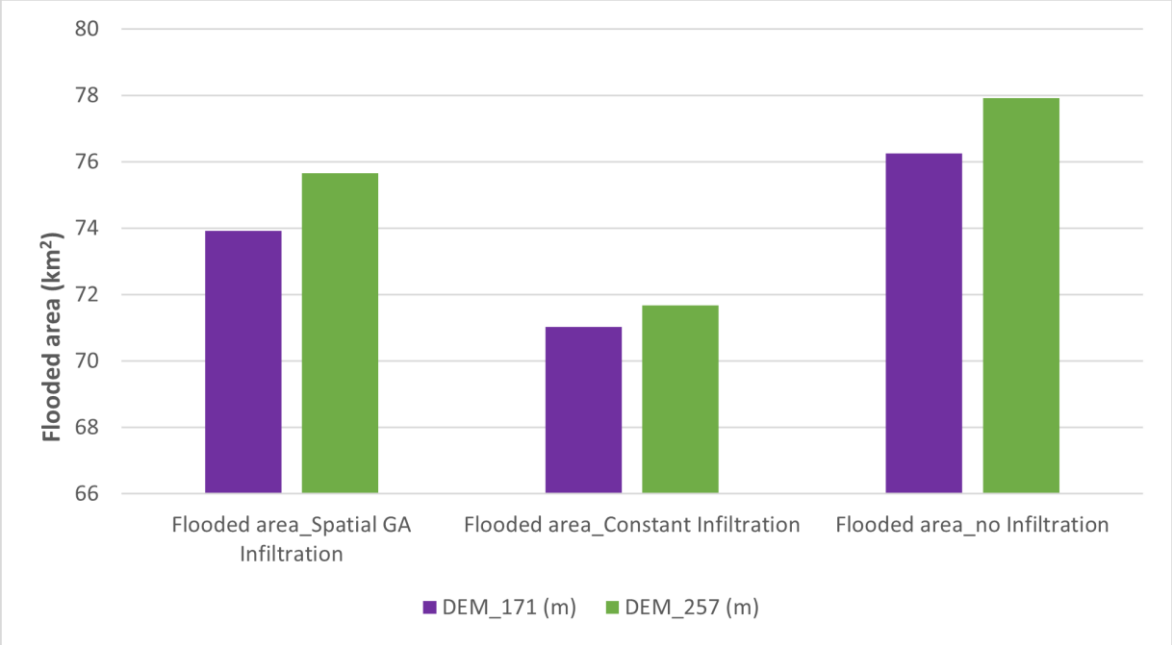

Figure 5.3.4 two models DEM spatial resolutions of 171m and 257m simulations comparison and the implications on the flooded area.

The comparison of results of the two spatial resolutions for water volume infiltrated are shown in Figure *5.3.5* and Table 5.3.3. It is found for each of the finer DEM simulations the water volume is increased when the 171m DEM is used, with 0.008 km^3, 0.007 km^3 and 0.008 km^3 more for Green-Ampt infiltration, constant infiltration, and no infiltration respectively. This might be explained by considering that the flooded area is decreasing with the finer DEM, therefore the water volume left in the model is increasing with the finer DEM.

Table 5.3.3.The models DEM spatial resolution of 171m and 257m simulations comparison and the implications on the water volume.

DEM (m)	Water volume- Spatial GA Infiltration (Km^3)	Water volume - Constant Infiltration (Km^3)	Water volume - no Infiltration (Km^3)
171	0.091	0.084	0.095
257	0.083	0.077	0.087

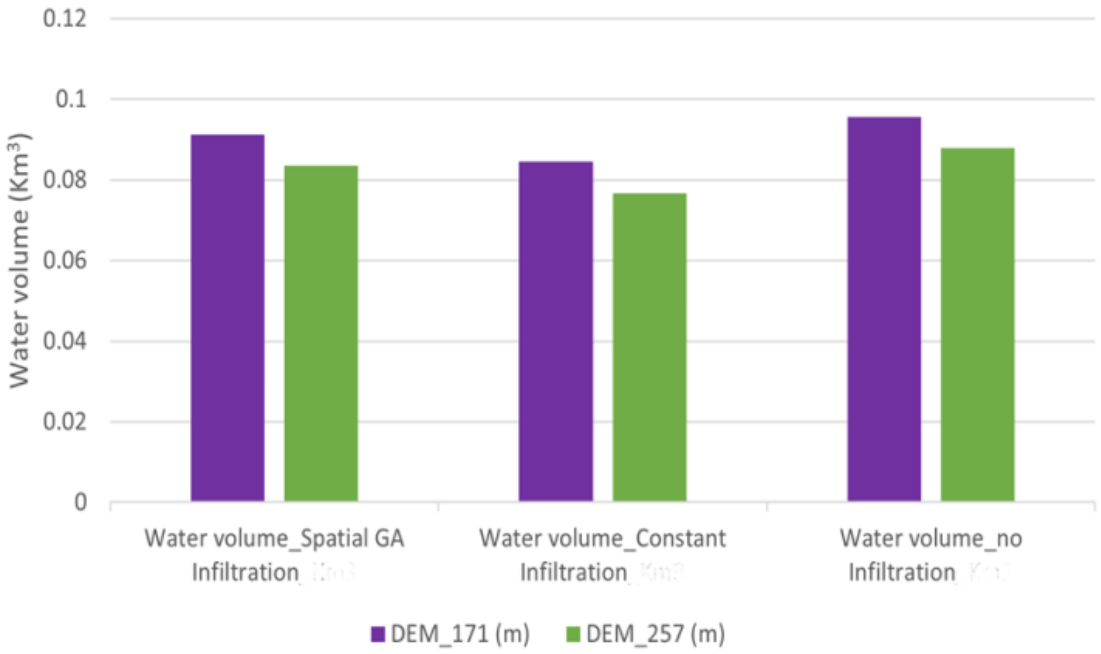

Figure 5.3.5 models DEM spatial resolution of 171m and 257m simulations comparison and the implications on the water volume.

5.3.2 30m, 60m and 90m FAB DEM spatial resolution model run simulations:

In order to investigate how a different DEM might affect the model simulations by LISFLOOD-FP-vGA with including Green-Ampt infiltration loss, additional simulation runs were carried out with the FAB DEM at resolutions of 30m, 60m and 90m.

The new FAB DEM was implemented for models with all three infiltration scenarios described and modelled above. These will enable establishment of the implications of the various infiltration loss scenarios on the flood wave propagation characteristics by using multiple DEM spatial resolution. The constant infiltration value of 7.778 $x10^{-6}$m/s (2.8 cm/h) used as explained earlier in section 5.2.1. Moreover, the varying flow hydrograph with a peak magnitude flow of 1500 m^3/s was used as a model inflow as shown earlier in the Figure 5.2.3 in the section 5.2.1.

Also, the Manning's floodplain coefficient values of 0.03, 0.04, 0.05 and 0.06 have been applied to each model of 30 m DEM spatial resolution model, 60 m DEM spatial resolution model and 90 m DEM spatial resolution model.

Figure 5.3.6, Figure 5.3.7 and Figure 5.3.8. Table 5.3.4, Table 5.3.5, and Table 5.3.6 show the comparison of flood wave travel time, the flooded area, and the water volume simulations of the three infiltration scenario applied to the model simulation at DEM spatial resolution of 30m.

Figure 5.3.6 and Table 5.3.4 show flow travel time difference of 5.75 hours, 6.5 hours, 7 hours, and 7.5 hours by applying the Green-Ampt spatial infiltration and applying the constant infiltration shows the flood wave travel time is shorter when applying Green-Ampt spatial infiltration.

This shorter travel time is because of the amount of water infiltrated from the water volume added to the model during the simulation run is less than the amount of water infiltrated from the water volume added to the model during the simulation run when applying the constant infiltration, therefore shorter flow travel time to reach the end of the domain simulation.

Moreover, Figure 5.3.6 shows increasing flow travel time of 5.5 hours, 10.5 hours, and 15 hours when applying Green-Ampt spatial infiltration, along with increasing the Manning's coefficient from 0.03 to 0.04, 0.05, and 0.06 respectively.

Also, it shows along with increasing the Manning's coefficient from 0.03 to 0.04, 0.05, and 0.06 an increase in the flow travel time of 6.25 hours, 11.75 hours, and 16.75 hours respectively when applying constant infiltration within the simulation domain.

Lastly, Figure 5.3.6 shows an increase as well in the flow travel time of 5.5 hours, 10.25 hours, and 14.75 hours when applying no infiltration, along with increasing the Manning's coefficient from 0.03 to 0.04, 0.05, and 0.06 respectively.

This increase in the flow travel time along with increasing the Manning's coefficient, could be the reason for the flow resistance implications. Therefore, higher flow Manning's coefficient causes more flow obstacles and slower flow travel time.

This flow travel time variation between the three infiltration scenarios, at DEM spatial resolution of 30m model with the varying flow hydrograph, and various Manning's coefficient shows again that the infiltration loss is significant to achieve robust flood risk assessment in the ephemeral system.

Table 5.3.4 comparison of flow travel time at three different scenarios of no infiltration, constant infiltration and Green-Ampt spatial infiltration simulation models on 30m DEM spatial resolution.

:

DEM 30m model			
Manning's Coefficient	**Travel time- Spatial GA Infiltration (h)**	**Travel time - Constant Infiltration (h)**	**Travel time - no infiltration (h)**
0.03	45.25	51	43.75
0.04	50.75	57.25	49.25
0.05	55.75	62.75	54
0.06	60.25	67.75	58.5

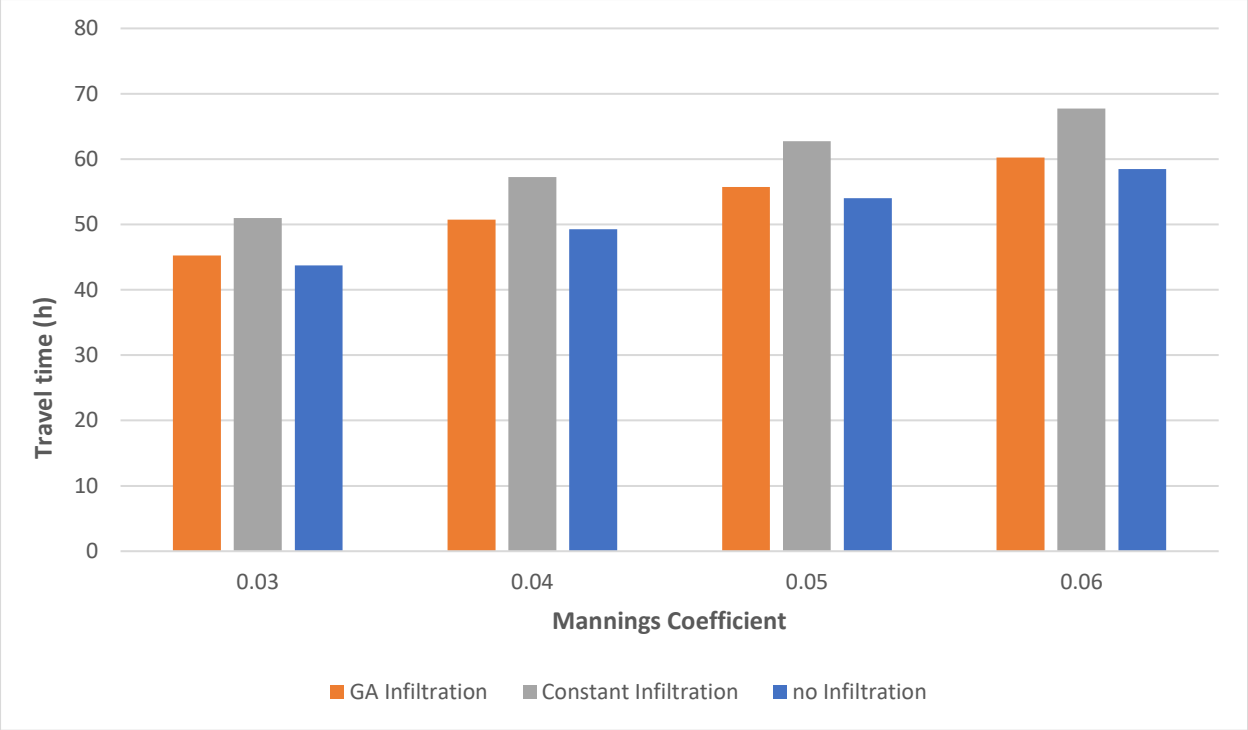

Figure 5.3.6 comparison of flow travel time at three different scenarios of no infiltration, constant infiltration and Green-Ampt spatial infiltration simulation models on 30m DEM spatial resolution.

Figure 5.3.7 and Table 5.3.5 show the implications of three infiltration scenarios on the simulated flooded area using 30m DEM. Figure 5.3.7 and Table 5.3.5 show the flooded area difference of 2.8 km^2 , 2.5 km^2 , 2.7 km^2 , and 3.367 km^2 between the Green-Ampt spatial infiltration scenario and the constant infiltration scenario. This difference may be explained by the amount of water infiltrated from the water being less in the Green-Ampt than that infiltrated with the constant infiltration.

Moreover, Figure 5.3.7 and Table 5.3.5 show increasing flooded area of 5.91 km^2, 11.1 km^2, and 15.47 km^2 when applying Green-Ampt spatial infiltration, along with increasing the Manning's coefficient from 0.03 to 0.04, 0.05, and 0.06 respectively.

Also, it shows along with increasing the Manning's coefficient from 0.03 to 0.04, 0.05, and 0.06 an increase in the flooded area of 6.14 km^2, 11.13 km^2, and 14.92 km^2 respectively when applying constant infiltration within the simulation domain.

Lastly, FigureFigure 5.3.7 and Table 5.3.5 show as well an increase in the flooded area of 6.25 km^2, 11.14 km^2, and 15.74 km^2 when applying no infiltration, along with increasing the Manning's coefficient from 0.03 to 0.04, 0.05, and 0.06 respectively.

This increase in the inundated area along with increasing the Manning's coefficient, could be the reason of flow resistance implications. Therefore, causes a higher water level which leads to greater flooded area.

Moreover, the significant flooded area difference between the three various infiltration scenarios at DEM spatial resolution of 30m model along with varying flow magnitude hydrograph, and various Manning's coefficient, indicates what is discussed earlier in the Chapter 5 that the infiltration loss plays a significant role for more robust flood risk assessment in the ephemeral system.

Table 5.3.5 comparison of flooded area at three different scenarios of no infiltration, constant infiltration and Green-Ampt spatial infiltration simulation models on 30m DEM spatial resolution.

DEM 30m model			
Manning's Coefficient	**Flooded area - Spatial GA Infiltration (Km^2)**	**Flooded area - Constant Infiltration (Km^2)**	**Flooded area - no Infiltration (Km^2)**
0.03	75.25	72.44	75.45
0.04	81.16	78.58	81.7
0.05	86.35	83.57	86.59
0.06	90.72	87.36	91.19

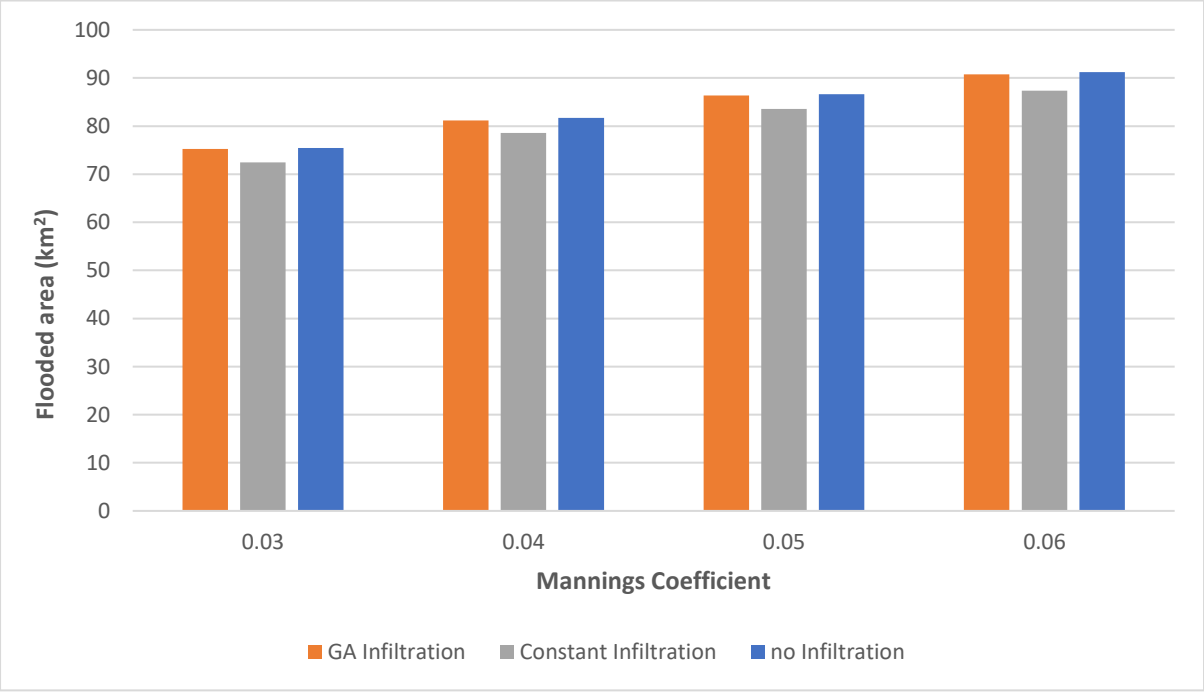

Figure 5.3.7 comparison of flooded area at three different scenarios of no infiltration, constant infiltration and Green-Ampt spatial infiltration simulation models on 30m DEM spatial resolution.

Figure 5.3.8 and Table 5.3.6 show the implications of three infiltration scenarios on the simulated water volume using 30m DEM. Figure 5.3.8 and Table 5.3.6 show water volume difference of 0.006

km^3, 0.007 km^3, and 0.009 km^3 between the Green-Ampt spatial infiltration scenario and the constant infiltration scenario.

As concluded earlier in the chapter 5, this water volume difference between the three infiltration scenarios can be accounted for by the amount of water infiltrated being different for each simulation infiltration scenario which leading to directly different water volumes left in the channel.

Again, it may be concluded from these simulations that there is significant water volume difference then it is vital to model infiltration loss with care to ensure more robust flood risk assessment.

Table 5.3.6 comparison of water volume at three different scenarios of no infiltration, constant infiltration and Green-Ampt spatial infiltration simulation models on 30m DEM spatial resolution.

DEM 30m model			
Manning's Coefficient	**Water volume - Spatial GA Infiltration (Km^3)**	**Water volume - Constant Infiltration (Km^3)**	**Water volume - no Infiltration (Km^3)**
0.03	0.085	0.079	0.086
0.04	0.108	0.100	0.109
0.05	0.130	0.121	0.131
0.06	0.153	0.137	0.153

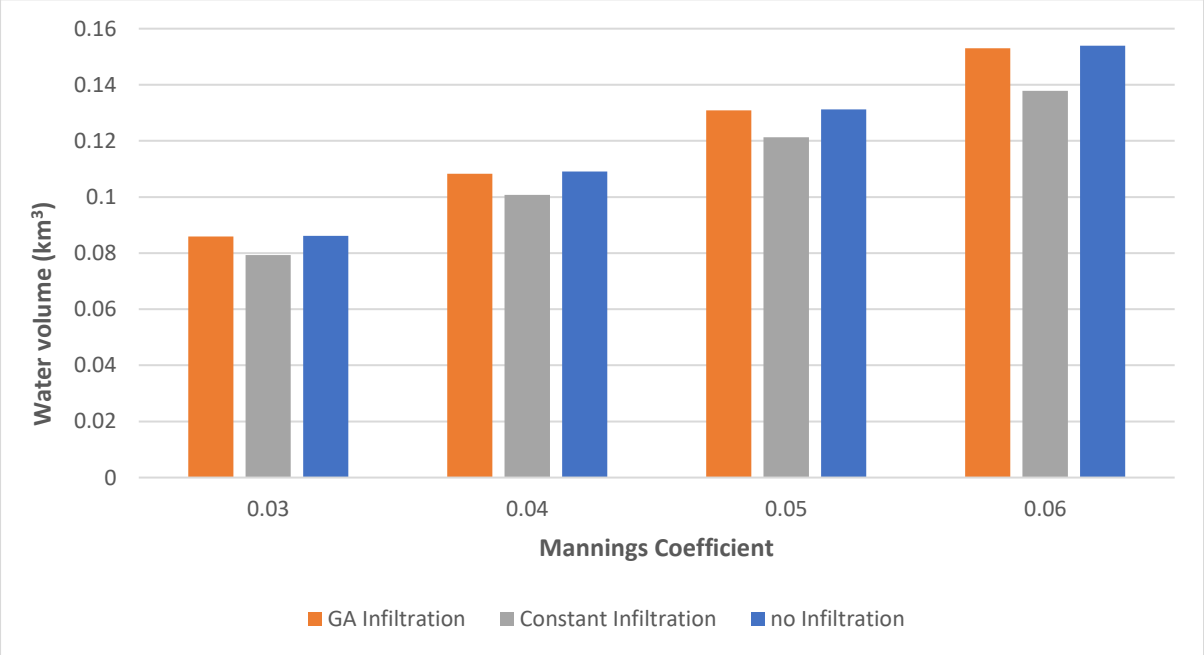

Figure 5.3.8 comparison of water volume at three different scenarios of no infiltration, constant infiltration and Green-Ampt spatial infiltration simulation models on 30m DEM spatial resolution.

5.3.3 The comparison between the 30m, 60m and 90m DEM spatial resolution model run simulations:

This section consists of comparing and discussing the implications of the DEM spatial resolutions of 30m, 60m and 90m on flood wave progression characteristics for the three infiltration loss scenarios at Manning's coefficient of 0.04.

Considering the flow travel time simulated results as shown in Figure 5.3.9 and Table 5.3.7 for the 30m, 60m and 90m DEM spatial resolution. These three infiltration scenarios show a longer flow travel time with the course, 60 m and 90m DEM. For the 60m DEM spatial resolution model, the flow travel time increases of 0.75 hour, 0.75 hour and 0.5 hour, for Green-Ampt infiltration, constant infiltration, and no infiltration respectively. Moreover, for the 90m DEM spatial resolution model, the flow travel time increase of 1.5 hours, 1.75 hours and 1.25 hours, when applying Green-Ampt infiltration, constant infiltration, and no infiltration respectively.

This might be explained by the finer resolution DEM presents more detailed topographic features and flow paths. Therefore, the flow takes longer time with higher DEM cell size in comparison with the lower cell size.

Table 5.3.7 DEM spatial resolution models of 30m, 60m and 90m comparison and the implications on the flow travel time.

DEM (m)	Travel time - Spatial GA Infiltration (h)	Travel time - Constant Infiltration (h)	Travel time - no infiltration (h)
30	50.75	57.25	49.25
60	51.50	58.00	49.75
90	52.25	59.00	50.50

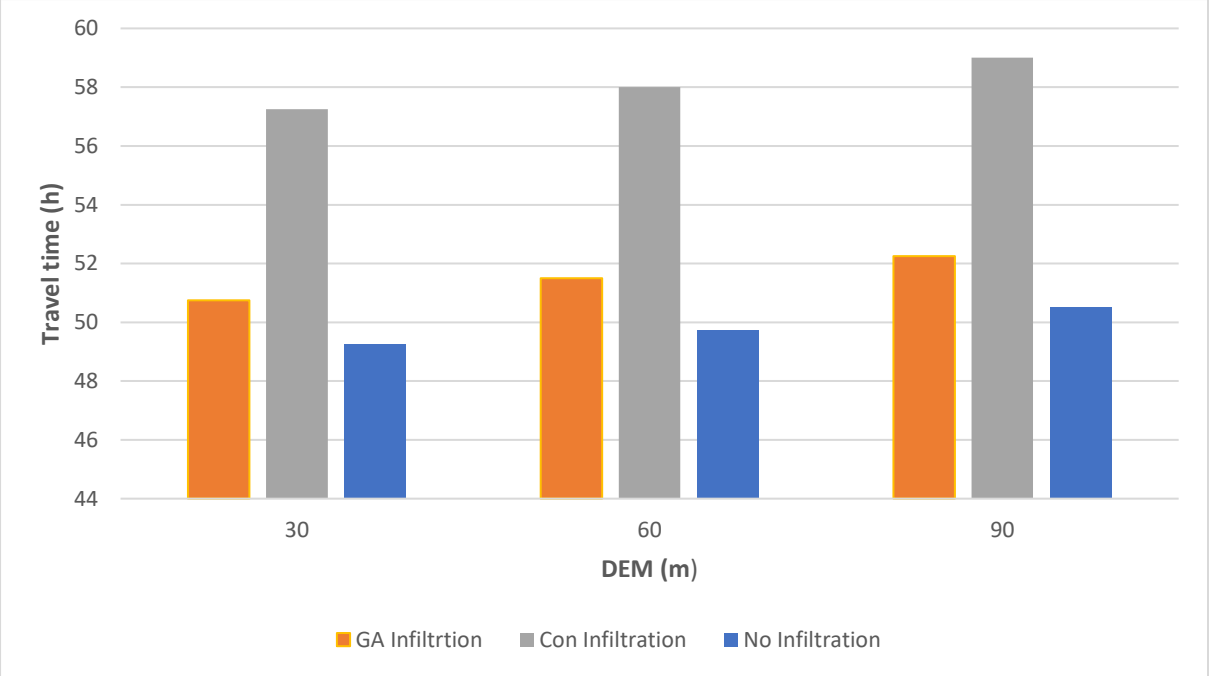

Figure 5.3.9 DEM spatial resolution models of 30m, 60m and 90m comparison and the implications on the flow travel time.

The comparison of the flooded area results between the three DEM spatial resolution models of 30m, 60m and 90m are shown in Figure 5.3.10 and Table 5.3.8. For each of the DEM simulations the flooded area is reduced when the finer 60m DEM is used, with 1.3 km^2, 0.93 km^2 and 0.83 km^2 less for Green-Ampt infiltration, constant infiltration, and no infiltration respectively. Moreover, for the 30m DEM the flooded area is reduced with 2.38 km^2, 2.12 km^2 and 1.97 km^2 less for Green-Ampt infiltration, constant infiltration, and no infiltration respectively.

The increase of the flooded area when using coarser DEM resolution, is related to the bed elevation increase as a result of the smoothing due to the DEM resampling, as found by Saksena and Merwade (2015). Therefore, higher water level which leads to greater inundated area.

Lastly, the increase in flooded area along with the increasing the DEM cells size, leads to over prediction of the simulated flooded area. This indicates again what was seen in Chapter 3 that finer DEM spatial resolution, leads to better estimation of the simulated flow travel time, the flooded area, and the flow water volume. Therefore, this might lead to more robust flood risk assessment, prediction and developed resilience emergency measures from the local authorities.

Table 5.3.8 DEM spatial resolution models of 30m, 60m and 90m comparison and the implications on the flooded area.

DEM (m)	Flooded area Spatial GA Infiltration (Km^2)	Flooded area Constant Infiltration (Km^2)	Flooded area no Infiltration (Km^2)
30	81.70	81.16	78.58
60	82.53	82.46	79.51
90	83.67	83.54	80.70

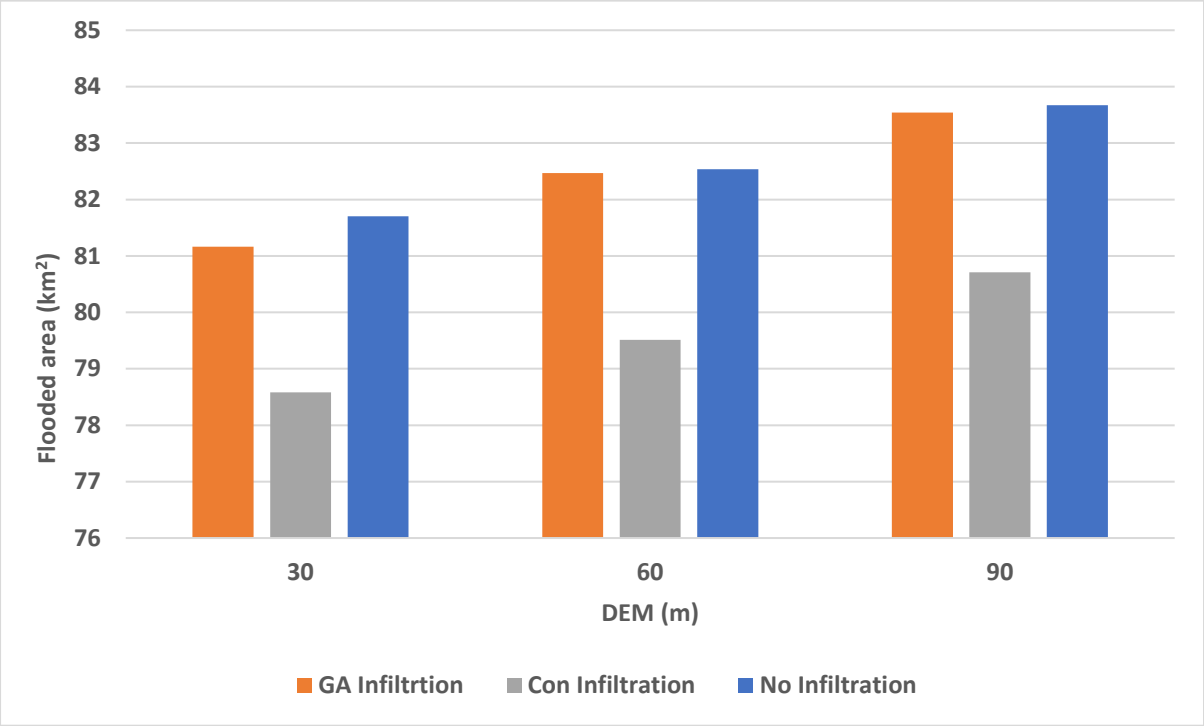

Figure 5.3.10. DEM spatial resolution models of 30m, 60m and 90m comparison and the implications on the flooded area.

5.4 Discussion

Following the results analysis presented in the previous section, further discussion is presented below.

The results show that the infiltration loss in the ephemeral channel in Wadi Al Batin slows the flow and gives more time for the infiltration process to occur. Therefore, there is less inundated area and longer flow travel time.

This is in line with what (Mudd 2006) found, when investigating the interaction between the flow in the ephemeral channel and the bed infiltration. (Mudd 2006) found that the infiltration loss plays an important role into the momentum balance in the ephemeral system.

Moreover, the results show applying Green-Ampt infiltration plays a crucial role in defining the implications of the infiltration loss on the wave propagation characteristics in the ephemeral channel in Wadi Al Batin. This is in relation to the amount of water volume infiltrated within the channel is less than in the Green-Ampt model when compared with the constant infiltration model as shown Figure 5.4.1 and Figure 5.4.1. Therefore, more water volume is left in the channel, which leads to shorter flow travel time to reach the end of the simulation domain.

This above discussion applies as well to the simulated flooded area, as the amount of infiltrated water volume is greater with the constant infiltration model compared to the Green-Ampt model. Meaning that less water volume remains in the model, which leads to lower simulated water depth. Therefore, there is less simulated inundated area in comparison with the simulated inundated area when applying variable Green-Ampt infiltration loss.

As a result of the above discussion, the simulated inundated area, and the travel time could be either underestimated, or overestimated in the ephemeral system, which could lead to an unreliable flood prediction system.

Furthermore, the results of various range of parameters applied, might give more credibility on the above discussion. This again show the significant implications of the infiltration loss on the wave propagation in Wadi Al Batin in the ephemeral channel. These parameters are the following:

- Range of Manning's coefficient of 0.03, 0.04, 0.05 and 0.06.
- Merit DEM of 171m, and 257m spatial resolution.
- FAB DEM of 30m, 60m, and 90m spatial resolution.
- Constant inflow hydrograph and variable magnitude inflow hydrograph.

Firstly, the results show an increase in the flow travel time and the flooded area along with increasing the Manning coefficient. This could be the cause of the flow resistance implications, which lead to slower travel time, higher water level, and greater flooded area.

Secondly, the results of comparing the implications of various DEM spatial resolutions of 30m, 60m, 90m, 171m, and 257m on flood wave progression, shows variation in the simulated flow travel time, greater flood extent, and decreased water volume in the model domain when applying coarser DEM's spatial resolution.

Increasing the flood inundated area and decreasing the water volume when applying a coarser DEM spatial resolution, might be related to the cell size and how differently various DEM cell size presents differently the topographical features.

This is because of DEM smoothing process as a result of the DEM resampling to coarser DEM resolution, therefore might cause and increase in the overall surface elevation. furthermore, this leads to higher water levels and greater flooded area as found by Saksena and Merwade (2015). Therefore, this leads to overestimation or underestimation the simulated flooded area and the water volume left in the model.

Regarding the simulated flow travel time, it shows shorter flow travel time when applied to the coarser Merit DEM of 171m, and 257m spatial resolution. On another hand, it shows slower travel time when applied coarser FAB DEM spatial resolution of 30m, 60m, and 90m.

This controversial simulated flow travel time results between these two DEM products spatial resolutions, might be related to the resampling process of the Merit DEM to a coarser spatial resolution of 171m and 257m. This might cause an underestimate of the microtopographic flow path. Therefore, it causes a shorter flow travel time as shown when comparing the flow travel time results between the two Merit DEM models of 171m and 257m spatial resolution.

However, a shorter simulated flow travel time is seen when applying a finer FAB DEM spatial resolution of 30m, 60m, and 90m. This could be explained as a longer flow path within the larger cell size, leads to slower simulated flow travel time. Moreover, these results explain the minimum influence of the resampling process on typographical features of finer resolution FAB DEM of 30m, 60m and 90m in comparing with Merit DEM of 171m and 257m spatial resolution.

In terms of the most important factor and it is greater implications on the wave propagation, Figure 5.3.9 and Table 5.3.7 show the effect of Green-Ampt infiltration on the travel time at 30, 60, and 90 m DEM is approximately by 11.3%. However, the impact of various DEM resolution from 30 to 90 m is approximately 2.9% when applying infiltration to the model simulation and 2.47% when no infiltration has applied to the simulation.

Therefore, it is found that the infiltration parameter has a greater implication on the travel time in comparing to the DEM resolution, Furthermore, it shows that the effect of the DEM becomes greater when incorporating the infiltration into the model simulation.

On another hand, Figure 5.3.10 and Table 5.3.8 show the effect of Green-Ampt infiltration on the flooded area at 30, 60, and 90 m resolution DEM is approximately by 0.66%, 0.085% and 0.155% respectively. However, the impact of various DEM resolution from 30 to 90 m is approximately 2.6%.

Therefore, the DEM resolution has greater implications on the simulated flooded area in comparison to the infiltration parameter.

The conclusions on the implications of the infiltration loss, applying Green-Ampt infiltration loss, and the impact of the DEM spatial resolution on the wave propagation within the ephemeral river system, will be outlined in the next section.

5.5 Conclusions

From the results and discussions presented in this chapter, it is concluded that the implication of the infiltration loss is significant for flood wave propagation characteristics such as the flow travel time, the flooded area, and the water volume in Wadi Al Batin ephemeral channel system.

Moreover, it is concluded that applying spatial Green-Ampt infiltration loss plays a crucial role in estimating the relation between the infiltration loss and the wave propagation characteristics. Therefore, it is vital to model channel infiltration loss with care to ensure more robust flood risk assessment in in Wadi Al Batin ephemeral channel.

Furthermore, the above conclusions applied when various simulation's parameters incorporated in the model. These parameters are the constant inflow, variable inflow magnitude hydrograph, multiple DEM products such as Merit DEM and FAB DEM, range of DEM spatial resolution of 30m, 60m, 90m, 171m and 257m, and range of Manning's coefficient of 0.03, 0.04, 0.05 and 0.06. Therefore, this gives more reability of the conclusions related to implications of spatial Green-Ampt infiltration loss.

Comparing the implications of various DEM spatial resolutions of 30m, 60m, 90m, 171m, and 257m on flood wave progression, it leads to either overestimating or underestimating the simulated wave propagation characteristics. Therefore, it is concluded that DEM spatial resolution has crucial and significant impact on inundation model in LISFLOOD-FP-vGA and flood risk.

Regarding the most important factor and has the greatest implications on the flood wave propagation, it is concluded that the infiltration parameter has a greater implication on the travel time in comparing to the DEM resolution. However, the DEM resolution has greater implications on the simulated flooded area in comparison to the infiltration parameter. In addition to the above discussions, the limitation of LISFLOOD-FP-vGA simulations on Wadi Al Batin and the findings from these simulations, could be related to no calibration or validations having been conducted. This is mainly due to the data scarcity such as flow data, water depth data from the river gauge stations on Wadi Al Batin, or rainfall stations within the catchment from the water authority in Saudi Arabia.

Moreover, LISFLOOD-FP-vGA simulations results' uncertainty are related to the models input parameters such as the constant infiltration, Green-Ampt infiltration parameters, inflow hydrographs.

These simulations results could be more verified by applying the following; however, these couldn't be achieved due to the data scarcity within the catchment.

- Finer DEM resolution such as 1 m LIDAR data, could better verify the conclusions related to the implications of the DEM spatial resolution on the wave propagation characteristics in the Wadi Al Batin ephemeral river system. For example, this could better present the spatially varying channel width within the domain. This should account for wider channel having a greater water volume infiltrate within the channel as found by Mudd's (2006). Therefore, this has an implication on the simulated travel time and the flooded area.

- Time Variable Inflow hydrograph retrieved from the rainfall stations within Al Batin catchment to retrieve the inflows from various stream sources within Al Batin catchment. Furthermore, the hydrograph shape plays an important role in the amount of water volume infiltrates within the channel as suggested by Mudd's (2006). This could more generalize the results and emerge the validity of the above conclusion.

- High resolution soil map to better present the soil texture within the catchment, which leads to better present the Green-Ampt infiltration parameters within the simulation domain. Therefore, it might strengthen the validity of the conclusion related to the implications of the infiltration loss on the on the wave propagation in the ephemeral river system.

Lastly, it is concluded that the significant variation in the estimated simulated wave propagation characteristics such as the flow travel time, the inundated area, and the water volume shows how vital and crucial the infiltration loss for flood risk assessment in the ephemeral system. Without focus on these it may lead to poor predictions for all flood wave propagation predictions figures.

Chapter 6 Conclusions

6.1 Summary of research aim and Objectives.

This conclusions chapter discusses the achievements of this research in terms of the research aim and the specific objectives as well as the contribution to the scientific community.

The aim of this research was defined in Chapter 1 as:

> *Extend an existing 2D flood inundation model (LISFLOOD-FP) by implementing a variable spatial infiltration process in the existing ephemeral channel flow routing model in order to understand the importance of this process on the prediction of flood risk parameters.*

This aim was to focus on achieving better understanding of the implications of the spatial variable channel bed infiltration process on the wave progression and characteristics in ephemeral systems. As infiltration is significant in ephemeral systems a better understanding of this is expected to lead to the ability to achieve more robust flood risk assessments in both temporal and spatial terms. In these ephemeral systems it could also potentially lead to a more informed and effective prediction flood warning system and emergency response effort as well as investment in resilience measures by the local authorities.

The research objectives defined earlier are:

- To investigate and determine the sensitivity analysis of 2D flood inundation models to the various topographical spatial data and various infiltration scenarios to assess whether higher spatial resolution digital elevation models will lead to more robust flash flood predictions in ephemeral river systems.
- To implement the spatially variable infiltration model into the 2D flood inundation model and to assess and evaluate its effectiveness.
- To determine whether implementing the spatial variable infiltration process in ephemeral channel flood routing models will lead to more robust flash flood assessments, and potentially provide more effective prediction, flood warning systems and effective emergency response.

The following sections discuss the conclusions from the specific objectives, the overall conclusion for this research and future work.

6.1.1 Specific objective 1: Determining and investigating the 2D flood inundation model sensitivity analysis to various topographical spatial resolution data.

This objective was addressed in Chapters 3 and 5, from the data described there. The following conclusions concerning the 2D flood inundation model sensitivity to various topographical spatial data can be summarised as follows:

- Varying the DEM's spatial resolution has a significant impact on 2D flood inundation model performance affecting flow routing behaviour. Estimations of the significance of the DEM's impact on 2D flood inundation model was explored through examination of the following flood wave progression characteristics in an ephemeral system: the flooded area, the water volume, the water depth, and the flow travel time from the start of the simulation domain to the end of the model domain's (a distance of 65 km).
- It is concluded that the DEM spatial resolution has a significant implication on the simulated flow travel time. The specific examples show a travel time increase from approximately 10 hours to 30 hours with increasing the DEM's resolution from 85 m to 343 m. In contrast to this another example shows a travel time decrease with increasing of the DEM's resolution from 90 m to 30 m. One conclusion to draw from this contradictory finding is that the resampling process can cause underestimation of the microtopographic flow paths. Therefore, it leads to quicker simulated travel time. Another conclusion to be drawn is that finer DEM resolution will lead to more reliable flow travel time estimation.
- The implications of varying DEM spatial resolution on the predicted flooded area, are that it has again a significant implication on the flooded area. It was demonstrated in an example that the flooded area increased from approximately 1 km^2 to 10 km^2 with increasing DEM resolution from 515 m to 85 m. Another example also shows an increase in the flood extent when increasing the DEM resolution from 90 m to 30 m. Furthermore, the inundation area is higher with a coarser resolution DEM compared to a finer resolution DEM. As the DEM resolution becomes coarser, there is loss of the topographical features presented within the cells from the smoothing of the elevations due to the DEM resampling. This leads to higher water surface elevations and greater flood inundation extents. It is concluded that there is an over prediction of the inundated area at larger DEM cell sizes.
- Based on the above observations, it is concluded that higher spatial resolution DEM will lead to more robust flood risk assessments for the ephemeral systems used in this demonstration. However, there are several limitations to be taken in consideration when using the DEM for flood assessments and modelling. The DEM is unable to resolve the channels if their widths are less than the DEM spatial resolution. Thus, the microtopographic flow path, could be

underestimated or even not present. Therefore, in this case a channel ground survey is recommended in order to obtain more channel ground truthing point for enhancing the DEM data accuracy and processing. Inaccurately or insufficiently resolved channels by the DEM would most likely lead to an overestimation of the flood inundation extent, and the flow travel time.

6.1.2 Specific objective 2: implementation of the variable spatially distributed Green-Ampt infiltration into a 2D Hydrodynamic model and assessment of the affect this has on flood inundation simulation.

A variety of testing scenarios were used to draw conclusions regarding implementation of the variable spatially distributed Green-Ampt infiltration into the 2D hydrodynamic model, these can be summarised as follows:

- Scenarios of varying complexity and were implemented to test scenarios in terms of estimating the variable spatial infiltration loss by using the implemented spatially distributed variable Green-Ampt infiltration. These tests include: ponding infiltration testing with a non-flowing one-meter cell, a more sophisticated flowing test of a simple conceptual river channel represented by line of 1 m cell size of 10 cells, and the testing of small subset of 2D river channel with spatially varied soil types from Wadi Al Batin in Saudi Arabia, which is within this research study area, and finally estimating the spatially distributed accumulated infiltration by testing model of spatially distributed pounding accumulated infiltration test with non-flowing of 10×10 cells. These various scenarios are, no infiltration, constant infiltration, and the spatially variable Green-Ampt infiltration scenario. These simulated test results give an initial indication of the successful implementation of the variable spatial distributed Green-Ampt infiltration into the 2D hydraulic model.
- The conclusions drawn from the simulations are based on expected behaviour following measurements from the simulation: the accumulated infiltration, water depth and the water balance. These were simulated using the updated version of the 2D hydrodynamic model through various infiltration scenarios described. These tests suggested the importance of simulating the variable infiltration to better reproduce the wave propagation characteristics.

6.1.3 Specific objective 3: To investigate and determine the implications of the infiltration loss on flood wave propagation characteristics in the ephemeral river system.

The conclusions concerning the implications of the infiltration loss on flood wave propagation characteristics in the ephemeral river system can be summarized as follows:

- Infiltration losses have a significant impact on the flood wave propagation characteristics in ephemeral river systems. This includes the extent of the flooded area, the water volume, and the flow travel time. These were demonstrated in the study catchment area of Wadi Al Batin in Saudi Arabia. The conclusion from this study is that applying the spatial variable Green-Ampt infiltration loss will provide more robust results in the flood risk assessments particularly in ephemeral systems.
- It is concluded that spatially variable Green-Ampt infiltration loss leads to shorter flow travel time in comparison with a constant infiltration implication on the flood wave propagation of the same model simulation run using the updated version of LISFLOOD-FP. This is related to the water volume infiltrated during the simulation run when applying the spatial variable Green-Ampt being less than the water volume infiltrated during the simulation run when applying the constant infiltration, therefore greater water volume remains in the model, thus there is a quicker flow travel time to reach the end of the domain. This conclusion is also applicable to the flooded area, meaning that when applying the spatial variable Green-Ampt less water volume being infiltrated during the simulation run leads to greater water volume left in the model, therefore a higher water level is predicted which leads to greater flood extent.

6.2 Sensitivity analysis conclusions

Sensitivity analysis of various parameters has been conducted. These parameters are DEM type and spatial resolutions, Manning's friction coefficients, infiltration rate and models of infiltration, and lastly various magnitude inflow hydrographs and duration.

The following conclusions have been drawn from these model sensitivity testing:

- It is concluded from the sensitivity analysis results that the simulations in this research are credible and valid conclusions can thus be drawn. This conclusion is based on the consistent pattern of the simulated wave propagation characteristics. Furthermore, this consistency was found even when applying various wide ranges of parameters. Examples of these patterns

observed are: flow travel time increases with increasing the infiltration rate and Manning's friction coefficients, also flooded area decreases with increasing the infiltration rate, and that flooded area increases with increasing the Manning's friction coefficients. Moreover, the flood extent decreases with applying various magnitude inflow hydrographs when compared against applying a constant inflow hydrograph of the same peak magnitude. In contrast, the travel time increases when applying a varying magnitude inflow hydrograph. These simulated patterns are explained and discussed in Chapter 3 and Chapter 5 in more detail.

- It is also concluded from the sensitivity analysis that the infiltration parameter has the most significant effect on the simulated flow travel time. However, the DEM spatial resolution has the most significant implication for the flood extent. Furthermore. It is concluded that a greater impact of other parameters such as the Manning's coefficient increases with increasing the infiltration rate. Therefore, this could increase the uncertainty of the flood risk modelling process. An example of this impact, is that when increasing the Manning's coefficient from 0.04 to 0.06, the implication of this increase on the travel time was approximately 22.1% when applying a constant infiltration rate of 3.1 cm/h. However, the implication of this increase on travel time is greater, reaching approximately 27.4% when applying a higher infiltration rate of 5.4 cm/h. More examples and details are found again in Chapter 3 and Chapter 5.

6.3 Research limitations

In this research, a methodology to develop an existing robust 2D flood inundation model by linking the variable spatial infiltration process, such as the Green-Ampt infiltration model to the existing ephemeral channel flow routing model. However, the limitation of the research is that no calibration and validation has been possible. This is mainly due to the data scarcity from the water authorities in Saudi Arabia. These data mainly could be a flow and stage gauges data.

As mentioned above, due to the difficulties of obtaining rainfall and storm gauges, arbitrary inflow hydrographs have been used in the model. This means it is not possible to apply different return period flows such as 2-year, 50-year and 100-year. Moreover, the hydrograph shape plays a crucial role in determining the volume of water infiltrated.

The finest DEM spatial resolution used in this research study is 30 m which probably means the microtopographic flow path could be underestimated or even eliminated within the 2D model simulation.

A coarse resolution global soil type map has been used in this research study to define Green-Ampt parameters as well as the selected infiltration rate.

Based on the above, it is difficult to eliminate the high degree of uncertainty associated with these parameters. This is a limitation of this research study, so the conclusions are mainly approximate.

On the other hand, the set of sensitivity analysis model runs carried out within this research, do allow for useful conclusions on the key parameters influencing the model predications. Knowing that a wide range of variable parameters have been included, and the results are consistent with what is expected as mentioned in Section 6.2 above.

6.4 Future research

The implementation and the effectiveness of the spatially variable Green-Ampt infiltration has been tested, but it would be interesting to carry out further testing with more sophisticated modelling complexity and scenarios. Moreover, it would be also interesting to implement an explicit Green-Ampt solution model such as Barry et al. (2005) (BA) and to compare the effectiveness and the accuracy of the chosen explicit model within this research.

Moreover, it would be very helpful to compare the simulated LISFLOOD-FP wave propagation characteristics results with the simulated results from other modelling tools, such as Flood Modeller, HECRAS, MODFLOW and TUFLOW. These software's are using Green-Ampt to estimate the spatial variable infiltration with in the 2D domain.

The methodology described in this research was to Wadi Al Batin in the east of Saudi Arabia. It would be useful to apply the same methodology in various case study areas, comparing the impact of the channel bed infiltration loss on flood wave progression in ephemeral systems, and investigating if the channel bed infiltration impact on flood wave progression varies in different case study areas within the ephemeral systems. Furthermore, it would be worthwhile in the future to calibrate and validate the 2D hydrodynamic model by conducting field work in Wadi Al Batin or a similar area. Furthermore, it would be worth if possible, obtaining a storm gauge data within the catchment area, so then various inflow hydrographs return period could be applied to the model.

Lastly, it would be very helpful for further future research to investigate the implications of using high spatial resolution DEM data retrieved from LIDAR data on the flood wave progression characteristics of a flood inundation model in the ephemeral systems. This recommendation is based on the conclusion above, that a higher spatial resolution DEM leads to more robust flood risk assessments

particularly in ephemeral systems, and potentially provide more effective prediction, flood warning system and developed emergency response as well as resilience measures for the local authorities.

References

Abdulrazzak, M. and Sorman, A. (1988). Water Balance Approach under Arid Conditions. J. Hydrol. Processes V(113), pp. 210-215.

Adger, W. (2006). Vulnerability. *Global Environmental Change*, 16, pp. 268–281.

Ali, S., Ghosh, N., Singh, R. and Sethy, B. (2013). Generalized Explicit Models for Estimation of Wetting Front Length and Potential Recharge. *Water Resour*, 27, pp. 2429–2445.

Ali, S., Islam, A., Mishra, P. and Sikka, A. (2016). Green-Ampt Approximations: A Comprehensive Analysis. *Journal of Hydrology*, *535*, pp.340-355.

Almedeij, J. and Esen, I. (2014). Modified Green–Ampt Infiltration Model for Steady Rainfall. *J. Hydrol. Eng*, 19 (9), pp. 04014011.

Al-Zahrani, M., Al-Areeq, A. and Sharif, H. (2016). Flood Analysis Using HEC-RAS Model: A Case Study for Hafr Al-Batin, Saudi Arabia. In E3S Web of Conferences (Vol. 7, p. 04024).

Archer, L., Neal, J., Bates, P. and House, J. (2018). Comparing TanDEM-X Data with Frequently Used DEMs for Flood Inundation Modelling. *Water Resources Research*, 54, 10, pp. 205–10,222.

Balamurugan, M. and Bhallamudi, S. (2016). Flood routing in an ephemeral channel with compound cross-section. *Sādhanā*, *41*(7), pp. 771-785.

Balica, S. (2012). *Applying the Flood Vulnerability index as a knowledge base for Flood Risk Assessment*. Ph.D. thesis, UNESCO-IHE Institute for Water Education.

Barry, D., Parlange, J., Li, L., Jeng, D. and Crapper, M. (2005). Green–Ampt Approximations. *Water Resour,* 28, pp. 1003–1009.

Bates, P.D., Horritt, M.S. and Fewtrell, T.J. (2010). A simple inertial formulation of the shallow water equations for efficient two-dimensional flood inundation modelling. *Journal of Hydrology*, 387(1-2), pp. 33-45.

Borga M., Boscolo P., Zanon F., Sangati M. (2007) Hydrometeorological Analysis of the August 29, 2003 Flash Flood in the Eastern Italian Alps. *J Hydrometeorol,* 8(5), pp.1049–1067.

Bouwer, H. (1978). *Groundwater Hydrology.* Wiley: New York.

Bracken, L., Cox, N. and Shannon, J. (2008). The Relationship between Rainfall Inputs and Flood Generation in South–East Spain. *Hydrological Processes: An International Journal*, *22*(5), pp.683-696.

Bracken, L., Wainwright, J., Ali, G., Tetzlaff, D., Smith, M., Reaney, S. and Roy, A. (2013). Concepts of Hydrological Connectivity: Research Approaches, Pathways and Future Agendas. *Earth-Science Reviews*, 119, pp. 17-34.

Bracken, L.J. and Croke, J. (2007). The Concept of Hydrological Connectivity and its Contribution to Understanding Runoff-Dominated Geomorphic Systems. *Hydrological Processes: An International Journal*, 21(13), pp. 1749-1763.

Budiyono, Y., Aerts, J., Brinkman, J., Marfai, M.A. and Ward, P. (2015). Flood Risk Assessment for Delta Mega-Cities: A Case Study of Jakarta. *Natural hazards*, 75(1), pp. 389-413.

Camarasa, A. and Tilford, K. (2002). Rainfall-runoff Modelling of Ephemeral Streams in the Valencia Region Eastern Spain. *Hydrological Processes*, 16, pp. 3329–3344.

Camarasa-Belmonte, A. (1995). Génesis de crecidas en pequeñas cuencas semiáridas: Barranc de Carraixet y Rambla del Poyo (Flood Generation in Small Semi-Arid Catchments: Carraixet and Poyo Basins).

Camarasa-Belmonte, A. (2016). Flash Floods in Mediterranean Ephemeral Streams in Valencia Region (Spain). *Journal of hydrology*, *541*, pp. 99-115.

Camarasa-Belmonte, A. and Soriano, J. (2014). Empirical Study of Extreme Rainfall Intensity in a Semi-Arid Environment at Different Time Scales. *Journal of Arid Environments*, *100*, pp.63-71.

Camarasa-Belmonte, A. and Soriano-García, J. (2012). Flood Risk Assessment and Mapping in Peri-Urban Mediterranean Environments Using Hydrogeomorphology. Application to Ephemeral Streams in the Valencia Region (Eastern Spain). *Landscape and Urban Planning*, 104(2), pp.189-200.

Cheng, L., Wang, Z., Hu, S., Wang, Y., Jin, J. and Zhou, Y. (2015). Flood Routing Model Incorporating Intensive Streambed Infiltration. *Science China Earth Sciences*, *58*(5), pp.718-726.

Chen, L., Young, M.H., 2006. Green-Ampt infiltration model for sloping surfaces, *Water Resources* Research, 42, pp.1-9, doi:10.1029/2005WR004468, 2006.

Collis-George, N. (1977). Infiltration Equations for Simple Soil Systems. *Water Resources Research,* 13(2), pp.395–403.

Costa, A., Foerster, S., de Araújo, J. and Bronstert, A. (2013). Analysis of Channel Transmission Losses in a Dryland River Reach in North-Eastern Brazil Using Streamflow Series, Groundwater Level Series and Multi-Temporal Satellite Data. *Hydrological Processes*, *27*(7), pp. 1046-1060.

Coulthard, T., Neal, J., Bates, P., Ramirez, J., de Almeida, G. and Hancock, G. (2013). Integrating the LISFLOOD-FP 2D Hydrodynamic Model with the CAESAR Model: Implications for Modelling Landscape Evolution. *Earth Surface Processes and Landforms*, 38(15), pp. 1897-1906.

Courty, L., Pedrozo-Acuña, A. and Bates, P. (2017). Itzï (version 17.1): An Open-Source, Distributed GIS Model for Dynamic Flood Simulation. *Geoscientific Model Development*, 10(4), pp.1835-1847.

Dottori, F., Salamon, P., Bianchi, A., Alfieri, L., Hirpa, F. A. and Feyen, L. (2016). Development and Evaluation of a Framework for Global Flood Hazard Mapping. *Advances in Water Resources*, 94, pp. 87–102.

Dunkerley, D. (2012). Effects of Rainfall Intensity Fluctuations on Infiltration and Runoff: Rainfall Simulation on Dryland Soils, Fowlers Gap, Australia. *Hydrological Processes*, *26*(15), pp.2211-2224.

Earth Observation Center (2018). TanDEM-X Ground Segment Dem Products Specification Document. https://geoservice.dlr.de/web/dataguide/tdm90/pdfs/TD-GS-PS-0021_DEM-Product-Specification.pdf, TD-GS-PS-0021, Accessed on Fri, April 09, 2021.

El-Hames, A., and Richards, K. (1998). An Integrated, Physically-based Model for Arid Region Flash Flood Prediction Capable of Simulating Dynamic Transmission Loss. *Hydrol. Processes*, 12(8), pp. 1219–1232.

Farr, T. G., Rosen, P. A., Caro, E., Crippen, R., Duren, R., Hensley, S., et al. (2007). The Shuttle Radar Topography Mission. *Reviews of Geophysics*, 45 (2).

Fernández-Pato, J., Caviedes-Voullième, D. and García-Navarro, P. (2016). Rainfall/Runoff Simulation with 2D Full Shallow Water Equations: Sensitivity Analysis and Calibration of Infiltration Parameters. *Journal of hydrology*, *536*, pp.496-513.

Freyberg, D. (1983). Modelling the Effects of a Time-Dependent Wetted Perimeter on Infiltration from Ephemeral Channels. *Water Resources Research,* 19 (2), pp. 559–566.

Glenis, V., Kutija, V. and Kilsby, C. (2018). A Fully Hydrodynamic Urban Flood Modelling System Representing Buildings Green Space and Interventions. *Environmental Modelling & Software*, 109, pp. 272–292.

Goodrich, D., Lane, L., Shillito, R., Miller, S., Syed, K. and Woolhiser, D. (1997). Linearity of basin Response as a Function of Scale in a Semiarid Watershed. *Water Resour. Res.*, 33(12), pp. 2951–2965.

Green, W. and Ampt, C. (1911). Studies on Soil Physics, I. Flow of Air and Water through Soils. *Journal of Agricultural Science*, 4: 1–24.

Grigorjev, V. and Iritz, L. (1991). Dynamic Simulation Model of Vertical Infiltration of Water in Soil. *Journal of Hydrological Sciences,* 36(2), pp. 171–179.

Guha-Sapir, D., Vos, F., Below, R. and Ponserre, S. (2012). Annual Disaster Statistical Review 2011: The Numbers and Trends.

Gülbaz, S., Boyraz, U. and Kazezyılmaz-Alhan, C. (2020). Investigation of Overland Flow by Incorporating Different Infiltration Methods into Flood Routing Equations. *Urban Water Journal*, *17*(2), pp.109-121.

Hand W., Fox N., Collier C. (2004). A Study of Twentieth-Century Extreme Rainfall Events in the United Kingdom with Implications for Forecasting. *Meteorology Applied,* 11, pp. 15-31.

Hansson, K., Danielson, M. and Ekenberg, L. (2008). A Framework for Evaluation of Flood Management Strategies. *Journal of environmental management*, *86*(3), pp. 465-480.

Helali, Awad. (1993) The relationship between soil infiltration and effective porosity in different soils. *Agriculture Water Management*, 24, pp.39-47.

Hodgson, M.E. and Bresnahan, P. (2004). Accuracy of Airborne Lidar-Derived Elevation. *Photogrammetric Engineering & Remote Sensing*, 70(3), pp. 331-339.

Holtan, H. (1961). *A Concept of Infiltration Estimates in Watershed Engineering*. Department of Agricultural Service: U.S., Washington, DC.

Horritt M., Bates P. (2002). Evaluation of 1D and 2D Numerical Models for Predicting River Flood Inundation. *J Hydrol*,268, pp. 87–99.

Horton, R. (1938). The Interpretation and Application of Runoff Plot Experiments with Reference to Soil Erosion Problems. *Soil Science Society of America Proceedings*, 3, pp. 340–349.

Huggins, L. and Monke, E. (1966). The Mathematical Simulation of the Hydrology of Small Watersheds. Technical Report No. 1, Purdue Water Resources Research Centre, Lafayette.

Jin, H. and Ward, G. (2005). Hydraulic Characteristics of a Small Coastal Plain Stream of the South-eastern United States: Effects of Hydrology and Season. *Hydrological Processes*, 19(20), pp.4147–4160.

Jonkman, S. and Vrijling, J. (2008). Loss of Life due to Floods. *Journal of Flood Risk Management*, *1*(1), pp. 43-56.

Kale, R. and Sahoo, B. (2011). Green–Ampt Infiltration Models for Varied Field Conditions: A Revisit. *Water Resour*, 25, pp. 3505–3536.

Korichi, K., Hazzab, A. and Atallah, M. (2016). Flash Floods Risk Analysis in Ephemeral Streams: A Case Study on Wadi Mekerra (Northwestern Algeria). *Arabian Journal of Geosciences*, *9*(11), pp. 1-11.

Kostiakov, A. (1932). On the Dynamics of the Coefficient of Water Percolation in Soils and the Necessity of Studying it from the Dynamic Point of View for the Purposes of Amelioration. *Trans. Sixth Comm. Int. Soc. Soil Sci.*, *1*, pp.7-21.

Kowalsky, M., Finsterle, S., Peterson, S., Hubbard, J., Rubin, Y., Majer, E., Ward, A. and Gee, G. (2005). Estimation of Field-Scale Soil Hydraulic and Dielectric Parameters through Joint Inversion of GPR and Hydrological Data. *Water Resour Res,* 41, pp. 11425.

Laurence Hawker, Jeffrey Nael (2021). FABDEM V1-0. University of Bristol. https://doi.org/10.5523/ bris.25wfy0f9ukoge2gs7a5mqpq2j7

Li, R., Steven, M. and Simons, D. (1976). Solutions to Green–Ampt Infiltration Equation. *J. Irrig. Drain. Eng. Div. ASCE* 102 (2), pp. 239–248.

MacCormack, R. (1971). Numerical solution of the interaction of a shock wave with a laminar boundary layer. In *Proceedings of the second international conference on numerical methods in fluid dynamics* (pp. 151-163). Springer, Berlin, Heidelberg.

Maghrabi K. (2012). Impact of Flood Disaster on the Mental Health of Residents in the Eastern Region of Jeddah Governorate, 2010: A Study in Medical Geography. *Life Science Journal*, 9(1), pp. 95-110.

McClean, F., Dawson, R. and Kilsby, C. (2020). *Data and Code Supporting McClean et al. (2020) Implications of Using Global Digital Elevation Models for Flood Risk Analysis in Cities*. Water Resources Research, Newcastle University.

Mein, R. and Larson, C. (1971). Modelling the Infiltration Component of the Rainfall-Runoff Process. WRRC Bull. Water Resources Research Center: University of Minnesota, Minneapolis.

Mein, R. and Larson, C. (1973). Modelling Infiltration during a Steady Rain. *Water Resources Research,* 9(2), pp. 384–394.

Mishra, S., Kumar, S., and Singh V. (1999). Calibration of a General Infiltration Model. *Journal of Hydrological Processes,* 13, pp. 1691–1718.

Mishra, S., Tyagi, J. and Singh, V. (2003). Comparison of Infiltration Models. *Journal of Hydrological Processes,* 17, pp. 2629–2652.

Momani N. and Fadil A. (2010). Changing Public Policy due to Saudi City of Jeddah Flood Disaster. *Journal of Social Sciences*, 6(3), pp. 424-428.

Mudd, S. (2006). Investigation of the Hydrodynamics of Flash Floods in Ephemeral Channels: Scaling Analysis and Simulation Using a Shockcapturing Flow Model Incorporating the Effects of Transmission Losses. *J. Hydrol*., 324(1–4), pp. 65–79.

MunichRe, (2015). Natural Disasters 2014. [online]. [Accessed 25 April 2021]. Available from: https://www.munichre.com/touch/naturalhazards/en/25natcatservice/annual-statistics/index.html.

Neal, J., Schumann, G. and Bates, P. (2012). A Subgrid Channel Model for Simulating River Hydraulics and Floodplain Inundation over Large and Data Sparse Areas. *Water Resources Research*, 48(11).

Neuman, S.P. (1976). Wetting Front Pressure Head in the Infiltration Model of Green and Ampt. *Water Resources Research*, 12(3), pp. 564-566.

Ni, Y., Cao, Z., Liu, Q. and Liu, Q. (2020). A 2D Hydrodynamic Model for Shallow Water Flows with Significant Infiltration Losses. *Hydrological Processes*, *34*(10), pp. 2263-2280.

Ordnance Survey (2017). *User Guide and Technical Specification—OS Terrain 50.* https://www.ordnancesurvey.co.uk/documents/ os-terrain-50-user-guide.pdf, Accessed on Sat, April 11, 2020.

Overton, D. (1964). *Mathematical Refinement of an Infiltration Equation for Watershed Engineering*. ARS 41–99, U.S. Department of Agricultural Service, Washington, DC.

Parissopoulos, G. and Wheater, H. (1991). Effects of Wadi Flood Hydrograph Characteristics on Infiltration. *J. Hydrol.,* 126(3–4), pp. 247–263.

Parlange, J., Barry, D. and Haverkamp, R. (2002). Explicit Infiltration Equations and the Lambert W-Function. *Water Resour*, 25, pp. 1119–1124.

Philip, J. (1957). Theory of Infiltration. *Soil Science,* 83(5), pp.345–357.

Rao, M.D., Raghuwanshi, N.S. and Singh, R. (2006). Development of a Physically-based 1D-Infiltration Model for Irrigated Soils. *Agricultural Water Management*, 85(1-2), pp. 165-174.

Rawls, W., Brakensiek, D. and Saxon, K. (1982). Estimation of Soil Water Properties. *Trans. ASAE,* 25, pp. 1316–1320.

Rode, A. (1965). Theory of Soil Moisture, Vol. 1 (translated from Russian). Published for USDA and NSF by the Israel Program for Scientific Translation, Jerusalem, 1969.

Saksena, S. and Merwade, V. (2015). Incorporating the Effect of DEM Resolution and Accuracy for Improved Flood Inundation Mapping. *Journal of Hydrology*, 530, pp. 180-194.80-93.

Salvucci, G. and Entekhabi, D. (1994). Explicit Expression for Green-Ampt (Delta Function Diffusivity) Infiltration Rate and Cumulative Storage. *Water Resour Res,* 30(9), pp.2661–2663.

Sampson, C., Smith, A., Bates, P., Neal, J., Alfieri, L. and Freer, J. (2015). A High-Resolution Global Flood Hazard Model. *Water Resources Research*, 51, pp. 7358–7381.

Sanders B. (2002). Non-reflecting Boundary Flux Function for Finite Volume Shallow-Water Models. *Adv Water Resour*, 25, pp. 195–202.

Schumann, G., Neal, J., Voisin, N., Andreadis, K., Pappenberger, F., Phanthuwongpakdee, N., Hall, A. and Bates, P. (2013). A First Large-Scale Flood Inundation Forecasting Model. *Water Resources Research*, 49(10), pp. 6248-6257.

Shannon, J., Richardson, R. and Thornes, J. (2002). Modelling Event-Based Fluxes in Ephemeral Streams. *Dryland Rivers: Hydrology and Geomorphology of Semi-Arid Channels*, pp. 129-173.

Singh, V. And Yu, F. (1990). Derivation of Infiltration Equation Using Systems Approach. *Journal of Irrigation and Drainage Engineering*, 116(6), pp. 837–857.

Smith, R. (1972). The Infiltration Envelope: Results from a Theoretical Infiltrometer. *Journal of Hydrology,* 17, pp. 1–21.

Smith, R. and Parlange, J-Y. (1978). A Parameter-Efficient Hydrologic Infiltration Model. *Water Resources Research* 14(3), pp. 533–538.

Smith, R., Goodrich, D., Woolhiser, D. and Unkrich, C. (1995). KINEROS-a Kinematic Runoff and Erosion Model. *Computer Models of Watershed Hydrology*, pp. 697-732.

Sokol, Z. (2003). The Use of Radar and Gauge Measurements to Estimate Areal Precipitation for Several Czech River Basins. *Studia Geophysica et Geodaetica, Springer*, 47(3), pp. 587–604.

Stone, J., Hawkins, R. and Shirley E. (1994). Approximate form of Green-Ampt Infiltration Equation. *J Irrig Drain Engg ASCE*, 120(1), pp. 128–137.

Swamee, P., Rathie, P. and Ozelim, L. (2012). Explicit equations for infiltration. *J. Hydrol*. pp. 151–153.

Tachikawa, T., Hato, M., Kaku, M. and Iwasaki, A. (2011), July. Characteristics of ASTER GDEM version 2. In *2011 IEEE international geoscience and remote sensing symposium* (pp. 3657-3660). IEEE.

Tadono, T., Ishida, H., Oda, F., Naito, S., Minakawa, K. and Iwamoto, H. (2014). Precise Global DEM Generation by ALOS PRISM. *ISPRS Annals of Photogrammetry Remote Sensing and Spatial Information Sciences*,4, pp. 71–76.

Tügel, F., Hassan, A., Wannous, M., Tröger, U. and Hinkelmann, R. (2020), May. Investigation of the Green-Ampt Infiltration Model in Rainfall-Runoff Simulations with a Robust 2D Shallow Water Model. In *EGU General Assembly Conference Abstracts* (p. 19020).

UNDP (2004). Reducing Disaster Risk. A challenge for Global Report. New York: United Nations Development Programme Development [online]. [Accessed 25 April 2021]. Available from: http://www.undp.org/cpr/disred/documents/publications/rdr/english/rdrenglish.pdf

UNISDR, C. (2015). The Human Cost of Natural Disasters: A Global Perspective.

Vatankhah, A. (2015). Discussion of Modified Green–Ampt Infiltration Model for Steady Rainfall by J. Almedeij and I.I. Esen. J*. Hydrol. Eng*,20,(4), pp.07014011-1–07014011-3.

Wainwright, J., Turnbull, L., Ibrahim, T.G., Lexartza-Artza, I., Thornton, S.F. and Brazier, R. (2011). Linking Environmental Regimes, Space and Time: Interpretations of Structural and Functional Connectivity. *Geomorphology,* 126(3-4), pp. 387-404.

Ward, P., Jongman, B., Weiland, F., Bouwman, A., van Beek, R., Bierkens, M., et al. (2013). Assessing Flood Risk at the Global Scale: Model Setup Results, and Sensitivity. *Environmental Research Letters*, 8(4), pp. 044019.

Weiler, M., Leistert, H. and Steinbrich, A. (2020), May. Which Event Produces the Largest Flash Flood? Considering Rainfall Characteristics, Initial Soil Moisture, Retention and Run-On Infiltration. In *EGU General Assembly Conference Abstracts* (p. 18172).

Wilson, M., Bates, P., Alsdorf, D., Forsberg, B., Horritt, M., Melack, J., Frappart, F. and Famiglietti, J. (2007). Modeling Large-Scale Inundation of Amazonian Seasonally Flooded Wetlands. *Geophysical Research Letters*, 34(15).

Yamazaki, D., Ikeshima, D., Tawatari, R., Yamaguchi, T., O'Loughlin, F., Neal, J. C., et al. (2017). A High-Accuracy Map of Global Terrain Elevations. *Geophysical Research Letters*, 44, pp. 5844–5853.

Yan, B., Guo, S. and Chen, L., 2014. Estimation of Reservoir Flood Control Operation Risks with Considering Inflow Forecasting Errors. *Stochastic Environmental Research and Risk Assessment*, 28(2), pp. 359-368.

Yang, J. and Chu, X., 2015. A New Modelling Approach for Simulating Microtopography-Dominated, Discontinuous Overland Flow on Infiltrating Surfaces. *Advances in Water Resources*, 78.

Zhang, Q., Chen, W. and Kong, Y. (2020). Modification and Discussion of the Green-Ampt Model for an Evolving Wetting Profile. *Hydrological Sciences Journal*, 65(12), pp. 2072-2082.